APPROVAL SHEET

Title of Dissertation: BIOENGINEERED MODELS OF ALZHEIMER'S DISEASE: STUDYING AMYLOID BETA (Aβ) PROTEIN AGGREGATION WITHIN 3D SCAFFOLDS

Name of Candidate: Laura W. Simpson

Doctor of Philosophy, 2019

Dissertation and Abstract Approved: Jennie B Leach

Dr. Jennie B. Leach

Associate Professor & Graduate Program Director

Chemical, Biochemical & Environmental Engineering

Date Approved: 4/23/19

CURRICULUM VITAE

Name: Laura W. Simpson

Degree and date to be conferred: Doctor of Philosophy, 2019

Secondary education: University of Maryland Baltimore County (UMBC), Baltimore, MD, May 22, 2019.

Collegiate institutions attended:

University of Maryland Baltimore County (UMBC). 2008 - 2013

Baltimore, Maryland.

Biology B.S., 2013.

Psychology Minor, 2013.

University of Maryland Baltimore County (UMBC). 2013 - 2019

Baltimore, Maryland.

Chemical & Biochemical Engineering, Ph.D., 2019.

Professional Publications:

Peer-Reviewed Manuscript

- Santos-Cancel, M.; Simpson, L. W.; Leach, J. B.; White, R. J., Direct, Real-Time Detection of Adenosine Triphosphate Release from Astrocytes in Three-Dimensional Culture Using an Integrated Electrochemical Aptamer-Based Sensor. ACS Chem Neurosci 2019

Manuscripts in Preparation

- Simpson, L. W.; Good, T. A.; Leach, J. B., Protein folding and assembly in confined environments: Implications for protein aggregation in biomaterial scaffolds and tissues. 2019
- Simpson, L. W.; Boukari, H.; Good, T. A.; Leach, J. B., Collagen hydrogel confinement of Amyloid-β (Aβ) accelerates aggregation and reduces cytotoxic effects. 2019
- Simpson, L. W.; Boukari, H.; Good, T. A.; Leach, J. B., Impact of four common hydrogels on Amyloid-β (Aβ) aggregation and cytotoxicity: Implications for 3D models of Alzheimer's disease. 2019

Presentations:

Scientific Meetings (Presenter underlined)

- Simpson, L. W.; Good, T. A.; Leach, J. B., "Bioengineered models of Alzheimer's disease: Studying Aβ protein aggregation within 3D scaffolds", Biophysical Society (BPS), Baltimore, MD, March 2019, (POSTER)
- Simpson, L. W.; Leach, J. B., "Bioengineered models of Alzheimer's disease: Studying Aβ protein aggregation within 3D scaffolds", American Chemistry Society (ACS), New Orleans, LA, March 2018, (ORAL)
- Simpson, L. W.; Leach, J. B., "Bioengineered models of Alzheimer's disease: Studying Aβ protein aggregation within 3D scaffolds", American Chemistry Society (ACS), San Francisco, CA, March 2017, (ORAL)
- Simpson, L. W.; Leach, J. B., "Phenotypic characterization of NSC-34 a motor neuron cell line", Washington, DC, December 2014, (POSTER)
- Adamson, E.; Simpson, L. W.; Balasubramanian, S.; Leach, J. B., "Baseline characterization of NSC-34 cell line for tissue engineering application." Annual Biomedical Research Conference for Minority Students (ABRCMS), San Antonio, TX, November 2014, (POSTER)

Professional positions held:

Graduate Research Assistant, Leach Biomaterials Laboratory, UMBC

Advisor: Dr. Jennie Leach

Summer 2013 – Spring 2019

Teaching Assistant, Chemical, Biochemical, & Environmental Engineering Department, UMBC

Bioengineering Laboratory, ENCH 485L	Spring 2016
Bioengineering Laboratory, ENCH 485L	Spring 2015
Transport Processes I, ENCH 425	Fall 2014
Bioengineering Laboratory, ENCH 485L	Spring 2014

Mentor, Chemical, Biochemical, & Environmental Engineering Department, UMBC

Elise Adamson, Chemical Engineering, UMBC	Spring 2014 – Spring 2017
Vani Ravichandran, Biochemistry, UMBC	Spring 2016 – Spring 2017
Becca Glatt, Chemical Engineering, UMBC	Summer 2015
Jake Engel, Chemical Engineering, UMBC	Summer 2016 – Summer 2017
Robert Atwood, Chemical Engineering, UMBC	Fall 2016 – Summer 2017
Fabria Baptise, Chemical Engineering, UMBC	Fall 2016 – Fall 2018
Aryeh Sherizen, Chemical Engineering, UMBC	Winter 2017 – Summer 2017
Rose Zilberberg, Chemical Engineering, UMBC	Spring 2017 – Summer 2017
Howard Nicholson, Chemical Engineering, UMBC	Fall 2017 – Spring 2019
Peter Bailer, Biochemistry, UMBC	Fall 2017 – Spring 2019
Christopher Williams, Biochemistry, UMBC	Summer 2018 – Fall 2018
Bilal Mughal, Chemical Engineering, UMBC	Summer 2018 – Spring 2019
Kendall McWilliams, Chemical Engineering, UMBC	Fall 2018 – Spring 2019

Chemical Engineering Intern, James Webb Space Telescope (JWST), Goddard Space Flight Center, National Aeronautics and Space Administration (NASA)

Summer 2013

Undergraduate Research Assistant, Leach Biomaterials Laboratory, UMBC

Advisor: Dr. Jennie Leach

Spring 2010 – Spring 2013

Resident Assistant, Hilltop Apartments, UMBC

Mentor: Doug Copeland

Fall 2012 – Spring 2013

Planetary Protection Intern, Mars Atmosphere and Volatile EvolutioN (MAVEN), Goddard Space Flight Center, NASA

Summer 2011

Configuration Management Intern, supporting NASA contracts, Stinger Ghaffarian Technologies

Summer 2008, 2009, 2010 & Winter 2010

ABSTRACT

Title of Dissertation: **BIOENGINEERED MODELS OF ALZHEIMER'S DISEASE: STUDYING AMYLOID BETA (Aβ) PROTEIN AGGREGATION WITHIN 3D SCAFFOLDS.**

Laura W. Simpson, Doctor of Philosophy, 2019

Dissertation Directed By: Dr. Jennie B. Leach
Associate Professor & Graduate Program Director
Chemical, Biochemical and Environmental Engineering

Alzheimer's disease (AD) is the most common form of dementia and is associated with the accumulation of amyloid-β (Aβ), a peptide that can aggregate into larger species with presumed neurotoxicity. Drugs targeting Aβ have shown great promise in 2D *in vitro* cultures and mouse models, yet human clinical trials for AD have yielded highly disappointing results.

In developing this project, I proposed that 2D *in vitro* culture systems that have been used for discovering and developing AD drugs have significant limitations. Specifically, I hypothesized that Aβ aggregation is vastly different in 2D cultures vs 3D environments, such as brain tissue. In 2D cultures, Aβ can freely diffuse and aggregate. In 3D environments, however, Aβ rearrangements are spatially restricted or "confined". Such confinement acts to exclude solvent from Aβ, resulting in Aβ

having an increased local concentration and decreased entropy. The net outcome of these effects is the destabilization of disordered Aβ structures, shifting equilibrium towards larger aggregate species. It is striking that only a few 3D *in vitro* AD models have been reported, all of which ignore potential changes to Aβ structure and function that may occur within 3D systems.

This dissertation reports my investigation of Aβ aggregation and toxicity in 3D hydrogels compared to 2D culture using biophysical tools including transmission electron microscopy, fluorescence correlation spectroscopy, and thioflavin T assays. In 3D hydrogels, I found that Aβ rapidly transitions from unstructured and likely toxic oligomeric species to stable β-sheet aggregates. In 2D cultures, however, the oligomeric species has prolonged persistence. Despite quantitative differences in aggregation kinetics between hydrogels of various mesh size and bioactivity, all of the 3D hydrogels tested had attenuated Aβ cytotoxicity vs 2D culture. Therefore, this work suggests that efforts to develop AD drugs using 2D *in vitro* models may overestimate the potential toxicity of Aβ, and thus offers an explanation for the decades of failed AD drug clinical trials. These findings imply that drug discovery and development for AD, and potentially other diseases, will more rapidly identify therapeutics with greater efficacy if 3D cultures are included in early testing stages.

BIOENGINEERED MODELS OF ALZHEIMER'S DISEASE: STUDYING AMYLOID BETA (Aβ) PROTEIN AGGREGATION WITHIN 3D SCAFFOLDS

By

Laura W. Simpson

Dissertation submitted to the Faculty of the Graduate School of the
University of Maryland, Baltimore County, in partial fulfillment
of the requirements for the degree of
Doctor of Philosophy
2019

Dedication

To my mom, dad, and loving husband.

Acknowledgements

I would like to extend my deepest gratitude to my advisor Dr. Jennie Leach who has been my mentor and advocate since I was an undergraduate research assistant in her lab. She has believed in me from the very beginning and the completion of my dissertation would not have been possible without her support. I am also extremely grateful to Dr. Theresa Good whose invaluable insight into Aβ aggregation kept me sane during trying times. I would like to express my deepest appreciation to my committee for their valuable advice. Special thanks to Dr. Hacene Boukari for granting me access to his FCS system at Delaware State University (DSU) and for his guidance in FCS theory and data analysis.

I cannot leave UMBC without mentioning Victor Fulda, who keeps our department running smoothly and has been a dear friend to me; I will miss our morning chats. Thanks also to Tagide deCarvalho for the training and assistance with the confocal and TEM microscopes. I would like to thank the rest of the faculty, staff, and students in the Chemical, Biochemical, & Environmental Engineering Department.

I cannot begin to express my thanks to my parents Nancy and Robert, who have loved and supported me every step of the way; to my husband Mike, who has provided me with encouragement and patience throughout the duration of my PhD; and to my husband's family Bridget, Jim, Shawn and Lauren, who have never wavered in their support.

Table of Contents

List of Figures

List of Abbreviations

2D	Two-dimensional
3D	Three-dimensional
ACH	Amyloid cascade hypothesis
AD	Alzheimer's disease
AEM	N-(2-aminoethyl) maleimide trifluoroacetate salt
AFM	Atomic force microscopy
Aβ	Amyloid-β
BSA	Bovine serum albumin
CD	Circular dichroism
CR	Congo Red
D_i	Diffusion constants
DMEM	Dulbecco's Modified Eagle's Medium
ECM	Extracellular matrix
EDC	1-Ethyl-3-(3-dimethylaminopropyl) carbodiimide
FA	Fluorescence anisotropy

FAM Scr Aβ	FAM-labeled Scrambled Aβ
FCS	Fluorescence correlation spectroscopy
FDA	Food and Drug Administration
FFF	Field flow fractionation
FP	Fluorescence polarization
FRAP	Fluorescence recovery after photobleaching
FRET	Fluorescence resonance energy transfer
FTIR	Fourier transform infrared
G(τ)	Autocorrelation
HA	Hyaluronic acid
HiLyte Aβ	HiLyte 488-labeled Aβ
I(t)	Fluorescence intensity
IDP	Intrinsically disordered proteins
IDR	Intrinsically disordered regions
MEM	Maximum Entropy Method
MES	2-(N-morpholino)ethanesulfonic acid
MFI	Micro-flow imaging

NHS	N-hydroxysuccinimide
NMR	Nuclear magnetic resonance spectroscopy
PBS	Phosphate buffered saline
PEG	Polyethylene glycol
PMT	Photon multiplier tubes
R_H	Hydrodynamic radius
RICS	Raster image correlation spectroscopy
SANS	Small angle neutron scattering
SAXS	Small angle X-ray scattering
Scr Aβ	Scrambled Aβ
SEM	Scanning electron microscopy
SIM	Structured illumination microscopy
SLS	Static light scattering
SPT	Single particle tracking
SRM	Super-resolution microscopy
STED	Stimulated emission depletion
STORM	Stochastic optical reconstruction microscopy

TEM	Transmission electron microscopy
ThS	Thioflavin S
ThT	Thioflavin T
TIRFM	Total internal reflection fluorescence microscopy
w_0	Characteristic radial dimension
z_0	Characteristic axial dimension
τ_D	Residence time

Chapter 1 : Summary of Work

As readers of this document will vary greatly in their expertise related to my work, I provide this chapter to describe my doctoral work to a broad audience.

Alzheimer's disease (AD) is the leading cause of dementia and is the sixth leading cause of death in the United States (US) [1]. Currently in 2019, 5.8 million Americans are living with AD, and this number is projected to increase to 14 million by 2050. In 1991, a genetic link was found between AD and the protein amyloid-β (Aβ), whose accumulation and aggregation is associated with neuronal death [2-4]. The connection between Aβ and AD was termed the "amyloid cascade hypothesis" (ACH), and Aβ has since been a primary target in AD drug development.

Aβ is naturally produced by cells in the brain and is removed from the body in healthy individuals [5-6]. The ACH states that in AD, Aβ accumulates in the brain and sticks together into unstructured aggregates called oligomers that are toxic to neurons. Neuron death leads to memory loss and other AD symptoms. Eventually, Aβ stabilizes into a hairpin structure called a β-sheet, which promotes other Aβ proteins to stack as a β-sheet (Figure 1.1) [7-9]. The β-sheet structures come together to form long fibril aggregates called plaques that cluster in the brain and are less toxic than the oligomer Aβ [10-12]. Unfortunately, early stages of AD cannot be directly studied in humans because obvious symptoms are not present for many years after the onset of the disease process in the brain. Therefore, the ACH has been based on data gathered through brain tissue samples upon autopsy, mouse models, mathematical

models, 2D *in vitro* cell culture models, and Aβ aggregation studies in solutions [6, 13-14].

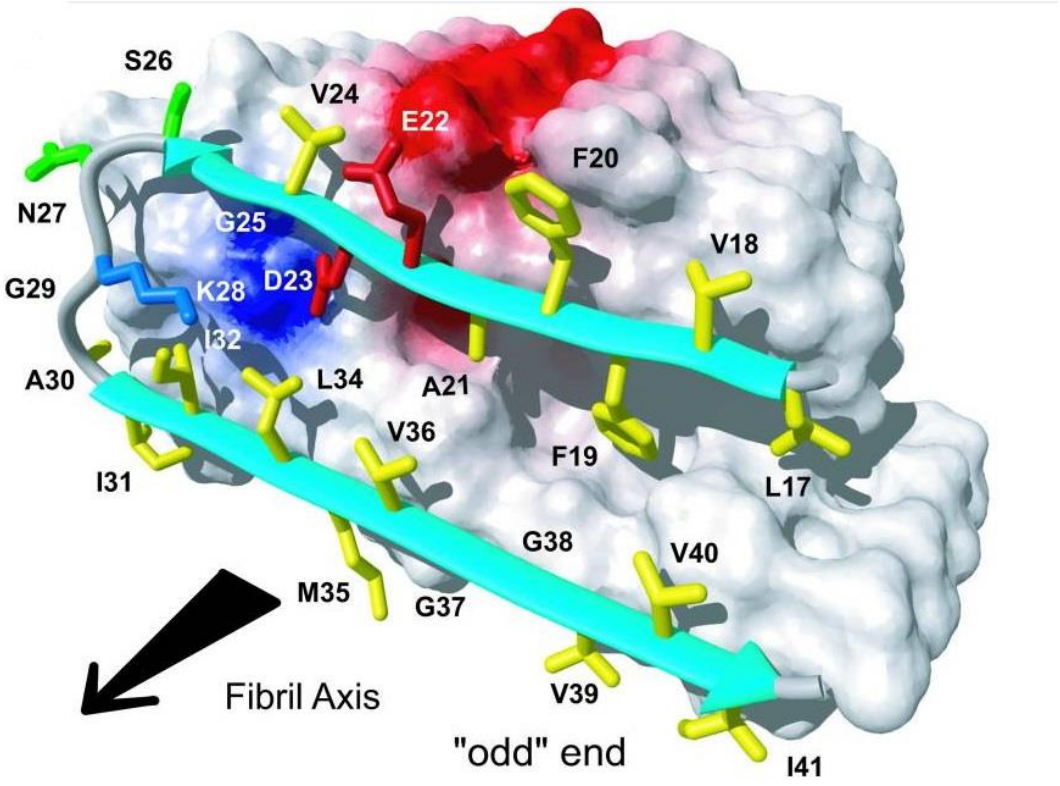

Figure 1.1 Structure of Aβ taking on a hairpin fold known as a β-sheet. The cyan arrows signify the β-sheet structure. The hydrophobic, polar, negatively charged, and positively charged amino acid side chains are shown in yellow, green, red, and blue. This structure allows additional Aβ monomers to stack, signified by the white globular structure. Reproduced from [15] copyright 2005 National Academy of Sciences.

There are four unique drugs licensed by the Food and Drug Administration (FDA) that treat symptoms of AD, but do not slow, prevent, or cure the disease [1, 16]. The lack of drugs is not due to a lack of interest, however, as the field of

neurology has the third largest number of drugs in preclinical development and Phase III clinical trials (oncology first and cardiovascular second) [17]. Many drugs that showed great promise in pre-clinical trials (two-dimensional (2D) cell culture and mouse models) have failed to show efficacy in human clinical trials [18-20]. The consistent failure of ACH-targeting drugs has prompted the question: What is the disconnect between pre-clinical and clinical trials?

Typically, when cells are cultured *in vitro*, they are grown on a stiff, flat surface as a single layer (Figure 1.2). However, our bodies are complex three-dimensional (3D) systems, where cells are held together with the extracellular matrix (ECM), which contains various biologic fibers and gives tissues their structural properties [21]. These ECM molecules, as well as other natural and synthetic biomaterials, may be used in *in vitro* cell culture providing a 3D scaffold for cells to adhere to and grow throughout [22-23]. These 3D *in vitro* models produce cells that behave and look very similar to *in vivo* body tissues compared to 2D cell cultures [24-26]. Although many fields, and most notably, the cancer research field, have moved toward 3D *in vitro* models, AD research primarily takes place in 2D cultures or studies of Aβ aggregation in solution [27-29].

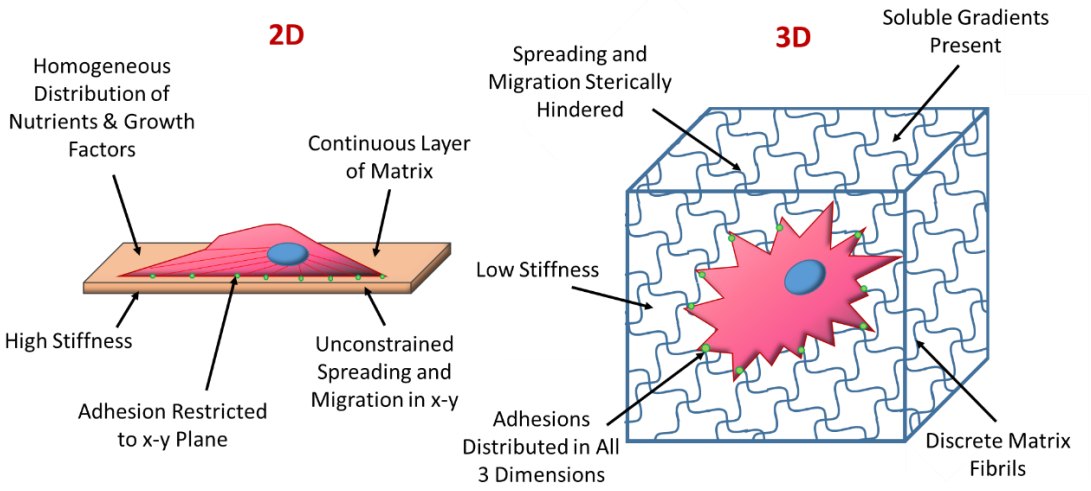

Figure 1.2 Cells cultured on 2D tissue plastic vs. in 3D hydrogels. Cells cultured in 2D are exposed to high stiffness, homogeneous distribution of nutrients, and a continuous layer of matrix coating and are restricted to the x-y plane. Cells cultured in 3D hydrogels are exposed to low stiffness, soluble gradients, and three dimensions of matrix interactions.

One of the challenges of doing research in 3D *in vitro* models is the adaptation of measurement techniques that were designed for 2D cultures and solutions. In a field such as AD, where the Aβ protein is hypothesized to play an important role in disease progression, analysis of not only cells but also of proteins in the 3D environment is essential. In **Chapter 2**, I present the progress of techniques developed to analyze proteins, the effect of confinement on protein structure and function, and the challenges of studying proteins in 3D environments.

An often overlooked aspect of 3D environments is the effect of confinement on proteins [30-32]. Imagine being in an open field; you have ample space to, for example, do gymnastics. Now imagine being in a cupboard under the stairs; you

cannot spread out or move very much, rather you must take on a compact shape. The same concept applies to proteins in confined spaces; they are forced to take on a more compact structure such as a β-sheet [33-34]. In **Chapter 3**, I report my findings of how the confined environment imposed by a collagen hydrogel changes Aβ structure, aggregation, and toxicity. (Gelatin is 'denatured' or broken-down collagen, so one may imagine collagen hydrogels to look and feel a lot like Jello.) I predicted that the confined environment in the collagen will promote Aβ to form more ordered, compact β-sheet structures, which will then come together to make large β-sheet fibrils that are less toxic to cells. To test this prediction, I tested the cell toxicity of Aβ in culture with a live/dead fluorescence assay. I imaged Aβ aggregates using Transmission Electron Microscopy (TEM). Aβ aggregate size was detected using Fluorescence Correlation Spectroscopy (FCS). Finally, Aβ β-sheet formation was monitored using a Thioflavin T assay (ThT). My results showed that Aβ was not toxic to cells when cultured in a 3D collagen hydrogel compared to the major cell death seen in 2D cell culture. In the 3D collagen hydrogel, the Aβ very quickly formed large β-sheet aggregates, which I suggest are less toxic than the small unstructured oligomers that are seen in solution. This discovery uncovers an important missing piece that 2D *in vitro* models have missed and may change the way that AD drugs are found and tested.

To further investigate the extent of this phenomenon, **Chapter 4** describes experiments where I tested four different 3D hydrogel types that have varying properties and are commonly used to grow cells *in vitro*. Collagen I and hyaluronic acid (HA) are hydrogels that are part of our ECM, meaning our cells are able to

recognize and bind to them. This binding interaction between the cells and the hydrogel could potentially make the cell less susceptible to the toxicity of Aβ. To test this theory, I also used inert biomaterials that cells do not recognize or bind to: agarose and polyethylene glycol (PEG). Of these four hydrogels, collagen and agarose have the largest "mesh size" – space between the fibers, while HA and PEG have the smallest (Figure 1.3). (One may think about "mesh size" as the spaces between ropes in a cargo net; smaller mesh spaces will trap smaller objects better than larger mesh spaces.) The mesh size of a hydrogel impacts the level of confinement that the protein experiences and may affect Aβ aggregation and toxicity. In the experiments described in **Chapter 4**, I tested the 4 hydrogel types using the same measurements as those I described in **Chapter 3**: ThT, FCS, and cell viability assays were used to study Aβ structure, aggregation, and toxicity. The results showed small differences in Aβ aggregation between the hydrogels; however, despite these differences, all hydrogel types showed no Aβ toxicity to cells. This suggests that the "varying properties" of the 4 hydrogel types mentioned above (including the ability to bind cells and mesh size) promotes less toxic and more stable Aβ fibril aggregates. This information further supports the idea that drugs to treat AD should be tested in 3D *in vitro* cultures rather than the 2D solutions that have been used to date.

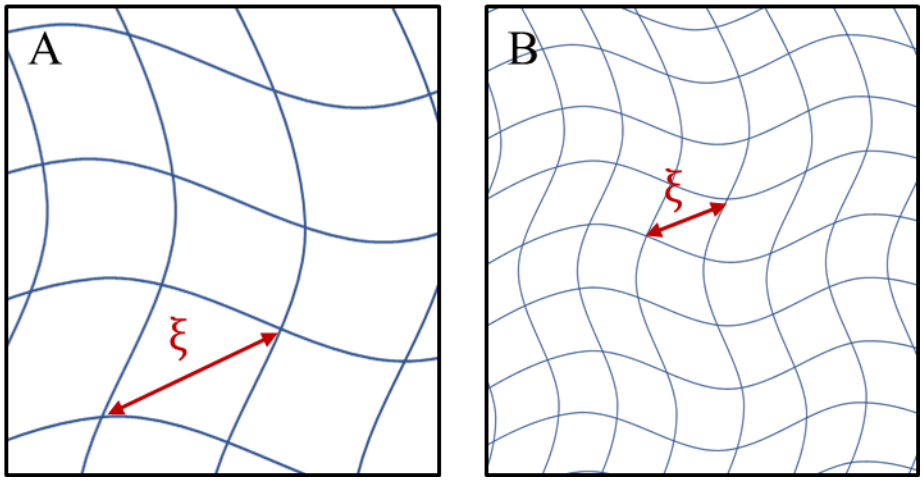

Figure 1.3 The mesh size (ξ) of a hydrogel is the space between the fibers. In A, the mesh size is large, while in B, the mesh size is small.

In summary, this dissertation tells the story of how I discovered a critical fault in the way that new AD drugs have been made. For decades, Aβ has been studied in 2D solutions and *in vitro* cell culture and have led us to believe that Aβ has a potent ability to kill neurons when Aβ exists as unstructured oligomer aggregates. This abundance of data has supported the development of drugs that target Aβ or the ACH pathway but used a test system that may over-estimate the ability of Aβ to cause damage. In these 2D *in vitro* experiments, some drugs have shown promise to protect neurons from dying, yet they failed to be effective in humans. I conclude that the brain is a complex 3D structure. Yet, the field has not realized the fact that such 3D structures confine Aβ differently than in 2D solutions. This confinement alters the size and shape of Aβ and therefore how Aβ can be toxic to neurons. With this new insight, I predict that the use of 3D hydrogels to test AD drugs will result in more effective drugs to combat this devastating disease.

Chapter 2 : Introduction and Motivation

This chapter has been submitted for publication

Protein folding and assembly in confined environments: Implications for protein aggregation in hydrogels and tissues

Introduction

Proteins are the building blocks of life and have highly diverse functions. The biophysical dogma of proteins is that structure predicts function [35-44]: proper protein folding and supramolecular assembly yield appropriate function while misfolding and aggregation yield dysfunction. Indeed, processes of protein folding and aggregation are ubiquitous. Numerous theories and experimental tools have been established during the past century to study structure-function relationships of proteins. While these theories and tools have allowed great understanding of proteins in dilute solutions, extrapolation of protein structure-function relationships determined in dilute solution to their structure and dynamics *in vivo* has been problematic. As a stepping stone between the simplified system of a single component in dilute solution and the complexity of living organisms, scientists and engineers are exploring a number of complex 3D *in vitro* models that are designed to mimic features of the *in vivo* environment. Currently, these models are enabling great advancements in basic science (e.g., to unravel the roles of heterogeneous networks of factors on cellular processes and disease), as well as create new technologies (e.g., biopharmaceuticals designed for greater therapeutic efficacy).

In the early to mid 1900's, new tools to visualize molecular structures were established, notably x-ray crystallography to determine the atomic crystal structure of molecules, electron microscopy (EM) to image specimens that are dried and stained with heavy metals, nuclear magnetic resonance spectroscopy (NMR) to determine molecular structures without crystallization, and light scattering techniques to

characterize molecular sizes and interactions in pure solutions [45-48]. One such method is circular dichroism (CD) which measures changes in polarized light that are signatures of different protein structures depending on the light wavelength: far-ultraviolet (UV) CD measures secondary structure, whereas near UV CD measures tertiary folding. Fourier transform infrared (FTIR) microspectroscopy measures the absorption or emission of IR light associated with secondary structure such as cross β-pleated sheets. Conformational sensitive dyes monitor specific protein conformations; Thioflavin T (ThT) only fluoresces when bound in the grooves of stacked cross β-sheets associated with amyloid proteins. With NMR, the backbone of each amino acid is labeled to identify the localization of secondary structural domains such as β-sheets and α-helixes [32, 49-50]. Identification of protein structure, size and function inform tissue physiology or disease pathology. These methods provided complementary information regarding the molecular resolution of static structures, morphology of static structures, near-molecular resolution of dynamic structures, and dynamic measures of molecular assembly.

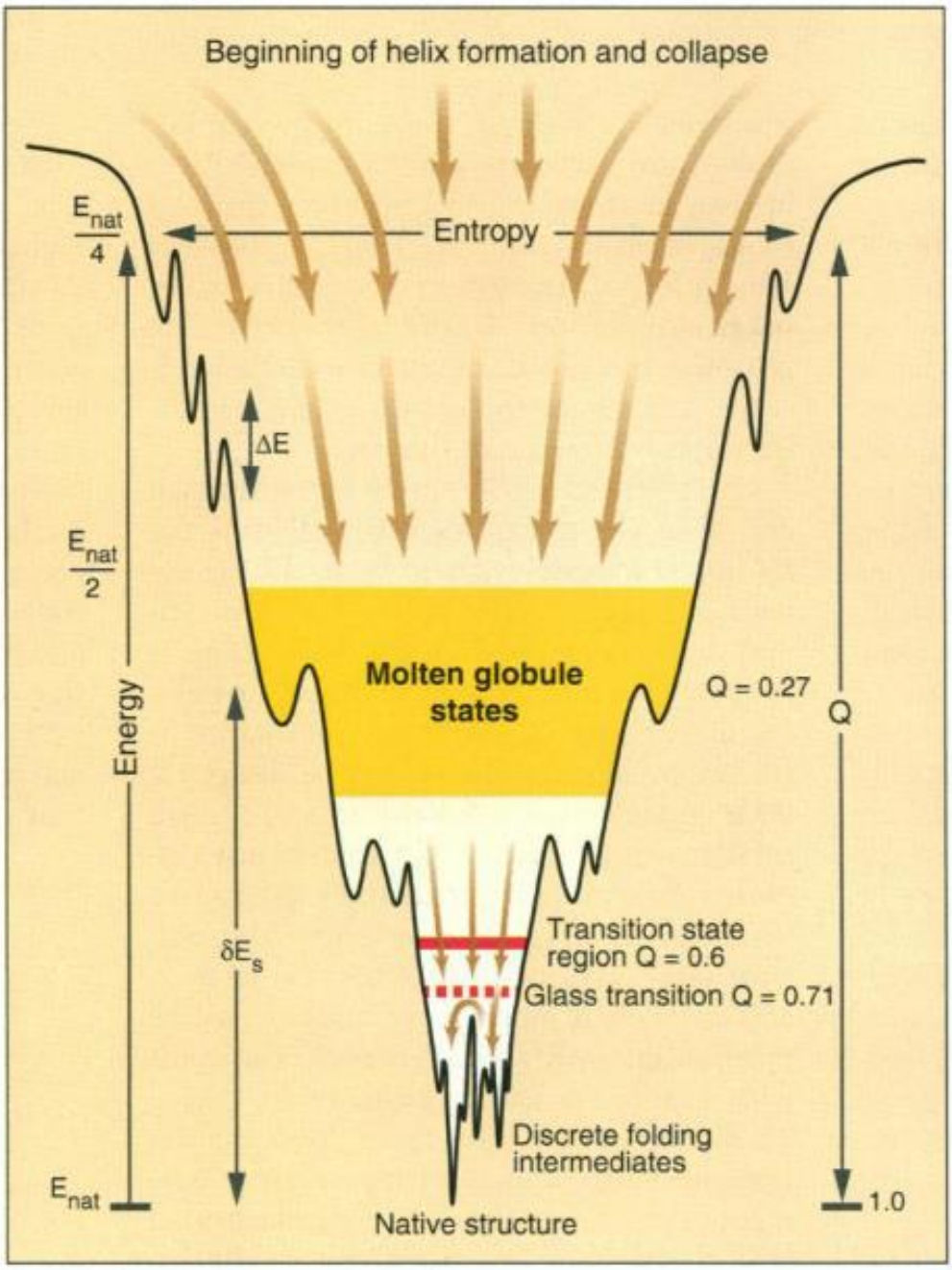

Figure 2.1 Schematic of the folding funnel for a helix forming protein. Reproduced from [51] with copyright permissions from AAAS. The width of the funnel is the entropy; the depth is energy. The fraction of correctly made native contacts is depicted as Q and is listed for each intermediate state down the funnel.

Building on ideas in physics as well as colloidal and polymer science, theorists have described the processes involved in protein folding by models of random packing of hard spheres, lattice statistical mechanics, and the driving forces of hydrophobic interactions and conformational entropy [52-57]. Unfolded proteins are highly disordered and have high entropy; as hydrophobic regions are hidden during folding, the protein takes on a more highly ordered, lower entropy native state (Figure 2.1). Models for protein-protein association and aggregation were developed using similar principles, enabling the prediction of populations of particles in solution [58-61]. These tools were developed for proteins in ideal solutions, and thus it is uncertain whether the findings are reflective of protein structures and function in living organisms. For example, the interior of a cell is a crowded environment where proteins are confined and influenced by their dynamic and heterogeneous local environment. Therefore, to move from ideal solutions towards theories and measurements that better describe protein behaviors *in vivo*, it is critical to consider how a protein's local environment influences its structure and function.

Crowding by a Protein's Local Environment

Solutions in living organisms contain a vast array of macromolecules. Inside the cell, proteins assemble into rigid structures (e.g., F-actin, microtubules, and intermediate filaments) [30, 62] and signaling complexes (e.g., DNA replication complex and RNA replication complex) [63-64]. In the nucleus, proteins condense around DNA, forming chromatin; protein transcriptional and repair machinery

assemble around DNA [65]. Outside the cell, complex heterogeneous matrices composed of collagen, laminin, fibronectin, and other macromolecules aid in maintaining higher order cellular and tissue structures [30, 66]. In these compartments, individual macromolecules only contribute a minute fraction of the total solution volume. However, collectively, the population of macromolecules occupies a substantial fraction (~30%) of the total solution volume [62]. Therefore, observations of proteins in pure dilute solutions do not fully represent how these molecules behave in intracellular and extracellular milieu in which there are substantial ranges in compositions and concentrations. Notably, macromolecules *in vivo* are physically crowded in concentrated "non-ideal" solutions; this crowding has profound effects on protein assembly and stability.

The phenomenon of macromolecular crowding was first applied in the 1940's to describe how proteins precipitate in complex solutions [67-69]. However, protein folding theories at that time approximated the protein population as a set of non-interacting rigid spheres and apply well only to dilute solutions [30-31, 62]. Later, theories such as the available volume theory and the scaled particle theory were developed to better describe the non-ideal behaviors that macromolecules demonstrate in crowded solutions [62, 70-71]. These theories apply the idea that a macromolecule's access to "available" solvent is compromised in crowded high concentration solution; in other words, a volume of solvent is excluded from interacting with the macromolecule. The net effect of this excluded volume of solvent is a reduced available space for a protein to rearrange and fold, thereby provoking a structural state that is compact and low entropy (Figure 2.2). These theories have

been verified experimentally using a variety of crowding factors (e.g., albumin, dextran, polyethylene glycol, and ficoll), which were observed to exclude the protein from interacting with a volume of solvent, thus altering protein folding and function versus what is predicted and observed in “ideal” solutions of pure protein at dilute concentrations [69, 72-77].

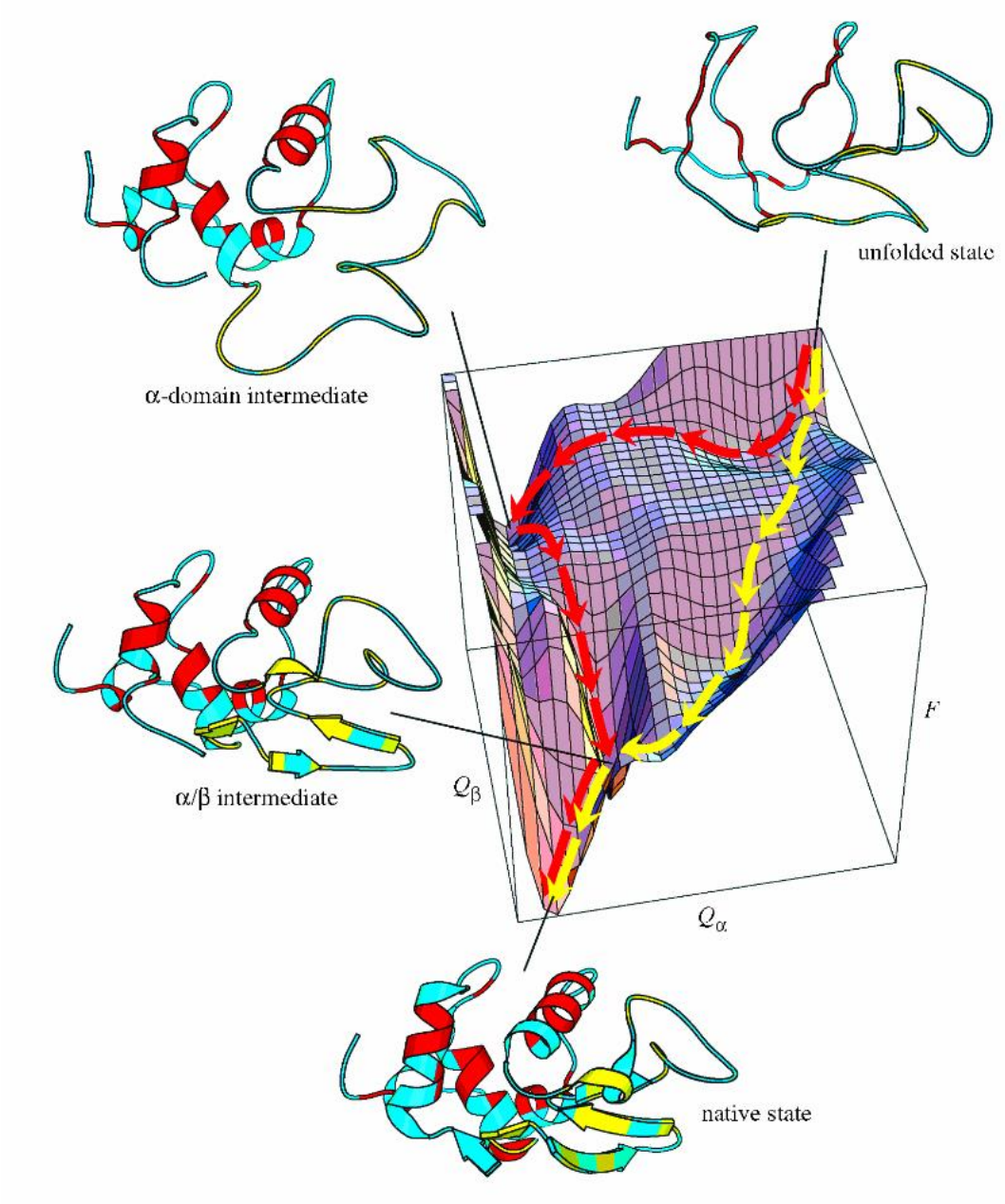

Figure 2.2 Schematic free energy surface (F) of hen lysozyme consisting of two folding domains designated as α and β (red and yellow respectively). The unfolded state has high energy and is highly disordered. As the α and β domains take on intermediate conformations, the energy decreases and the fraction of native

connections approaches unity forming the low entropy native state. Reproduced from [49] with copyright permission from The Royal Society.

These theories that describe macromolecular crowding consider a macromolecule's altered diffusivity and solute-solute interactions that contribute to the non-ideal nature of the solution. Classical methods of measuring the thermodynamic activity (non-ideal correction parameter) of macromolecules in solution include sedimentation equilibrium, osmometry, and Rayleigh scattering of light [62, 78]. The crowding effect is specific to the macromolecular crowder and the intermolecular interactions that arise between crowder and protein; charge, hydrophobicity, viscosity, and rigidity of the crowder (or environment) all play a role [32, 79]. Generally, high concentrations of large molecular weight crowding factors significantly increase protein-protein interactions. However, when the available volume is decreased, molecular interactions become more limited, and thus, the effects from hindered diffusion overcome thermodynamic forces, resulting in reduced rates of enzymatic reactions, protein assembly, and aggregation [30, 80].

Aggregation

Protein aggregation may occur when proteins are misfolded, by exposing sites for non-specific protein interactions, thereby resulting in higher-order structures (e.g., disordered clumps or organized fibrils). *In vivo*, genetic mutations can result in protein structures that are more likely to aggregate than in wild-type organisms, resulting in altered protein function and possibly disease [81-82]. Protein aggregation

rarely occurs in healthy tissues but is often correlated with disease and may readily occur within *in vitro* solutions when protein structure is disrupted or destabilized [83-84].

Aggregation-prone proteins often require a molecular chaperone to avoid unwanted aggregation. The protein lysozyme in pure solution is prone to aggregation, which is exacerbated in the presence of crowders bovine serum albumin (BSA) and ovalbumin. However, when protein disulfide isomerase (molecular chaperone) is added to the denatured lysozyme solution, lysozyme refolds into its native enzymatically active state. This refolding process is accelerated in the presence of crowders due to increased molecular associations between lysozyme and chaperone protein disulfide isomerase [83]. The excluded volume effect stabilizes protein structure; however, the structure may be unwanted aggregation.

As described before, the excluded volume effect imparted by crowding factors stabilizes the lower entropy conformation of the native protein. However, aggregation-prone proteins and intrinsically disordered proteins (IDP) may stabilize lower entropy nuclei for aggregation. In a crowded solution, the effective protein concentration is increased, resulting in a higher likelihood of protein-protein interactions and formation of nuclei, which accelerates the growth of filamentous aggregates [33-34, 79, 85-87].

Intrinsically Disordered Proteins

The importance of IDPs both in normal biological processes and in abnormal pathophysiology is becoming increasingly evident [44, 88-89]. Intrinsically disordered proteins (or regions) lack a defined structure. This conformational freedom allows IDPs to promiscuously bind to diverse partners, playing key roles in protein complex assembly, function and regulation [90]. NMR 3D structural determination has led to the discovery of numerous proteins with functional, yet disordered regions (e.g., Aβ, α-synuclein and prion protein) [44, 82].

IDPs are particularly susceptible to the effect of crowders given their conformational flexibility. As stated above for proteins in general, the crowding effect is specific to the crowder and the intermolecular interactions that arise between crowder and protein; this concept also applies to IDPs [88, 91-94]. To ensure the continued advances in our understanding of IDPs in normal and pathological biological function, IDPs studied *in vitro* must consider well-characterized crowded and confined environments.

Confinement

Protein folding, assembly, and aggregation occur within the cell, at the cell membrane, and in the extracellular space. The terms “crowding” and “confinement” are often misused interchangeably to describe an increase in protein structure stability due to excluded solvent volume accessible for protein folding, resulting in more ordered (lower entropy) protein conformations. However, these terms refer to

different mechanisms by which protein structure and diffusivity are altered by interactions with neighboring molecules or structures: “crowding” is volume exclusion by neighboring soluble macromolecules, but “confinement” is volume exclusion by rigid or fixed structures (Figure 2.3). Said another way, theoretical models of crowding consider effects of varying concentrations of a soluble crowding species, whereas confinement models include molecular meshes, pores, and channels as mimics of cytoskeletal and extracellular matrix structures [87, 95-101].

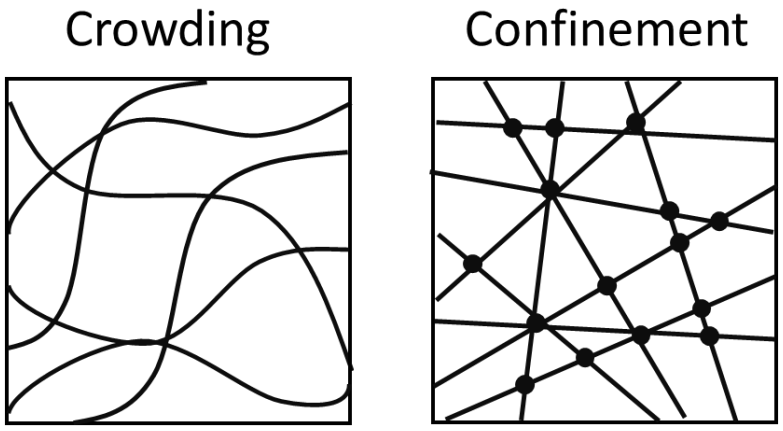

Figure 2.3 Schematic of crowding vs. confinement.
Crowding consists of soluble macromolecules that exclude volume from other macromolecules in the solution. Confinement consists of rigid structures that are crosslinked (black dots at crossing fibers) forming a 3D scaffold.

Because “crowding” and “confinement” are mechanistically different, it follows that these influences have different effects on protein structure. Confining structures limit molecular diffusion to a greater degree than soluble crowders; thus, theoretical models of crowding often predict faster protein diffusion rates than what is measured experimentally in the confined environment existing within a cell. [62, 97,

102]. Other theoretical models suggest that confinement imparts a greater protein folding and stabilization effect compared to crowding [103-106]; this idea is supported by experimental studies reporting that protein confinement within crosslinked alginate imparts a greater stabilization effect on denatured proteins compared to protein crowding within alginate that is not crosslinked [107]. Confinement is a unique phenomenon essential to physiological function that should be incorporated in *in vitro* models to better mimic features of the *in vivo* environment that influence protein structure and function.

This review should be of interest to many areas of research relating to proteins in living systems. These areas include, for example, dimerization of transmembrane proteins, enzymatic activity, assembly of supramolecular structures such as microtubules, disease-related protein aggregation in the ECM and inside the cell, protein therapeutics such as antibody drugs, and even nuclear condensates and membraneless organelles [27, 89, 108-112]. I take inspiration from the experimental and theoretical studies described above to suggest tools and measurement techniques to better mimic properties of the *in vivo* environment relevant to protein structure, folding, and aggregation. As such, I ask: What tools can we adapt from the fields of tissue engineering and hydrogels to create crowded and confined environments? Moreover, what challenges are encountered when applying established biophysical techniques to analyze the structure, function, and aggregation of proteins when they are entrapped in hydrogel scaffolds?

Hydrogels

Hydrogels are ideally suited to mimic key features of tissues for applications as *in vitro* platforms for cell culture, tissue engineering, and drug testing. Hydrogels are derived from natural and synthetic sources and are composed of macromolecules (polymers, proteins, glycans) that interact non-covalently or are crosslinked to form an insoluble macrostructure [23, 113-115]. When applied toward an *in vitro* model or an *in vivo* implant, hydrogels are associated with proteins, and most often, proteins are located within the molecular structure of the hydrogel. Because the molecular properties of hydrogels can be controlled via chemical and physical tools (Figure 2.4), these structures are an ideal platform to probe and tune protein crowding and confinement as vehicles for protein stabilization, formulation and delivery in biopharmaceutical applications, as well as for applications in models of disease (e.g., to determine molecular mechanisms of amyloid aggregation) and models of physiological functions (e.g., enzymatic activity and nuclear condensates containing transcriptional machinery) [22, 116-121].

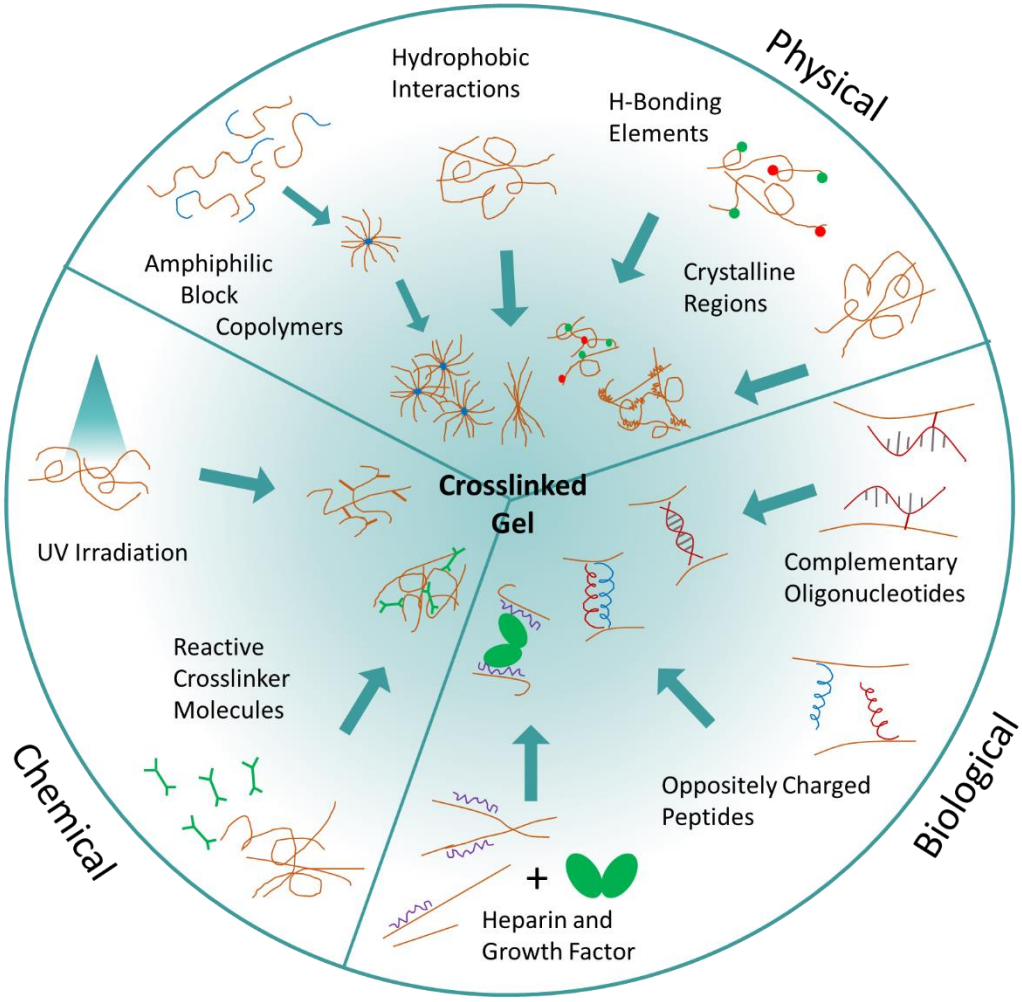

Figure 2.4 Schematic of hydrogel crosslinking capabilities. Chemical, biological, and physical crosslinking options provides tunability for the hydrogel physiochemical and mechanical properties. Reproduced from [122] with permissions from The Royal Society of Chemistry.

When modeling disease, selection of the most appropriate hydrogel model depends on the particular problem being investigated and should consider the heterogeneous compositions and structures that exist within the particular tissue or organ of interest [21, 66, 123]. Further, the structure and function of proteins that exist intracellularly and extracellularly drive cell behavior; therefore, it is essential to

consider how the milieu within a particular *in vitro* model influences protein crowding and confinement.

Both static and dynamic measurements of hydrogel microstructure are informative of the crowding and confinement features of a system. Static measurements give a general insight into architectures such as mesh size and microdomains (e.g., fibers, network heterogeneity). Dynamic measurements may also provide this information, but because they can also provide insight into solute transport within the hydrogel, dynamic measurements are vital for studying protein crowding and confinement.

The architecture of the static hydrogel scaffold can be imaged using atomic force microscopy (AFM), scanning electron microscopy (SEM) and transmission electron microscopy (TEM). AFM is applicable for hydrated or dry samples and may be modified with a receptor functionalized tip to combine topography mapping and molecular recognition mapping [124-125]. However, For SEM and TEM, the sample must be dehydrated; therefore, results may not be representative of the hydrated state of the hydrogel [126]. Static light scattering (SLS), small angle X-ray scattering (SAXS), and neutron scattering (SANS) are more suitable tools to probe the static properties of a hydrogel in its hydrated state [116, 127]. However, hydrogel microstructures are typically not static – molecular interactions and random structural fluctuations will dynamically influence the microenvironment of an embedded protein.

Dynamics of hydrogel microstructures can be characterized by a) analysis of probe diffusion via fluorescence recovery after photobleaching (FRAP) and dynamic light scattering (DLS), b) analysis of microstructure swelling using Flory-Rehner-Huggins theory, and c) examination of mechanical properties by rheology and dielectric relaxation [127-133]. Unfortunately, these techniques are most often incapable of distinguishing between features of the hydrogel and features of the protein because signatures related to the hydrogel typically overshadows the small signal generated by features of individual proteins. Therefore, this review addresses the following related questions: How can I adapt techniques to distinguish structures of a protein from structures of its complex local environment? What new tools could be applied to characterize these structures individually? What insights and opportunities are unveiled through the study of proteins in crowded and confined environments?

Current challenges and opportunities

When adapting analytical techniques to study crowded or confined proteins in hydrogel microstructural environments, the major challenge faced is the potential for the hydrogel itself to interfere with measurements of the embedded protein. It may be tempting to analyze protein extracts isolated from supernatants or digests of the hydrogel. However, considering that conditions of crowding and confinement stabilize proteins into low entropy states, analysis of protein structure should not be performed on extracted protein samples [8, 10, 134-135]. If either the hydrogel itself

can flow or the protein is convectively transported through the hydrogel, it may be possible to apply techniques designed for measurements of a mobile phase such as micro-flow imaging (MFI), field flow fractionation (FFF), and chromatography [134, 136-139]. Yet, most flow techniques require dilute solutions to make accurate measurements. Sample dilution would minimize the excluded volume effect that occurs from crowding and influences protein structure. Acknowledging the importance of analyzing proteins within hydrogels, the following section discusses several analytical techniques suitable for such studies.

Ideally, proteins should be analyzed unperturbed by labels or dyes and within a well-characterized hydrogel environment. The biophysical techniques available that are not dependent upon large fluorescent dyes are limited; these techniques are capable of interrogating protein secondary structure (CD, FTIR), tertiary structure (2D NMR, electron microscopy), and measures of macroscopic aggregation (AFM, scattering techniques). There are limits of applicability of these methods as detailed in the following section, and as such, in some cases, protein labeling may be necessary. Fluorescent labeling, in particular, allows the selective observation of the labeled protein independent of the background material. Techniques such as FRAP, FCS, and fluorescence resonance energy transfer or FRET interpret dynamic fluorescence fluctuations in order to identify individual proteins and their interactions. These techniques do not provide direct measures of the protein but provide indirect measures, either via a measure of diffusion, Brownian motion, or energy transfer, respectively.

CD detects the chirality of a molecule and is commonly used to study protein secondary structure. However many hydrogels used as hydrogel components (e.g., hyaluronic acid, agarose, collagen, polyacrylamide, polylactic acid) have chiral centers, creating a strong CD background signal [23, 49, 101, 140-141]. Achiral polymers (e.g., polyethylene glycol (PEG), polybutylene terephthalate (PBT), polycaprolactone) minimally interfere with entrapped protein CD signal [85, 142]. When using CD to study protein structure, it is crucial to select appropriate achiral biomaterials for the hydrogel.

Fourier Transform Infrared Spectroscopy (FTIR) detects the vibrational spectra of a protein to determine the secondary structure. An infrared light beam passes through the sample and detects the attenuation of the beam [143]. Beam attenuation occurs when light interacts with vibrational transitions in covalent bonds, thereby informing protein secondary structure [144]. FTIR can differentiate between parallel and antiparallel β-sheets as well as native β-sheets vs. amyloid [145-146]. However, this technique is limited to a sample depth of 0.5 – 2 μm [147].

2D NMR is a powerful technique that analyzes the molecular rotational correlation time to identify protein tertiary structure [9, 11]. However, large molecular weight (>25 kDa) proteins and polymers tumble slowly causing increased linewidths and spectral overlap from the large number of unique signals [148]. Protein assembles, and aggregates are not suitable for 2D NMR analysis. Although NMR has been used to characterize amyloid proteins, aggregates are intentionally broken down into monomers to analyze protein structure of a single protein [15].

High-resolution techniques such as AFM and electron microscopy can be used to study protein tertiary structure, but only within a very thin (<150 nm) section or a surface plane of a hydrogel. AFM uses a transducer to measure deflections of a probe that is tapped or dragged across a surface, allowing visualization of the molecular topography at resolutions as small as a fraction of a nanometer. Additionally, AFM may be conducted on surfaces of hydrated samples [149], but cannot probe structure within a 3D material unless thin sections are prepared [150].

Electron microscopy techniques take place under vacuum which requires samples to be dry. SEM captures 10 – 100 nm of depth into the sample with a resolution of 2 nm but requires sample dehydration and a coating of a conductive material. TEM can be used to examine protein structure within a 3D hydrogel but the sample must be resin-embedded, sectioned, and the protein is stained with heavy metal. Electrons are passed through an ultra-thin (~100 nm) section of hydrogel to capture images with subnanometer resolution. In TEM array tomography, serial sections are imaged then reconstructed to generate a 3D image to visualize structures (e.g., protein fibrils) that are larger than the 100-nm thick section [151]. For resin embedding, samples undergo repetitive ethanol and resin washes that compromise the hydrated state of the hydrogel [126, 152] and potentially washes out small molecules from the hydrogel [153]. These treatments may yield samples where smaller protein species are removed, and thus measurements of protein size distribution are skewed towards large protein aggregates. As such, systems meant to mimic *in vivo* milieu require characterization techniques where samples are examined in their hydrated state with negligible washing steps.

It is possible to approximate a hydrogel's structure in its hydrated state by cryo-preservation EM (cryo-EM). In this technique, the water at a hydrogel surface is removed so that the structural detail may be obtained up to 10 – 100 nm deep into the structure. However, removal of water necessarily removes the protein's solvent and likely disrupts the locations of the protein in dry samples vs. when they are hydrated. Prior chemical fixation of the hydrogel may bind the soluble proteins to the hydrogel scaffold, but at this time I am unaware of cryo-SEM studies of small soluble macromolecules when encapsulated in hydrogels.

In TEM, electrons pass through the sample; thus frozen water does not need to be removed. However, when the high energy electron beam hits the ice-organic material interface, a volatile reaction occurs and organic sample is destroyed [154-155]. Samples are vitrified by rapid freezing either by plunging samples into liquid ethane or freezing under high pressures (2100 bar). Vitrification is possible in samples up to 200-μm thick which then can be cryo-sectioned [156]. Cryo-sections of hydrogel can also be imaged dry on support grids. However, thin sections (100 nm) will cut most structures not parallel to the thin plane (protein assemblies and aggregates) making size information unobtainable. In addition, the nanometer scale of proteins and protein assemblies are near impossible to differentiate from the interconnected/crosslinked hydrogel scaffold.

To differentiate protein from hydrogel scaffold, the protein may be labeled with nanoparticles to give contrast to aggregate clusters. The nanoparticle labeling should not to hinder protein diffusion, protein folding or interfere with protein assembly. Nanoparticles <5 nm in diameter cannot be resolved as individual species,

but when clustered, provide sufficient contrast for imaging [157]. It is important to remember, however, that nanoparticles can interfere with protein-protein interactions, such β-sheet structures that stack into large filaments that are associated with amyloid diseases. In these cases, a small ratio of labeled species may be mixed with the unlabeled species to allow enough space between bulky groups to allow proteins to assemble or aggregate [158-159].

Scattering techniques including static light scattering (SLS), dynamic light scattering (DLS), Raman scattering, small angle neutron scattering (SANS), and small angle X-ray scattering (SAXS) are powerful techniques to analyze unlabeled protein structures in pure solutions. These scattering techniques measure fluctuations of light intensity generated when a species undergoes Brownian motion within a focused light beam. However, when the species is a protein is embedded within a hydrogel, the identification of unique signals from the protein vs. the hydrogel can be challenging [134, 146, 160-162]. Hydrogel scaffolds are interconnected networks that are relatively immobile but scatter intensely, while small molecules diffuse quickly and scatter minimally. Scattering techniques have been used to study the behavior of a single non-interacting protein species within a hydrogel scaffold by separating the fast and slow fluctuation times [163-165]. When a heterogeneous mixture of proteins are in a hydrogel scaffold, the intense light scattering signal from the hydrogel and larger species overshadow the weaker signal from the smaller species, making it challenging to differentiate various aggregate sizes.

Fluorophore labeling has been used for decades in various fluorescence microscopy and spectroscopy techniques. The advantage of fluorescence-based tools

is that they detect only the fluorescently-labeled species without interference from other molecules or the hydrogel itself. Live cell imaging can capture the diffusion and interactions of proteins inside a cell, in the cell membrane, and the extracellular space in a hydrogel or tissue. Total internal reflection fluorescence microscopy (TIRFM) characterizes fluorescently-labeled proteins that are located on a glass surface with a maximum imaging depth of ~100 nm from the glass surface [166-167] and a diffraction-limited resolution of ~240 nm. Fluorescence resonance energy transfer (FRET) uses two distinct fluorophores that transfer energy when located within 10-100 Å of each other and are close enough associate [168]. Fluorescence polarization and anisotropy (FP/FA) detect unidirectional light emission and can be used to capture molecular rotation and movement [169]. While some proteins can utilize intrinsic tryptophan or tyrosine fluorescence to measure protein aggregation and conformation [34, 170-172], other species may require labeling with a fluorophore. As with nanoparticles, these labeling techniques can interfere with protein-protein interactions.

Fluorescence correlation spectroscopy (FCS) detects the individual photons of fluorescently-labeled molecules that pass through a very small confocal volume. Photon fluctuation data can be used to generate a correlation function, which can then be used to calculate molecular diffusion and size [173-176]. In cases where fluorophore photobleaching is a concern, raster image correlation spectroscopy (RICS) is similar to FCS but applies multiphoton excitation and rasterized scanning to limit fluorophore exposure to light (Figure 2.5) [177-178].

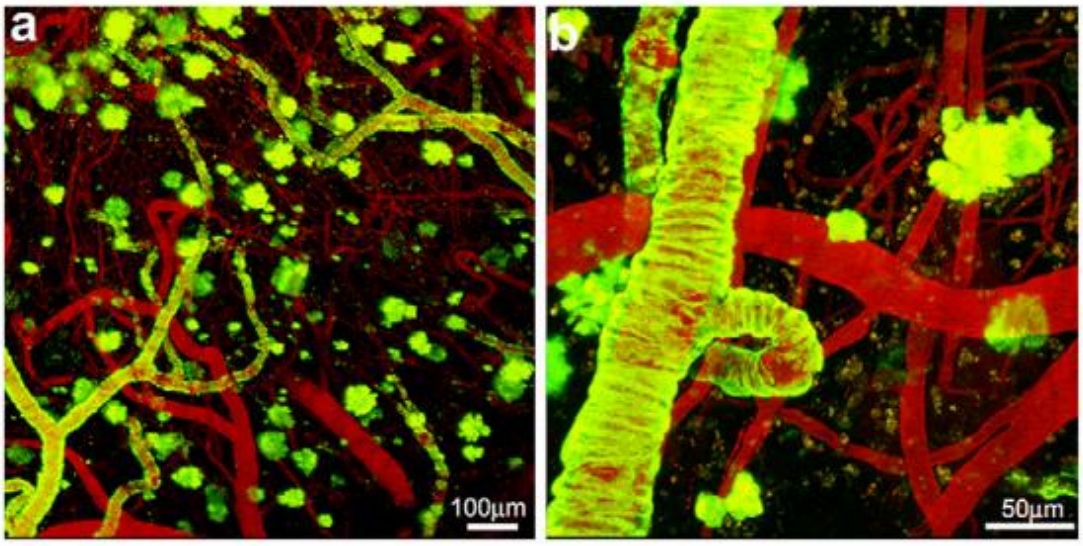

Figure 2.5 Multiphoton in vivo imaging of cerebral amyloid angiopathy. This condition is where Aβ builds up on the walls of arteries in the brain. At low (a, 100 µm scale bar) and high (b, 50 µm scale bar) magnification blood vessels are labeled with rhodamine-dextran (red), and amyloid plaques are labeled with methoxy-X04 (green). Reproduced from [178] with permissions from Elsevier.

Fluorescent or enzymatically-active reporter proteins that are sensitive to aggregation can be expressed in cells to measure protein aggregation that occurs within cells [50, 179]. Also, dyes that are sensitive to protein conformation such as Congo Red (CR), Thioflavin T (ThT), and Thioflavin S (ThS) fluoresce when bound to β-sheet structures. While light microscopy is diffraction-limited to a resolution of ~300 nm, these dyes provide a rather easy-to-use approach to follow protein aggregation kinetics and image large aggregate deposits [50, 180-181].

The development of new fluorescence-based single particle tracking (SPT) and super-resolution microscopy (SRM) techniques allow the study of dynamic

protein interactions resolved at <100 nm. SRM uses illumination patterns or fluorescence photo-switching to overcome diffraction limitations. An excellent example of enhancing fluorescence resolution is demonstrated by Li et al., where traditional TIRFM was demonstrated to resolve features as small as 220 nm, TIRF-structured illumination microscopy (SIM) can resolve 97 nm features, and patterned activation of a reversibly photo-switchable fluorescent protein using non-linear SIM (PA NL-SIM) resolves 62 nm features (Figure 2.6) [182]. Combining cryo-EM with SRM can achieve resolutions of <100 nm to yield images with high structural detail and identification of specific species by fluorescence [183].

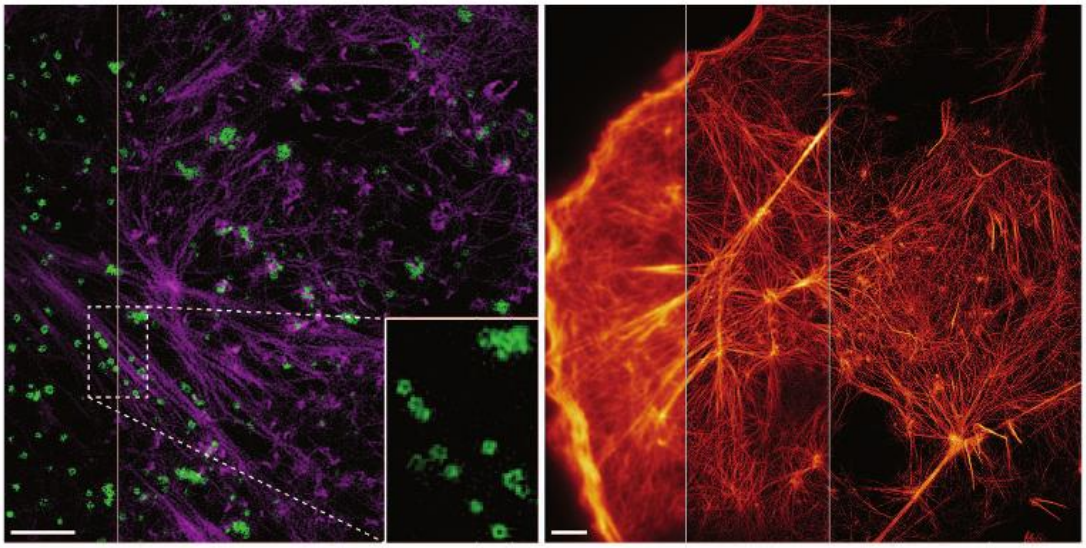

Figure 2.6 Two methods to enhance fluorescence resolution.

On the left, cortical actin (purple) with clathrin-coated pits (green). A resolution of 84 nm via ultrahigh numerical aperture TIRF-SIM captured the rings of the clathrin-coated pits. On the right, the progression of resolution of the actin cytoskeleton from diffraction limited TIRF (220 nm), to TIRF-SIM (97 nm), and finally non-linear SIM with patterned activation using reversibly photoswitchable fluorescent protein (PA

NL-SIM, 62 nm resolution). Scale bars, 2 μm (left); 3 μm (right). Reproduced from [182] with permissions from AAAS.

SRM techniques and SPT have shed light on transcription factors (TF) and their dynamic functions. TFs assemble to form the transcription preinitiation complex through a multi-step process, but little is known of the dynamics of assembly. TFs also contain intrinsically disordered regions (IDRs) that regulate transcription, but underlying mechanisms are unclear. By live-cell slimfield single molecule imaging, stochastic optical reconstruction microscopy (STORM), FCS, and lattice lightsheet microscopy, IDRs have been visualized to cluster into oligomeric assemblies, forming liquid-liquid phase transitions, stabilizing DNA binding, recruiting RNA polymerase, and activating transcription [184-185].

Many SRM techniques require long capture times and high photon input. Movement can yield false results; therefore, specimens can be fixed to capture higher quality images [186]. SPT in live cells tracks the dynamic movement using EM-CCD cameras that have high frame rates and high aperture objectives to capture freely diffusing proteins. Combining SRM techniques such as SIM or stimulated emission depletion (STED) with SPT obtains the ultimate spatiotemporal tracking resolution. MINFLUX tracking uses STED concepts with 80% reduced photon input, which minimizes photobleaching, and has achieved a resolution of 6 nm [186-187]. Current drawbacks of SPT and SRM include limited viewing at depth and of larger samples, many require static, fixed samples, and many require specialized fluorophore labeling.

Concluding remarks and perspectives

Tissue development, disease, and repair involve highly complex and dynamic processes. Though the *in vivo* scenario is ultimately the most relevant to understand, *in vitro* models allow control of the composition and spatial arrangement of cells and biologically-active molecules with specificity not possible in living organisms. In these complex 3D models, cellular behaviors have been the primary subject of interest, whereas investigations of protein stability, structure, and assembly have been relatively limited. Yet, environments both inside and outside cells are composed of protein structures that drive cellular behavior and shape tissues properties (e.g., stiffness, local charge, pH, and gradient features). The ECM also contains various motifs that are involved with cell binding, gene activation, and protein-protein interactions (e.g., sequestration of growth factors, localization of mitogens and cytokines).

Simple identification of the presence or general location of a protein can be accomplished through fixation and immunolabeling. However, the definition of protein structures in dynamically interacting systems requires real-time tools that can detect features within the three-dimensional hydrated structures of cells, tissues, and hydrogels. As reviewed herein, many analytical tools to study protein structure in solutions can be extrapolated for use within hydrated structures. However, delineation between signals from the protein of interest vs. its physical microenvironment can be very challenging. Advanced tools and approaches that apply to the contexts of crowded and confined microenvironments will undoubtedly shed new insights into

protein structure, folding and aggregation processes that will advance our understanding of disease states and the stability of biopharmaceutical drugs.

Chapter 3 : Collagen hydrogel confinement of Amyloid-β (Aβ) accelerates aggregation and reduces cytotoxic effects

This chapter has been submitted for publication

Introduction

Amyloids are defined as abnormal fibrous, extracellular, protein aggregates that accumulate in organs throughout the body. Native proteins misfold, and intrinsically-disordered proteins fold predominantly into a β-sheet conformation. Under certain conditions the β-sheet structure extends, leading to the formation of amyloid fibrils; this aggregation process either leads to loss of function of the native protein or gain of toxic function of the aggregated amyloid protein. There are currently 37 human amyloid proteins identified that are linked to neurodegenerative diseases and amyloidosis diseases [81-82]. Alzheimer's disease (AD) is the most common form of dementia [16] and is associated with the accumulation of amyloid-β (Aβ), and intrinsically disordered peptide between 39 to 45 amino acids long in its native form, whose aggregation has been associated with neurotoxicity in AD [188].

Since the first studies demonstrating a genetic link between Aβ and early-onset AD [189], investigators have targeted Aβ as a potential therapeutic strategy. Neurology has the third highest number of medications in drug development, yet there are only four unique drugs approved by the FDA for the treatment of AD [17]. Between 2002 and 2012 there were 413 clinical trials for AD. During that time only one drug was licensed by the FDA, a 99.6% failure rate [20]. Many AD drugs are Aβ targeting antibodies that demonstrated great promise in pre-clinical trials and mouse models yet failed to show efficacy in human patients [190-191].

There are a number of possible causes for the failure of Aβ targeting drugs in clinical trials. Aβ may not be causative in AD, but instead may simply be a side-product of the disease progression. The clinical trial design may be faulty in that drug intervention is administered in late-stage AD while Aβ toxic effects occur significantly before (potentially decades before) the onset of symptoms. Clinical endpoints are subjective, making it difficult to determine the efficacy of any intervention. Alternatively, the 2D tissue culture models used to screen drugs for their ability to attenuate Aβ toxicity are poor models for the *in vivo* 3D environment. Some or all of the above hypotheses may be valid; however, in this study, I set out to test the last hypothesis, that 2D tissue culture models are a poor model for Aβ toxicity testing.

In vitro models typically culture cells on a 2D surface to study the cellular response to Aβ [192-197]. However, 3D biomaterial scaffolds promote stem cell differentiation, cellular binding, and cell signaling that better represent *in vivo* cell behaviors compared to 2D cultures [24-25, 123, 198-203]. There is a growing trend across all of biotechnology and biopharmaceutical discovery teams to use 3D models of tissue as opposed to 2D tissue culture models, with remarkably good results [204-206]. 3D AD models have begun to be used to model the human cellular aspects that mouse models inherently cannot. [207-210]. Some of these 3D models have even used iPSCs taken from an AD patient and differentiated them into neurons that produced Aβ and eventually tau tangles [110, 209-210]. However, these models have yet to be used routinely for drug testing.

3D environments such as collagen hydrogels used in tissue culture models form a confined space that excludes solvent volume from soluble macromolecules [22-23, 66]. Volume exclusion reduces the space available to an unfolded protein, thereby shifting the equilibrium towards a more compact protein conformation. For most proteins, the native state is a compact conformation [32, 62, 70-71, 97, 104, 107]. However, with intrinsically disordered proteins and other aggregation-prone proteins, confinement promotes rapid aggregation [30, 33-34, 83-86, 211]. Even for free, uncrosslinked crowding materials, the solvent exclusion effect has been observed experimentally [33, 85] and predicted from simulation [212-213]. However, whether this effect leads to amorphous (off-pathway) aggregation [214-215], or stabilization of on-pathway intermediates [216], is unclear as conflicting results have been reported [217]. Further, for hydrogels used as cell scaffolds (e.g., collagen) the influence of 3D environments on protein structure and aggregation is equally unclear.

From studies carried out in solution and 2D culture models, I know that Aβ aggregation is intimately tied to its cytotoxicity. Unstructured Aβ monomers associate with each other, forming unstable oligomers that are associated with neuronal toxicity [10-11, 218-220]. Fibrils and other protofibril structures are thought to be less toxic [11-12, 221]. While it is commonly held that the unstable toxic oligomers are an "on pathway" intermediate, there are some dissenting opinions [222]. Thus, a priori, it is difficult to predict the effect of 3D confined environments on the relative distribution of Aβ structures associated with aggregation and toxicity.

In this work, I tested the hypothesis that Aβ toxicity is altered for cells cultured in 3D hydrogels vs. 2D cell culture plates. I show that Aβ aggregates more readily in the 3D confined environment of a hydrogel. I suggest the differences in toxicity between 2D and 3D cultures are a result in a shift in chemical equilibrium from oligomer to fibril, and from toxic to less toxic species, in these environments. Finally, I propose that some clinical trials of AD drugs fail as a result of the differences in the biophysical environment in 2D culture and the *in vivo* environment; therefore, I suggest that future Aβ toxicity studies be conducted in 3D hydrogel cultures so that the biophysics of Aβ aggregation better approximates the *in vivo* scenario.

Materials and Methods

Amyloid-β Preparation

Human amyloid-β (1-42) (Aβ) and scrambled Aβ (1-42) (Scr Aβ) (*AIAEGDSHVLKEGAYMEIFDVQGHVFGGKIFRVVDLGSHNVA*) was purchased from AnaSpec (Fremont, CA) and Genscript (Piscataway, NJ). HiLyte 488-labeled Aβ (1-42) (HiLyte Aβ) and FAM-labeled scrambled Aβ (1-42) (FAM Scr Aβ) were purchased from AnaSpec (Fremont, CA). All other unspecified reagents were purchased from Sigma Aldrich (St. Louis, MO) or Thermo Fisher Scientific (Waltham, MA).

In order to break any existing β-sheet structures and monomerize the protein, lyophilized Aβ was pretreated with hexafluoro-2-propanol at a concentration of 1

mg/ml for 40 mins until Aβ was fully dissolved. Aβ aliquots were transferred into glass scintillation vials, and hexafluoro-2-propanol was evaporated under vacuum overnight. Aliquots of dried peptide film were stored at -20°C. For an experiment, an Aβ aliquot was dissolved in freshly-made and filtered 60 mM NaOH and allowed to dissolve for 2 mins at room temperature. Tissue culture grade water was then added, and the vial was sonicated for 5 mins. The Aβ solution was then filtered with a 0.2-μm pore, 4-mm diameter syringe filter. Sterile phosphate buffered saline (PBS) was then added to the Aβ monomer solution yielding a final concentration of 222 μM with the NaOH:water:PBS ratio of 2:7:1. The Aβ solution was used immediately after preparation. HiLyte Aβ and FAM Scr Aβ were prepared in the same NaOH:water:PBS ratio solution to a stock Aβ concentration of 10 μM. All FCS experiments used 250 nM fluorophore-labeled Aβ.

Hydrogel Preparation

Rat tail Type I collagen hydrogels were prepared to final concentrations ranging from 0.5 to 2 mg/ml. Cold 5x Dulbecco's Modified Eagle's Medium (DMEM) without phenol red, 7.5% sodium bicarbonate, sterile deionized water, and collagen were combined with PC12 cells to generate 3D substrates in black walled clear bottom well plates. The hydrogel solution (containing cells) was placed in a culture incubator for 20 mins to allow for gelation and then culture medium was added.

Cell Culture

PC12 cells (ATCC, Manassas, VA) (CRL-1721TM) were cultured on in collagen-coated flasks. Growth medium consisted of DMEM/F12 with L-glutamine and without phenol red, supplemented with 10% inactivated horse serum, 5% fetal bovine serum, and 20 μg/ml gentamicin. The experimental medium consisted of Neurobasal medium without phenol red, supplemented with 1% B27 and 10 μg/ml gentamicin. Phenol red and serum were avoided in the experiments because they are inhibitors of Aβ aggregation [223-224].

Live/Dead Assay

PC12 cells were collected by trypsin treatment, and viability was determined by trypan blue staining. To remove serum, cells were resuspended in experimental medium, pelleted then resuspended again in experimental media. In a black-walled clear-bottom tissue culture treated 96-well plate, wells for 2D culture were collagen coated, and then PC12 cells were seeded at 15×10^3 cell/cm^2. For the 3D hydrogels, PC12 cells were mixed in collagen gel solution at a concentration of 500 cell/μl; the solution was then pipetted (30 μl) into the well plate and allowed to solidify. All wells were incubated in 200 μl warmed medium. The medium was not changed during the 72 hr experiment.

To determine cell viability, the Live/Dead mammalian cell kit (Invitrogen, Carlsbad, CA) was applied at a concentration of 4 μM Calcein AM (green-fluorescing live cell reporter) and 9 μM Ethidium homodimer-1 (EthD) (red-fluorescing dead cell

reporter) and incubated at 37°C for 30 minutes. Images were taken on an IX81 Olympus inverted fluorescent microscope. A minimum of 100 cells were counted per well, two images per well, three wells per condition. The data is presented as percent viability, averaged between the three replicate experiments. An ANOVA Tukey pairwise test determined significant deviation from the population mean with a p-value less than 0.05 with 95% confidence.

Thioflavin T

A black-walled clear-bottom 384 well plate (Costar) was sterilized under UV light for 15 minutes in a laminar flow hood. UltraPure grade Thioflavin T (ThT) (AnaSpec, Fremont, CA) was dissolved in deionized water at a concentration of 1 mM then filter-sterilized. Wells for 2D and 3D samples were prepared as above, but containing 20 μM ThT. The wells were sealed with black TopSeal-A membranes to prevent evaporation. The ThT experiment was analyzed on a Spectra Max M5 (Molecular Devices, San Jose, CA) spectrophotometer set to ex. 450 nm, em. 480 nm, at 37°C, taking reads every 30 mins for 72 hrs, reading from the bottom of the plate. Replicates were averaged, Aβ data was corrected with ThT control data, and corrected curves were normalized. Due to the stochastic nature of aggregation, representative curves are presented here.

Transmission Electron Microscopy

Samples for transmission electron microscopy (TEM) imaging were prepared as follows. Reconstituted 222 μM Aβ was diluted to 20 μM in experimental media. Timepoints were taken at 0, 24, 48, and 72 hrs. Samples were prepared on copper-supported carbon formvar grids (FCF200-Cu-TB) (EMS, Hatfield, PA) and stained with 0.2% uranyl acetate. Grids were imaged at 180-220 kx on an FEI Morgagni M268 100 kV Transmission Electron Microscope equipped with a Gatan Orius CCD camera.

Fluorescence Correlation Spectroscopy

Theory

Fluorescence Correlation Spectroscopy (FCS) measures the fluctuations of fluorescence in a small, optically-defined confocal volume (~10^{-15} liter). These fluctuations are typically attributed to the fluorescent particles moving in and out of the volume with a statistical average residence time, τ_D. The residence time is proportional to the hydrodynamic radius (R_H) of the molecule. The fluctuations of detected photons inform the autocorrelation, $G(\tau)$, function defined as

$$G(\tau) = \frac{\langle \delta I(t+\tau)\delta I(t)\rangle}{\langle I(t)\rangle^2}$$

Where $\delta I(t) = I(t) - \langle I(t)\rangle$ is the fluorescence fluctuation determined from the measured fluorescence intensity, $I(t)$, at time t, and the average intensity, $\langle I(t)\rangle$, over the period of measurement. The excitation laser, which is focused, is assumed to

have a 3D Gaussian profile, with a characteristic radial dimension (w_0) and a characteristic axial dimension (z_0). For a solution of n noninteracting, freely diffusing fluorescent species $G(\tau)$ is given by:

$$G(\tau) = \sum_{i=1}^{n} b_i \left(\frac{1}{1 + \frac{\tau}{\tau_{D_i}}} \right) \left[\frac{1}{1 + \left(\frac{w_0}{z_0}\right)^2 \frac{\tau}{\tau_{D_i}}} \right]^{1/2}$$

$$\tau_{D_i} = \frac{{w_0}^2}{4D_i}$$

Here the D_i values are the n different values of diffusion constants and b_i are the relative fractions in brightness of these species. In practice, the radial and axial dimensions were determined using Alexa 488 dye in water where the diffusion coefficient (430 $\mu m^2/s$) is known and was used to estimate the excitation volume for a 3D Gaussian beam [225].

Methods

Neurobasal medium was used in preparing solution samples and contained 20 μM Aβ and 250 nM HiLyte Aβ. Collagen hydrogels were prepared as described with 20 μM Aβ and 250 nM HiLyte Aβ then pipetted into 0.8-mm deep hybridization chambers (PerkinElmer, Waltham, MA) on a borosilicate cover glass. Control samples were tested with 20 μM Scr Aβ and 250 nM FAM Scr Aβ.

The FCS measurements were performed using an Alba-FFS microscope-based system from ISS Inc. (Champagne, IL). The system is composed of: an Olympus

IX81 inverted microscope equipped with a 60X/1.35NA oil immersion objective lens, a Prior Pro stage, three different lasers (450 nm, 488 nm, and 532 nm), two Hamamatsu Photon Multiplier tubes (PMTs) for photodetection, and two sets of computer-controlled scanned mirrors for imaging. In these measurements, only the 488-nm diode laser was used for excitation of the fluorophores Alexa 488 or fluorescently-labeled Aβ, and the emitted fluorescence was collected through confocal detection with a pinhole (< 50 mm) located in the image plane of the excited focused beam inside the sample. The emitted fluorescent beam was optically filtered further with (525/50nm) filter and then sent to a 50/50 beam splitter for detection by two PMTs positioned in a 90-degree angle configuration. The photocounts of both PMTs were continuously acquired and then computationally cross-correlated in order to eliminate the afterpulsing effect of a single PMT, which is typically noticeable at short delay times (< 10 ms).

Using Vista Vision software, two runs were carried out back to back collecting for 3 minutes each to generate the correlation function G(τ) for each sample at a time point. The two correlation functions were averaged, and the Scr Aβ correlation function was fit using the one-component model to determine the diffusivity of the monomer. Further, the measured time point correlation functions for Aβ were fit using the 2-component model where the size of species 1 was held constant at monomer diffusivity in order to derive the average aggregate diffusivity population of the second species. Additional refinement for fitting the correlation functions were also performed with the Maximum Entropy Method FCS (MEMFCS) thanks to a code gifted by Dr. S. Maiti (Tata Institute of Fundamental Research),

allowing us to obtain the heterogeneous distribution of aggregate diffusivities at each time point [176].

Small molecules have a short delay time because they diffuse quickly through the volume, whereas large molecules have a long delay time because of their relatively slow diffusion through the volume. The 2-component model is intended to model two distinct molecular species in solution. For my samples, I held the monomer diffusivity constant as species 1 where the average diffusivity of aggregated species was identified by solving for species 2.

Fluorophore labeling of Aβ monomers inhibits aggregation due to the bulky groups sterically preventing proper monomer to monomer stacking [159]. Therefore, I used a ratio of 1:80 HiLyte 488-labeled Aβ to unlabeled Aβ, and FAM-labeled Scr Aβ to unlabeled Scr Aβ, to allow unhindered β-sheet stacking. Nanomolar fluorophore concentrations are also preferable in FCS in order for the detectors to monitor few individual fluorescent molecules in the confocal volume, enhancing hence the signal-to-noise of the fluctuations.

Results

Toxicity of Aβ in 2D and 3D cultures

I initially hypothesized that 3D hydrogels would be better models in which to test Aβ toxicity because neurons have a more *in vivo* like phenotype in 3D compared to 2D cultures [25, 226]. As such, I expected Aβ to be more toxic to cells in 3D than

in 2D. To begin to test this hypothesis, I examined the toxicity of PC12 cells when dosed with Aβ (pretreated to remove β-sheet structure) in both 2D and 3D collagen over a 72 hr period.

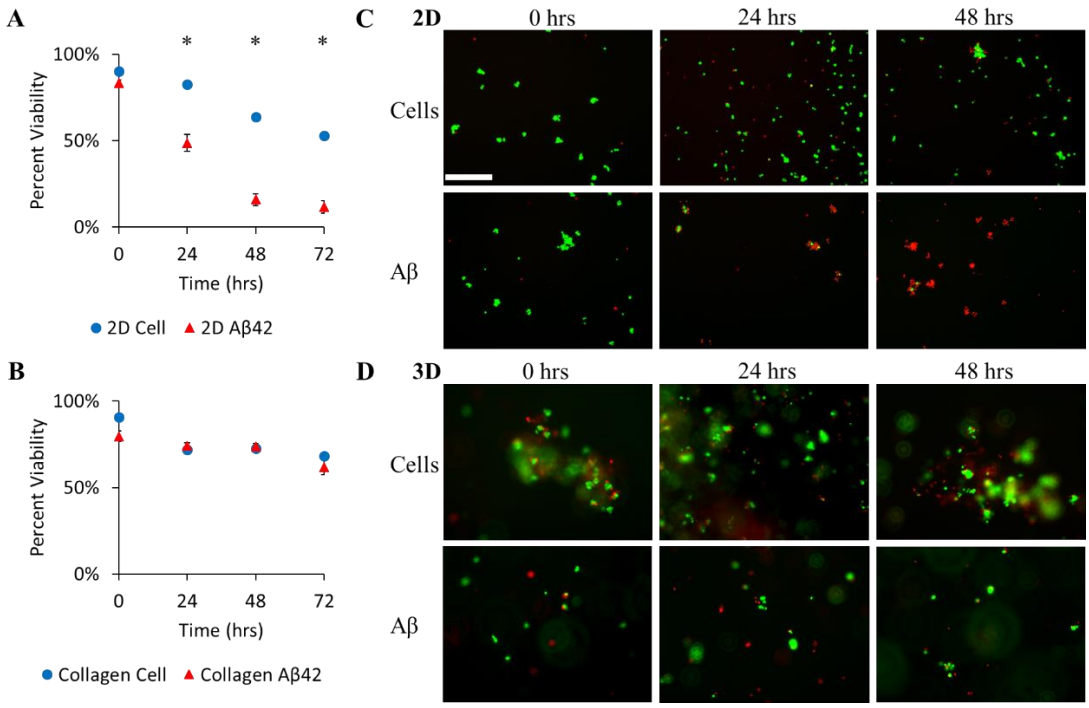

Figure 3.1 PC12 cell percent viability using a Live/Dead assay.

Cells were cultured without Aβ (A & B, blue), or with 20 μM Aβ (A & B, yellow). Cells were imaged in 2D (C) and 3D (D), without Aβ and with Aβ, where live cells appear green (Calcein-AM), and dead cells appear red (EthD). Significant differences were seen in (A) 2D culture in the presence of Aβ at 24, 48, and 72 hrs signified by (*). Statistics used n = 4. P values at significantly different times in 2D culture: 24 hrs (0.004), 48 hrs (<0.001), and 72 hrs (<0.001). Error bars are the percent error of the mean population. Scale bar is 200 μm; all micrographs are the same magnification.

I acknowledge that the percent viability decreases for all samples over time, but it is important to note that the medium was not changed in order to preserve the Aβ aggregation environment. Over 72 hrs, cell waste may build up, and nutrients may run low; this would explain the decrease in cell viability in all conditions. The number of viable cells cultured in 2D with 20 μM pretreated Aβ decreased significantly by 24 hrs where the cell viability was 49% (p-value 0.004); at 48 hrs and 72 hrs the cell viability was only 16% (p-value <0.001) and 12% (p-value <0.001) respectively (Figure 3.1A). When cells were encapsulated within 3D collagen hydrogels, treatment with Aβ did not affect cell viability (Figure 3.1B). Representative fluorescence microscopy images of stained cells at 0 hrs, 24 hrs, and 48 hrs in 2D and 3D culture are shown in Figures 3.1C and 3.1D respectively. In the presence of Aβ, the cell death (red staining) at 48 hours in 2D culture is striking (Figure 3.1C), while no notable increase in cell death is observed in the Aβ-treated 3D cultures (Figure 3.1D).

TEM imaging of Aβ in solution

Given the well-known correlation between Aβ structure or aggregation state and toxicity, I sought to confirm that the Aβ used in these studies aggregated as expected and that the surprising cell viability results were not the result of some anomalous aggregation process. To this end, I performed TEM imaging of the pretreated Aβ at time points after dissolution relevant to the viability studies.

Representative TEM micrographs are shown in Figure 3.2. At time zero, unstructured protein globules of various sizes were identified (Figure 3.2A). The smallest structures have a diameter of ~3.6 nm, which correlates well to the size of Aβ monomer (hydrodynamic radius of 1.8 nm) [227]. Larger globular structures are 6 - 50 nm in diameter and lack any fibrillar structures. At 24 hrs, thin filamentous aggregates (~3 nm diameter) are seen to extend from the unstructured globules (Figure 3.2B). By 72 hrs, thick Aβ fibrils are present and associate with each other into structures ~13 nm in diameter (Figure 3.2C).

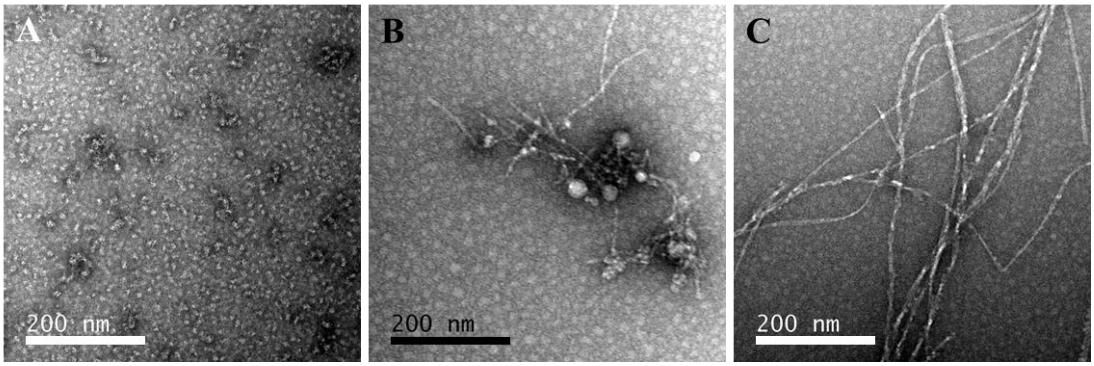

Figure 3.2 TEM images of 20 μM pretreated Aβ in solution.

Samples were stained with 0.2% uranyl acetate at time 0 hrs (A), 24 hrs (B), and 72 hrs (C).

Aβ aggregate diffusivities by FCS

Given the inherent challenges of imaging hydrogels using TEM, I utilized FCS to infer relative Aβ aggregate size from the diffusivity of fluorescently-labeled

Aβ species. Diffusivity scales inversely to the radius of a particle. Therefore small diffusivity values correspond to large particles.

Non-aggregating Scr Aβ was measured in solution and hydrogels as a monomer control. The diffusivity of these Scr Aβ monomers in solution was determined to be 175 $\mu m^2/s$, whereas the diffusivity in the hydrogel was 129 $\mu m^2/s$ (Figure 3.3A & B). As points for comparison, the diffusivity of Aβ monomer has been reported to be 180 $\mu m^2/s$ in solution and 62.3 $\mu m^2/s$ in brain tissue [153]. In solution, the diffusivity of the average Aβ aggregate population (determined using the 2-component model) is ~9x slower than the monomer for up to 6 hrs (Figure 3.3A). In hydrogels, the diffusivity of the average Aβ aggregate population is ~150x slower than a monomer for up to 4 hrs (Figure 3.3B).

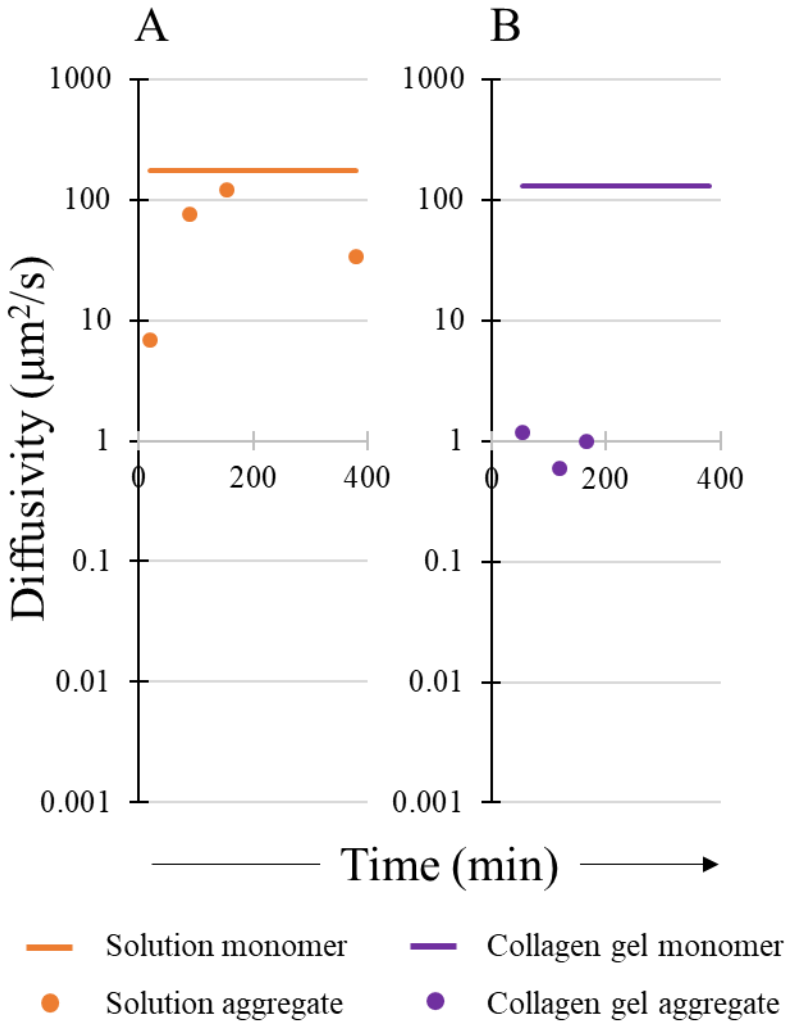

Figure 3.3 FCS G(τ) fit with a 2-component model.

The correlation function (G(τ)) was obtained from 20 μM Aβ with 250 nM HiLyte Aβ in solution (A, orange symbols) and collagen hydrogel (B, purple symbols). Species 1 was held constant at the diffusivity of the Scr Aβ control assumed to be monomer (solid line). Species 2 was calculated and represents the average Aβ aggregate diffusivity population (circles). The values of Scr Aβ diffusivity are displayed as solid lines, and the average aggregate species are displayed as circles.

The correlation functions were also analyzed using the MEMFCS program, which attempts to determine the distribution of size of the aggregating solutions. A distribution of multiple diffusivity populations of Aβ aggregates and their relative fractions were modeled. In solution, Aβ diffusivity values have a single broad distribution with an average peak diffusivity of 90 $\mu m^2/s$ (Figure 3.4A). The peak diffusivity of Aβ in solution is ~2x slower than the Scr Aβ diffusivity, suggesting an Aβ population predominately composed of dimers. In the hydrogel, Aβ has a peak diffusivity of 60 $\mu m^2/s$, which is ~2x slower than the Scr monomer (129 $\mu m^2/s$). However, in contrast to the solution samples that only have one diffusivity peak, the hydrogel sample data show a small secondary diffusivity peak as early as 5 mins after addition of Aβ to the hydrogel and persists throughout the measurement period (up to 4 hrs) with diffusivity values in the range of 0.2 $\mu m^2/s$ to 3 $\mu m^2/s$, or between 650x to 45x slower than Scr Aβ (Figures 3.4B).

Both analysis methods of the FCS data indicate that Aβ aggregates differently in 2D compared to 3D. Based on these data, a rough estimate of aggregate species size in 3D is ~25x to 200x larger in diameter than the Aβ species detected in 2D.

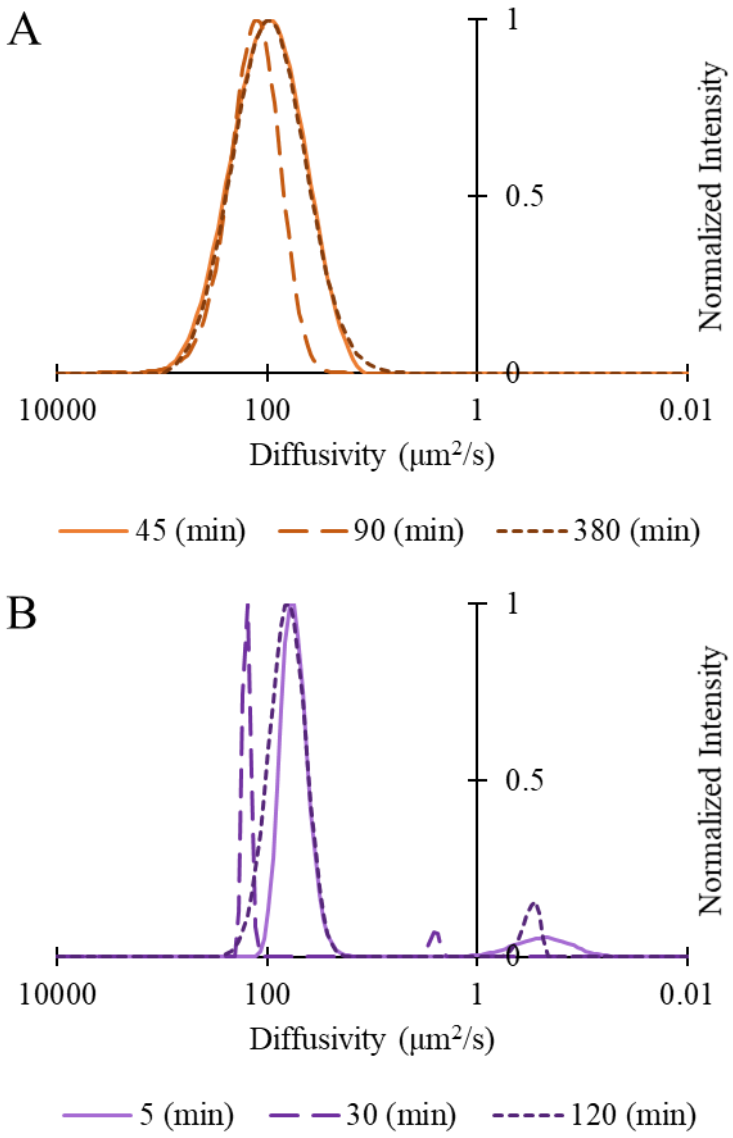

Figure 3.4 FCS G(τ) modeled as population distributions.

FCS G(τ) fit of 20 μM Aβ with 250 nM HiLyte Aβ using the MEMFCS program generously gifted by Dr. S. Maiti [228]. In A, solution time points were collected at 45 min (solid line, light orange), 90 min (long dash, medium orange) and 380 min (short dash, dark orange). In B, collagen hydrogel timepoints were collected at 5 min (solid line, light purple), 30 min (long dash, medium purple), and 120 min (short dash, dark purple).

ThT fluorescence as a measure of Aβ aggregation kinetics

While FCS is a powerful technique to measure diffusivities of molecules in complex media, it is difficult to get direct information on the structure or morphology of an aggregated species. Therefore, I used a ThT fluorescence assay as an additional measure of Aβ aggregation.

Representative curves of ThT fluorescence vs. time are shown in Figure 3.5 for Aβ aggregation in solution and collagen hydrogels. In solution, fibrillar Aβ aggregation (signified by ThT fluorescence) has a lag phase during the first ~20 hrs, followed by rapid aggregation (Figure 3.5, orange). In hydrogels, however, fibrillar aggregation does not show a lag phase, and instead, fluorescence steadily increases from the initiation of the experiment (Figure 3.5, purple). Depending upon the supplier and lot of Aβ tested, these curves lag time, and fluorescence intensity varied, but the qualitative differences between fibril Aβ aggregation in solution and the collagen hydrogel persisted; fibril aggregation was accelerated in the hydrogel compared to the solution.

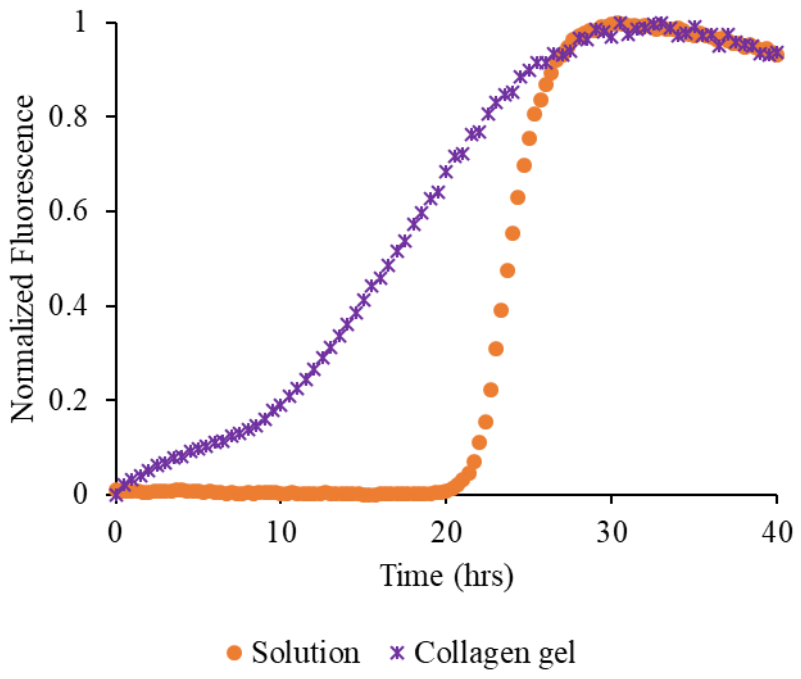

Figure 3.5 ThT Aβ aggregation kinetics in solution vs. collagen hydrogel. ThT fluoresces only when bound to stacked β-sheet structures. Shown are representative data of ThT fluorescence due to Aβ aggregation in solution (orange circle) and collagen hydrogel (purple star).

In solution samples, the duration of the aggregation lag phase varied with Aβ concentration: greater Aβ concentrations correlated with shorter lag phases of fibril aggregation in solution. The lag phase lasted 7.5 hrs for 10 μM Aβ, 4 hrs for 25 μM Aβ, and only 1 hr for 50 μM Aβ (Figure 3.6A). This effect was also noted for hydrogels, but on a much faster timescale: the lag phase was 1 hr for 10 μM Aβ, and nonexistent for 25 μM and 50 μM Aβ (Figure 3.6B). The rate of fibril aggregation was also influenced by the collagen concentration of the hydrogel: at collagen concentrations of 0.5, 1, 1.5 and 2 mg/ml, the lag phases were observed to be 13.5 hrs, 9.5 hrs, 9 hrs, and 6.5 hrs, respectively (Figure 3.6C).

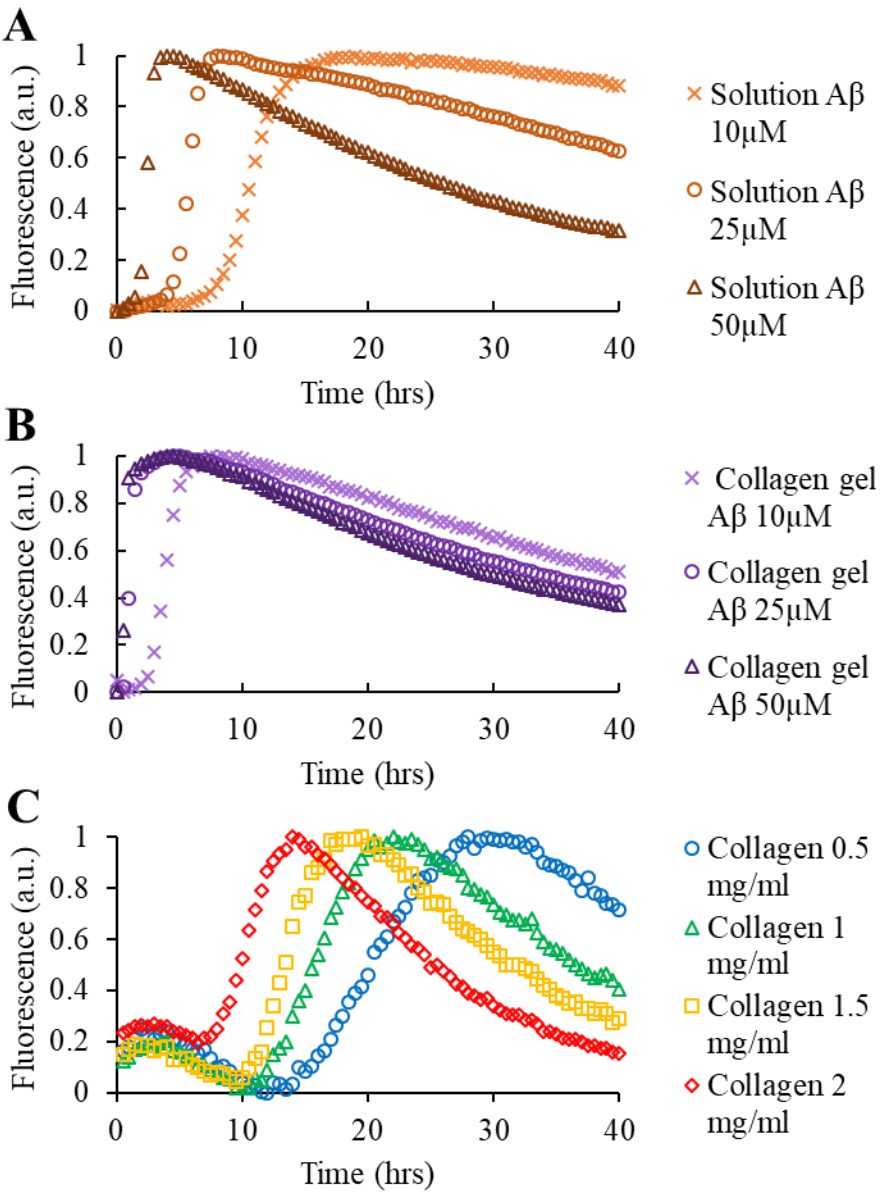

Figure 3.6 Aβ and collagen concentration impact ThT aggregation kinetics. ThT aggregation kinetics comparing Aβ concentrations (10 μM, light x; 25 μM, medium circle; 50 μM, dark triangle) in solution (A, orange) and collagen hydrogel (B, purple). In C, Aβ aggregation kinetics is compared in hydrogels with collagen concentrations of 0.5 mg/ml (blue circle), 1 mg/ml (green triangle), 1.5 mg/ml (yellow square), and 2 mg/ml (red diamond).

Discussion

For almost three decades, researchers have recognized a link between Aβ and AD and pursued drug candidates capable of preventing Aβ aggregation as new therapeutic strategies for AD [229-231]. These interactions were measured in cell culture experiments but were associated with little or no efficacy in pre-clinical testing and clinical trials [20, 191, 232-235].

There is a growing appreciation that cells grown *in vitro*, on rigid polystyrene tissue culture surfaces, behave very differently than cells *in vivo*, and that the stiffness of the surface upon which cells are grown can have profound epigenetic effects on cells that influence their phenotype [236-237]. In addition, many investigators have observed that morphologies of neuronal cells are strikingly more similar to those expressed *in vivo* in 3D vs. 2D culture [24-26, 238]. Thus, the use of 3D cell culture models for AD drug development may lead to a more positive correlation between successes *in vitro* and successes in clinical outcomes.

The preponderance of literature reports indicates that Aβ is toxic to cells in culture only when aggregated and that it is the oligomeric or intermediate-sized aggregation species that are the most toxic species, with large fibril aggregates being less toxic [218, 221]. These findings were reported for cells in traditional culture on flat rigid substrates such as polystyrene or glass. To my knowledge, no one has explored Aβ aggregation kinetics and cellular toxicity in a 3D cell culture model.

In the work presented here, my 2D cell culture of PC12 cells demonstrated the expected cytotoxic nature of Aβ aggregates. However, when PC12 cells and Aβ were encapsulated within 3D collagen hydrogels, the cytotoxic effects were attenuated. I supposed that this effect could be due to one of two effects, either (1) the 3D environment altered the phenotype of the PC12 cells, making them less susceptible to Aβ, or (2) the 3D environment altered the aggregation of Aβ. Given that PC12 cells and other neuron-like cells take on a phenotype more closely associated with an *in vivo* neuron in 3D [24-25, 239], I assumed that my first hypothesis was less probable. Therefore, in this work, I set out to investigate how the 3D collagen hydrogel environment affects Aβ structure and aggregation.

I used a combination of biophysical methods to investigate Aβ structure and aggregation both in solution and in the 3D collagen hydrogel. TEM micrographs of pretreated Aβ that underwent aggregation in solution confirm that the structures seen during my experiments are typical of those seen by others [240-241]. The pretreatment process removed any observable fibril or protofibril structures (Figure 3.2A). FCS and ThT measurements at these early time points (<24 hrs) suggest that only small, rapidly diffusing species remained after Aβ pretreatment; the samples were devoid of any extended β-sheet structures (Figures 3.3A, 3.4A, and 3.5, respectively). These results are consistent with literature reports for Aβ pretreatment via this method [220, 227]. Shortly after the dissolution of Aβ, the Aβ in solution appeared to form dimer or similar diffusing species (Figure 3.4A), and other somewhat larger aggregated species with diffusivity values on the order of 20 $\mu m^2/s$ (Figure 3.3A). The observance of monomers and dimers in equilibrium at early

stages of aggregation of Aβ in solution has been seen via other methods including chromatography [242-243] and hydrogen exchange mass spectrometry and others [244-245]. The observance of larger aggregated species in Aβ solutions that are non-fibril (i.e., they do not bind ThT; Figure 3.5), such as the more slowly diffusing species seen in FCS (Figure 3.3A) and TEM micrographs (Figure 3.2B), is consistent with the formation of the toxic oligomer species. While there is considerable debate concerning the actual size and structure of the most toxic species of aggregated Aβ, most consider that this species is smaller than a fibril [246], and by some accounts, the diffusivity of the toxic Aβ species is on the order of 20 $\mu m^2/s$ [12, 247]. Aβ aggregated for 72 hours shows typical fibril structures via TEM (Figure 3.1C), that bind ThT (Figure 3.4A), as would be expected for large extended β-sheet structures [9]. Given the typical aggregation pathway, I observed of Aβ in solution – one that included detectable oligomers that are suggested to be the most toxic species – the viability results observed in 2D cell culture (Figure 3.1A and 3.1C) were expected.

The same careful biophysical examination of Aβ aggregation in 3D collagen hydrogels demonstrates that aggregation does not proceed through the same pathway as in solutions. Even at early times during aggregation, no slowly diffusing species (diffusivity ~20 $\mu m^2/s$) were observed (Figures 3.3B, 3.4B). At these early times during aggregation, only a small unaggregated species and a very large/slow diffusing species were observed; the larger species diffused 10x to 100x more slowly than the oligomer observed in solution (Figures 3.3, 3.4). Given the ThT fluorescence seen even at these early times (Figure 3.5), this larger species may be a fibril form of Aβ. I hypothesize that I did not observe any notable Aβ toxicity in 3D culture because Aβ

aggregation proceeded through a pathway that did not include the formation of any detectable oligomeric species that are typically associated with Aβ toxicity.

While I am not aware of any other studies of Aβ aggregation in a 3D environment, the effect of crowding and confinement on protein folding and aggregation has been previously studied [32, 34]. Biomaterial scaffolds are composed of self-associating or crosslinked structures that exert an excluded volume effect on soluble molecules that are entrapped within. The excluded volume effect increases the local concentration of soluble molecules, increasing the chance of protein-protein interactions. The reduced volume also confines the available space a protein may use to fold, promoting a more compact, low entropy conformation. Uncrosslinked crowding molecules such as PEG, Ficoll, and bovine serum albumin stabilize protein folding into functional states or accelerate aggregation in aggregation-prone proteins (e.g., lysozyme, α-synuclein, and β2-microglobulin) [34, 83, 85]. Confinement has a greater stabilization effect than crowding but is seldom used to study the biophysics of proteins [105, 107, 248]. I suggest that in my studies, the confinement provided by the 3D collagen hydrogel resulted in increased Aβ-Aβ interactions, thus leading to the observed faster aggregation kinetics and the lack of slower diffusing species. If this were the case, then I would expect to see that higher concentrations of Aβ shortened the lag time to the onset of rapid aggregation due to the greater probability of nucleation of aggregation. This is indeed what I observed (Figure 3.6A and B). At every concentration tested, the lag phase until the onset of rapid aggregation was significantly shorter in 3D environments and shorter at higher Aβ concentrations. The acceleration of aggregation of Aβ with increasing

concentrations of collagen in the 3D hydrogels (Figure 3.6C) is consistent with the hypothesis as well; higher collagen concentrations would lead to smaller void spaces in the 3D collagen hydrogel, thus greater confinement, increased Aβ-Aβ interactions, and acceleration of Aβ aggregation.

When Aβ aggregation is nucleated in a confined environment, the β-sheet structures that form are more stable vs. aggregation as free molecules in solution, resulting in faster filament growth. Such stabilization of β-sheet structured Aβ aggregates that occurs in collagen hydrogels should result in a shift in the chemical equilibrium of aggregate species. In solution, the equilibrium composition of Aβ species is expected to be a distribution of unstructured monomer – dimer – multimer species. In confined collagen hydrogels, however, I hypothesize (and my data support) that the equilibrium is shifted to stable β-sheet aggregates and away from the relatively unstable/unstructured presumed toxic oligomeric Aβ species.

I propose that the attenuation of Aβ toxicity observed in the 3D environment is due to the shift in aggregation kinetics of Aβ away from the smaller toxic oligomer. However, other explanations are also plausible. Aggregated Aβ species may have hindered diffusion in the 3D collagen hydrogel. The FCS data suggest that at least at early times the Aβ species do diffuse within the hydrogel. In addition, the mesh size of the 3D collagen hydrogels used in this study was ~10 μm, one to two orders of magnitude larger than reports of sizes of Aβ toxic oligomers [249-250]. Therefore, I do not conclude that hindered diffusion of Aβ within the hydrogel contributed significantly to the attenuation in Aβ toxicity observed in 3D compared to 2D environments. It is also possible that the 3D environment resulted in some

unexpected phenotypic change in the PC12 cells that I cannot rule out in the studies performed in this work.

The shift in the equilibrium of Aβ species away from smaller potentially toxic species to larger extended β-sheet species in confined environments observed in my studies may suggest similar phenomena *in vivo* tissues. At the very least, my studies suggest that Aβ aggregation kinetics are fundamentally different in 3D structures as compared to in the solution phase of 2D culture, making a direct translation of results from a 2D culture model to a more *in vivo*-like 3D culture model difficult. However, this relatively simple collagen hydrogel cannot recapitulate the complexity of the *in vivo* environment. I can only speculate that the high percentage of failed Aβ targeting drugs in clinical trials may be due to the drug discovery models missing essential properties such as confinement and dimensionality. Knowing the biophysical impact of confinement stabilizing toxic Aβ aggregate species, advanced 3D *in vitro* models may be developed to investigate AD pathology and be implemented in AD drug development.

Chapter 4 : Impact of four common hydrogels on Amyloid-β (Aβ) aggregation and cytotoxicity: Implications for 3D models of Alzheimer's disease

This chapter has been submitted for publication

Introduction

Alzheimer's disease (AD) is the most common form of dementia [251], and is associated with the accumulation of amyloid-β (Aβ), a protein whose aggregation is associated with neurotoxicity [188]. There is still debate over the exact size and structure of the most toxic Aβ species, but it is widely held that small oligomers that lack β-sheet structure are more toxic than assembled β-sheet fibrils [10-11, 218-220]. Since the first genetic connection between Aβ and early-onset AD, investigators have targeted Aβ as a potential therapeutic strategy [189, 230-231]. Many anti-Aβ antibody drugs (e.g., aducanumab, solanezumab, crenezumab, gantenerumab) have had promising preclinical results; however, all have failed to show a significant clinical benefit [190-191, 252].

We have previously demonstrated that Aβ cytotoxicity was attenuated in 3D type I collagen hydrogels as compared to in 2D culture in which significant cell death occurred [253]. I suggested that in collagen hydrogels, a) the structural equilibrium of Aβ is shifted to favor larger β-sheet aggregates in contrast to in solution where the smaller oligomeric Aβ species persisted and b) that this shift in distribution of Aβ structures may have led to the stabilization of larger, less toxic fibril species compared to the species observed in solution. Confinement excludes the locally-available solvent, which promotes a more compact peptide/protein structure. Confinement also increases local protein concentration, promoting protein-protein interactions. This finding challenges the choice of 2D culture for investigations of Aβ cytotoxicity. Yet, only a few 3D gel-based models of AD have been published to

date, all using the gel matrix Matrigel® (Corning) [110, 209-210]. Matrigel® is composed of basement membrane ECM molecules (60% laminin, 30% collagen IV, and 8% entactin) and is also commonly used to investigate stem cell differentiation [201-202, 254-256].

A second possible explanation of my previous results is that 3D culture in a collagen hydrogel results in changes in cell signaling, phenotype, or potentially the expression or function of receptors available for Aβ interaction, resulting in attenuated toxicity. In support of this explanation, it is known that epigenetic changes occur in 3D culture that influences cellular phenotype [236-237]. Further, in comparison to 2D culture, cell morphologies of neuronal cells grown in 3D culture are strikingly similar to those expressed *in vivo* [24-26, 203, 238]. Finally, there have been numerous reports of cell surface receptors that bind Aβ, with the numbers of candidate receptors totaling 30 or more [257]. Thus, it is possible that the attenuation of Aβ cytotoxicity observed in 3D collagen may be unrelated to Aβ structural changes, but instead, be related to cellular responses that are altered due to 3D culture or the presence of collagen.

In this work, I investigated the extent to which of this Aβ confinement effect also occurs in other 3D hydrogels that vary in biomaterial physiochemical properties (e.g., mesh size, chemical composition, and biological activity). In this work, I studied Aβ structure, aggregation, and toxicity in hydrogels primarily composed of type I collagen, low melting temperature agarose, hyaluronic acid (HA), or polyethylene glycol (PEG) (Figure 4.1). In choosing these gel types, I was less concerned with specific biological relevance to brain tissue, rather focusing on gels

that vary greatly in mesh size, the potential to alter cell phenotype, and the potential to interact with one or more of the many suspected Aβ cell surface receptors [257]. I excluded laminin and laminin-containing materials (such as Matrigel®) from these studies because of laminin's high affinity for Aβ and its potent inhibition of fibril formation [258] Indeed, in my early experiments, I noted that Aβ did not aggregate in gels containing laminin (data not shown).

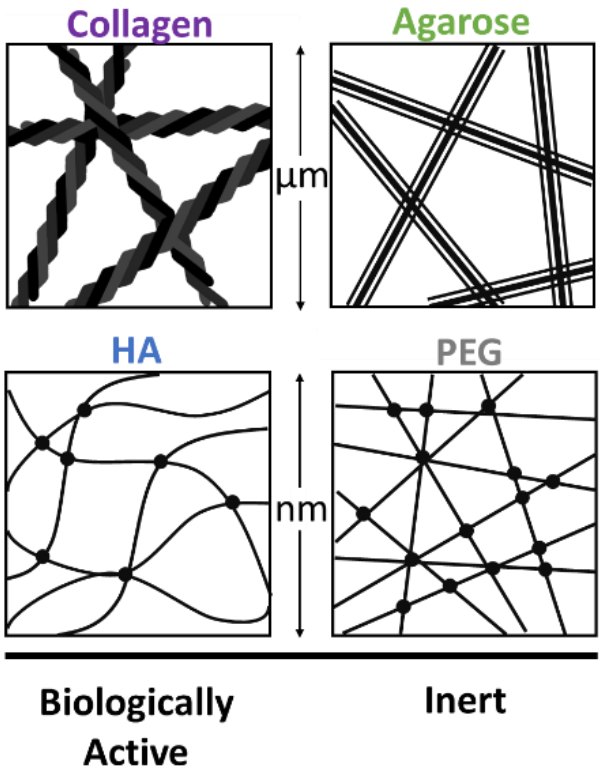

Figure 4.1 Properties of four 3D hydrogels.

Four biomaterials were used as hydrogels to encapsulate PC12 cells and Aβ based on their biophysical properties. Collagen is biologically active with a mesh size ~ 10 μm. Agarose is an inert polysaccharide with a mesh size ~ 800 nm. HA is a biologically active glycosaminoglycan modified with maleimide groups and

crosslinked with PEG dithiol with a mesh size ~ 200 nm. PEG is an inert polymer crosslinking a 4-arm PEG maleimide with a PEG dithiol with a mesh size ~ 10 nm.

Collagen is the most abundant extracellular matrix (ECM) molecule making up 30% of total mammalian protein mass [259-260]. Type I collagen is the primary protein in the interstitial ECM and is commonly applied to *in vitro* models of cancer invasion [27, 261]. Many cell types have type I collagen binding motifs that are important for adhesion, motility, and signaling [25, 200, 262]. The mesh size of type I collagen hydrogels is on the order of ~10 μm [250].

Agarose is an inert polysaccharide that forms hydrogels with mesh size and stiffness that are controlled by agarose concentration and setting temperature [263]. Agarose hydrogel mesh size can range from 200 nm to 800 nm [131, 263]. Agarose hydrogels have been utilized to study the diffusion of molecules through porous media [130-131] and investigate the effect of material stiffness on cell morphology [264]. In particular, pre-aggregated Aβ40 has been applied to 3D agarose culture; however, the aggregate structure was not investigated [247].

HA is a biologically-active glycosaminoglycan found in the ECM of soft connective tissues, especially the central nervous system (CNS) which is devoid of most proteinaceous ECM molecules [265-266]. Considering HA is a natural ECM molecule, it is inherently biocompatible and therefore is commonly selected for applications in regenerative medicine and drug delivery [111, 113, 152]. HA plays an important role in development and is therefore particularly relevant to *in vitro* cultures of stem cells and cancer cells [119, 267-271]. To form stable hydrogels, HA

can be modified with reactive functional groups and crosslinked to yield gels with a wide variety of properties [272-274]. HA mesh size is dependent on the molecular weight of the HA, the degree of modification of functional groups, and the crosslinking chemistry, and is typically between 100 – 600 nm [112, 119, 121].

PEG is an inert synthetic polymer that can be modified with reactive functional groups and crosslinked into a hydrogel scaffold [23, 275]. The particular crosslink chemistry can be selected to adjust gelation time, and the PEG molecular weight, and concentration influence gel stiffness and mesh size, which is typically 10 – 20 nm [276-277].

The work described herein examines Aβ aggregation and cytotoxicity in four hydrogels that are commonly selected for applications that involve encapsulated cells (Figure 4.1). I was particularly interested in collagen, agarose, HA and PEG gels because they have mesh sizes varying from ~10's of nm to ~10's of μm. These mesh sizes were hypothesized to impart confined microenvironments on Aβ that are relevant to the sizes of Aβ structures, from monomers/oligomers to fibrils. I was also interested in these hydrogels given their range of physiochemical properties and potential to interact with cells.

Materials and Methods

Beta-Amyloid Preparation

Human beta-amyloid (1-42) (Aβ) and scrambled Aβ (1-42) (Scr Aβ) (*AIAEGDSHVLKEGAYMEIFDVQGHVFGGKIFRVVDLGSHNVA*) was purchased from AnaSpec (Fremont, CA) and Genscript (Piscataway, NJ). HiLyte 488-labeled Aβ (1-42) (HiLyte Aβ) and FAM-labeled scrambled Aβ (1-42) (FAM Scr Aβ) were purchased from AnaSpec (Fremont, CA). All other unspecified reagents were purchased from Sigma Aldrich (St. Louis, MO) or ThermoFisher Scientific (Waltham, MA).

To break any existing β-sheet structures and monomerize the protein, lyophilized Aβ was pretreated with hexafluoro-2-propanol at a concentration of 1 mg/ml for 40 mins until Aβ was fully dissolved. Aβ aliquots were transferred into glass scintillation vials, and hexafluoro-2-propanol was evaporated under vacuum overnight. Aliquots of dried peptide film were stored at -20^{o}C. For an experiment, an Aβ aliquot was dissolved in freshly-made and filtered 60 mM NaOH and allowed to dissolve for 2 mins at room temperature. Tissue culture grade water was then added, and the vial was sonicated for 5 mins. Next, the Aβ solution was filtered with a 0.2-μm pore, 4-mm diameter syringe filter. Sterile phosphate buffered saline (PBS) was then added to the Aβ monomer solution yielding a final concentration of 222 μM with the NaOH:water:PBS ratio of 2:7:1. The Aβ solution was used immediately after preparation. HiLyte Aβ and FAM Scr Aβ were prepared in the same NaOH:water:PBS ratio solution to a stock Aβ concentration of 10 μM.

Hydrogel Preparation

Rat tail type I collagen hydrogels were prepared to final concentrations of 1 mg/ml. Cold 5x Dulbecco's Modified Eagle's Medium (DMEM) without phenol red, 7.5% sodium bicarbonate, sterile deionized water, and collagen were combined with PC12 cells to generate 3D substrates in black-walled clear-bottom well plates.

SeqPlaque Agarose with a concentration of 1% (w/v) was prepared in deionized water and sterilized. Agarose was heated to 68°C then cooled at room temperature for 5 minutes before mixing 1:1 with concentrated culture medium; yielding a solution of 1x DMEM without phenol red, 1% B27, and 0.5% agarose. The hydrogel solution was dispensed into black-walled clear-bottom well plates and placed in a culture incubator for 20 mins to allow for gelation.

HA and PEG hydrogels were each crosslinked by a maleimide-thiol Michael addition click reaction. Hyaluronic acid (HA, 242 kDa) was functionalized with maleimide (HA-Mal) following a published protocol [121]. Briefly, HA was dissolved in 0.1 M 2-(N-morpholino)ethanesulfonic acid (MES) buffer at a concentration of 5.15 mM. 1-Ethyl-3-(3-dimethylaminopropyl) carbodiimide (EDC, 15 mM) and N-hydroxysuccinimide (NHS, 15 mM) were added, and the solution was mixed for 30 mins. Next, N-(2-aminoethyl) maleimide trifluoroacetate salt (AEM, 10 mM) was added and mixed for 4 hrs covered with plastic wrap. The mixture was dialyzed against 50 mM NaCl in deionized water for 3 days, then against deionized water for 3 days. The dialyzed solution was then sterile-filtered and aliquoted

aseptically into sterile 15-ml tubes, lyophilized and stored at -20°C. The degree of substitution, the number of maleimide groups per HA chain, was determined as per [121] by ^{1}H NMR to be ~40.

For HA hydrogels, HA-Mal was prepared at 1% (w/v) and mixed equal volume with PEG dithiol (10 kDa) at a molar ratio of 1:1.2 maleimide to thiol. For PEG hydrogels, 4-arm PEG maleimide (PEG-Mal, 20 kDa) was prepared at 5% (w/v) and mixed equal volume with PEG dithiol (10 kDa) at a molar ratio of 1:1 maleimide to thiol. All HA and PEG solutions were dissolved in Neurobasal medium supplemented with 1% B27. PEG solutions were filter-sterilized. In black-walled clear-bottom well plates, maleimide solutions were pipetted into the well first, then the thiol solution containing experimental additives (cells, Aβ, ThT) was pipetted into the maleimide droplet to mix. Both HA and PEG gels crosslinked within ~5 sec.

Thioflavin T

A black-walled clear-bottom 384 well plate (Costar) was sterilized under UV light for 15 minutes in a laminar flow hood. UltraPure grade Thioflavin T (ThT) (AnaSpec, Fremont, CA) was dissolved in deionized water at a concentration of 1 mM then filter-sterilized. Wells for 2D and 3D samples were prepared as above but contained 20 μM ThT. The wells were sealed with black TopSeal-A membranes to prevent evaporation. The ThT experiment was analyzed on a Spectra Max M5 (Molecular Devices, San Jose, CA) spectrophotometer set to ex. 450 nm, em. 480 nm, at 37°C, taking measurements every 30 mins for 72 hrs and reading from the bottom

of the plate. Replicates were averaged, Aβ data was corrected with ThT control data, and corrected curves were normalized. As in standard practice in Aβ aggregation studies [7, 278] due to the stochastic nature of aggregation, curves representative of at least 10-20 experiments are presented here.

Fluorescence Correlation Spectroscopy

Theory

Fluorescence Correlation Spectroscopy (FCS) measures the fluctuations of fluorescence in a small, optically-defined confocal volume (~10^{-15} liter). These fluctuations are typically attributed to the fluorescent particles moving in and out of the volume with a statistical average residence time, τ_D. The residence time is proportional to the hydrodynamic radius (R_H) of the molecule. The fluctuations of detected photons inform the autocorrelation, $G(\tau)$, function defined as

$$G(\tau) = \frac{\langle \delta I(t+\tau)\delta I(t)\rangle}{\langle I(t)\rangle^2}$$

Where $\delta I(t) = I(t) - \langle I(t)\rangle$ is the fluorescence fluctuation determined from the measured fluorescence intensity, (t) , at time t, and the average intensity, $\langle I(t)\rangle$, over the period of measurement. The excitation laser, which is focused, is assumed to have a 3D Gaussian profile, with a characteristic radial dimension (w_0) and a characteristic axial dimension (z_0). For a solution of n noninteracting, freely diffusing fluorescent species $G(\tau)$ is given by:

$$G(\tau) = \sum_{i=1}^{n} b_i \left(\frac{1}{1 + \frac{\tau}{\tau_{D_i}}} \right) \left[\frac{1}{1 + \left(\frac{w_0}{z_0}\right)^2 \frac{\tau}{\tau_{D_i}}} \right]^{1/2}$$

$$\tau_{D_i} = \frac{{w_0}^2}{4D_i}$$

Here the D_i values are the n different values of diffusion constants and b_i are the relative fractions in brightness of these species. In practice, the radial and axial dimensions were determined using Alexa 488 dye in water where the diffusion coefficient (430 $\mu m^2/s$) is known and was used to estimate the excitation volume for a 3D Gaussian beam [225].

Methods

Experimental medium was used in preparing solution samples and contained 20 μM Aβ and 250 nM HiLyte Aβ. Hydrogels were prepared as described with 20 μM Aβ and 250 nM HiLyte Aβ then pipetted into 0.8-mm deep hybridization chambers (PerkinElmer, Waltham, MA) on a borosilicate cover glass. Control samples were tested with 20 μM Scr Aβ and 250 nM FAM Scr Aβ.

The FCS measurements were performed using an Alba-FFS microscope-based system from ISS Inc. (Champagne, IL). The system is composed of: an Olympus IX81 inverted microscope equipped with a 60X/1.35NA oil immersion objective lens, a Prior Pro stage, three different lasers (450 nm, 488 nm, and 532 nm), two

Hamamatsu Photon Multiplier tubes (PMTs) for photodetection, and two sets of computer-controlled scanned mirrors for imaging. In these measurements, only the 488-nm diode laser was used for excitation of the fluorophores Alexa 488 or fluorescently-labeled Aβ, and the emitted fluorescence was collected through confocal detection with a pinhole (< 50 mm) located in the image plane of the excited focused beam inside the sample. The emitted fluorescent beam was optically filtered further with (525/50nm) filter and then sent to a 50/50 beam splitter for detection by two PMTs positioned in a 90-degree angle configuration. The photocounts of both PMTs were continuously acquired and then computationally cross-correlated in order to eliminate the afterpulsing effect of a single PMT, which is typically noticeable at short delay times (< 10 ms).

Using Vista Vision software, two runs were carried out back to back collecting for 3 minutes each to generate the correlation function $G(\tau)$ for each sample at a time point. The two correlation functions were averaged, and the Scr Aβ correlation function was fit using the one-component model to determine the diffusivity of the monomer. Further, the measured time-correlation functions for Aβ were fit using the 2-component model where the size of species 1 was held constant at monomer diffusivity in order to derive the average aggregate diffusivity population of the second species. Additional refinement for fitting the correlation functions were also performed with the Maximum Entropy Method FCS (MEMFCS) thanks to a code gifted by Dr. S. Maiti (Tata Institute of Fundamental Research), allowing us to obtain the heterogeneous distribution of aggregate diffusivities at each time point [176].

Small molecules have a short delay time because they diffuse quickly through the volume, whereas large molecules have a long delay time because of their relatively slow diffusion through the volume. The 2-component model is intended to model two distinct molecular species in solution. For my samples, I held the monomer diffusivity constant as species 1 where the average diffusivity of aggregated species was identified by solving for species 2.

Fluorophore labeling of Aβ monomers inhibits aggregation due to the bulky groups sterically preventing proper monomer to monomer stacking [159]. Therefore, I used a ratio of 1:80 HiLyte 488-labeled Aβ to unlabeled Aβ, and FAM-labeled Scr Aβ to unlabeled Scr Aβ, to allow unhindered β-sheet stacking. Nanomolar fluorophore concentrations are also preferable in FCS in order for the detectors to monitor few individual fluorescent molecules in the confocal volume, enhancing hence the signal-to-noise of the fluctuations.

Cell Culture

PC12 cells (ATCC, Manassas, VA) (CRL-1721TM) were cultured in collagen-coated flasks. Growth medium consisted of DMEM/F12 with L-glutamine and without phenol red, supplemented with 10% inactivated horse serum, 5% fetal bovine serum, and 20 μg/ml gentamicin. The experimental medium consisted of Neurobasal medium without phenol red, supplemented with 1% B27 and 20 μg/ml gentamicin. Phenol red and serum were avoided in the experiments because they are inhibitors of Aβ aggregation [223-224].

Live/Dead Assay

PC12 cells were collected by trypsin treatment, and viability was determined by trypan blue staining. To remove serum, cells were resuspended in experimental medium, pelleted then resuspended again in experimental media. In a black-walled clear-bottom tissue culture treated 96-well plate, wells for 2D culture were collagen-coated, and then PC12 cells were seeded at 15×10^3 cell/cm^2. For the 3D hydrogels, PC12 cells were mixed in collagen and agarose gel solution at a concentration of 500 cell/μl; the solution was then pipetted (30 μl) into the well plate and allowed to solidify. For HA and PEG hydrogels, PC12 cells were mixed in PEG dithiol solutions at a concentration of 1000 cell/μl. HA-Mal and PEG-Mal solutions were pipetted (15 μl) into the well first; then the PEG dithiol solution (containing cells) was pipetted (15 μl) into the maleimide solution to mix. The final HA and PEG hydrogels had a PC12 cell concentration of 500 cell/μl. All wells were incubated in 200 μl warmed medium.

To determine cell viability, the Live/Dead mammalian cell kit (Invitrogen, Carlsbad, CA) was applied at a concentration of 4 μM Calcein AM (green-fluorescing live cell reporter) and 9 μM Ethidium homodimer-1 (EthD) (red-fluorescing dead cell reporter) and incubated at 37°C for 30 minutes. Images were captured on an IX81 Olympus inverted fluorescent microscope. A minimum of 100 cells were counted per well (two images per well), and three wells per condition were tested. The data is presented as percent viability, averaged between the three replicate experiments. An

ANOVA Tukey pairwise test determined significant deviation from the population mean with a p-value less than 0.05 with 95% confidence.

Results

In my earlier work, I observed that Aβ aggregation kinetics varied between the contexts of a solution and a 3D collagen hydrogel and that the variations in Aβ aggregation were associated with differences in cytotoxicity between those two contexts. I suggested that the altered Aβ aggregation in the collagen gel was due to confinement within the gel structure, which imparts a shift in the equilibrium Aβ species quickly to larger aggregates vs. the prolonged presence of oligomers in the solution of a 2D culture. Herein, I further explore this Aβ confinement effect in four hydrogel types that vary in mesh size with size scales relevant to Aβ structures, from monomers/oligomers to fibrils. Because cell-collagen-Aβ interactions may be related to the observed attenuated cytotoxicity, I was also interested in these hydrogels given their range of physiochemical properties and potential to interact with cells.

ThT fluorescence as a measure of Aβ aggregation kinetics

To examine the impact of different 3D environments of Aβ aggregation, I used the ThT assay to identify the presence of β-sheet Aβ aggregates in solution compared to in collagen, agarose, HA, and PEG hydrogels.

Representative curves of ThT fluorescence vs. time are shown in Figure 4.2 for Aβ aggregation in solution and hydrogels. In solution, fibrillar Aβ aggregation (signified by ThT fluorescence) had a lag phase during the first ~20 hrs, followed by rapid aggregation. In all hydrogels, however, fibrillar aggregation did not exhibit a lag phase, and instead, fluorescence steadily increased from the initiation of the experiment (Figure 4.2). Depending upon the supplier and the particular lot of Aβ tested, lag time as well as the maximum fluorescence intensity varied, but all shared the same qualitative features of fibril Aβ aggregation in solution vs. the hydrogels: fibril aggregation was accelerated in the hydrogels compared to in solution. Fibrillar Aβ aggregation appeared to proceed most rapidly in the gel with the smallest mesh size -- the PEG hydrogel showed the fastest initial onset of ThT fluorescence.

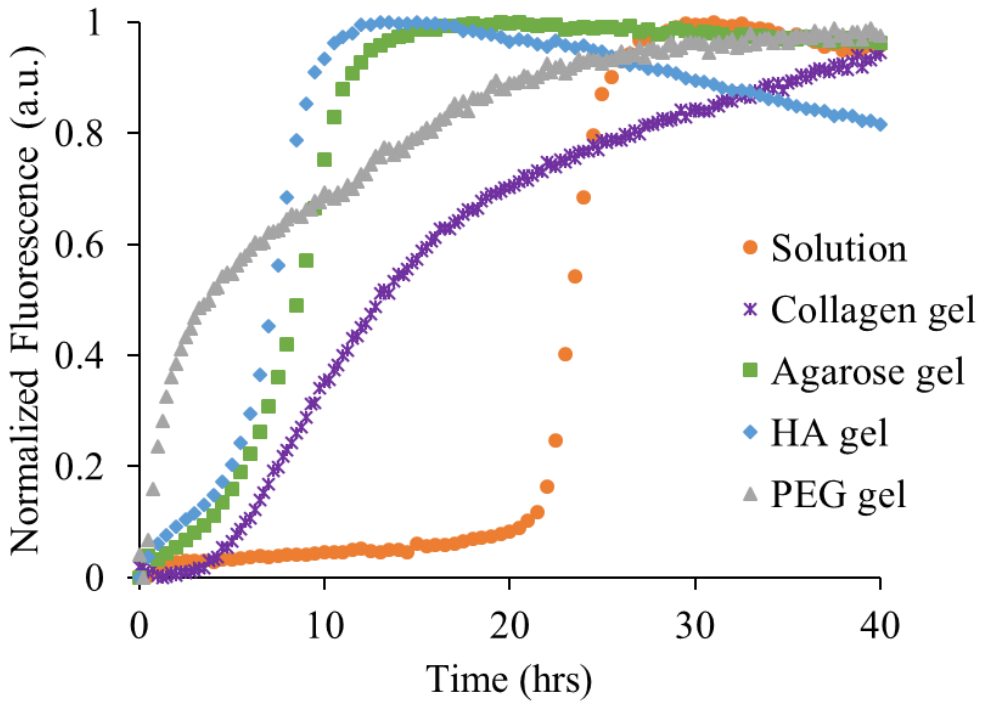

Figure 4.2 ThT Aβ aggregation kinetics in solution and four hydrogels.

ThT binding to stacked β-sheet amyloids triggers fluorescence and therefore tracks kinetics of β-sheet filament aggregation in solution (orange circle), collagen hydrogel (purple star), agarose hydrogel (green square), HA hydrogel (blue diamond), and PEG hydrogel (gray triangle).

Aβ aggregate diffusivities by FCS

Whereas ThT experiments provide insight into Aβ aggregate structure and kinetics, this approach is limited in that it cannot indicate aggregate size. Therefore, I utilized FCS to infer relative Aβ aggregate size from the diffusivity of fluorescently-labeled Aβ species. Diffusivity scales inversely to the radius of a spherical particle. Therefore small diffusivity values correspond to large particles. While Aβ aggregates are not spherical, this general idea that diffusivity scales inversely with particle size still applies.

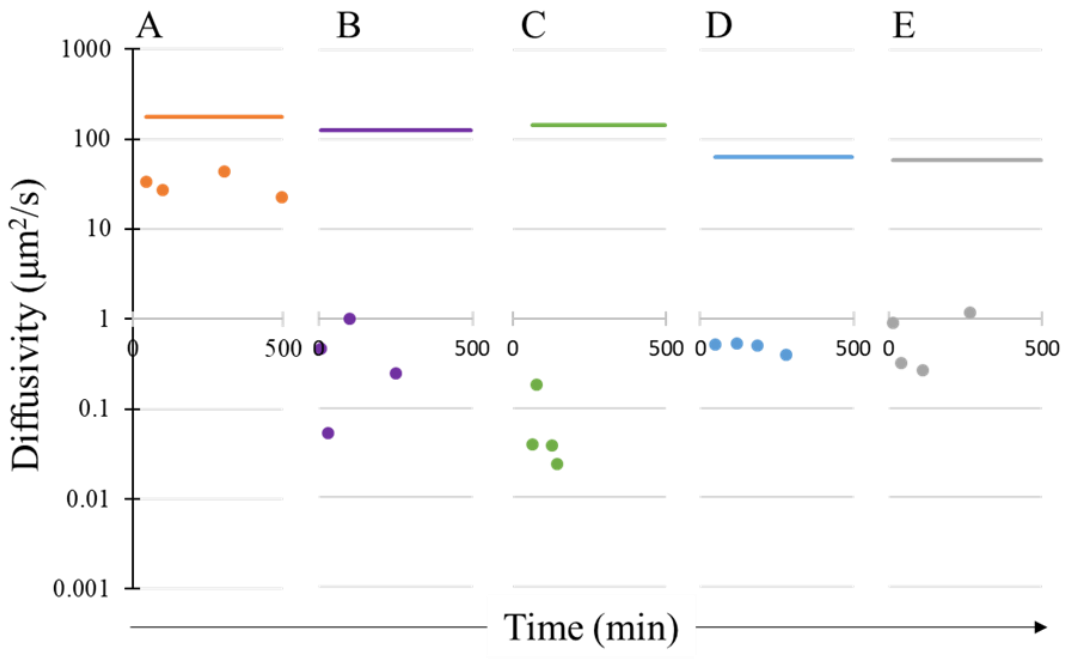

Figure 4.3 FCS G(τ) fit using a triplet 2-component model.

G(τ) of 20 μM Aβ with 250 nM HiLyte Aβ where Species 1 was held constant at the calculated Scr Aβ diffusivity (in each condition) assumed to be monomer (solid line). Species 2 was solved for and represents the average aggregate species diffusivity population in solution (A, orange), collagen hydrogel (B, purple), agarose hydrogel (C, green), HA hydrogel (D, blue), and PEG hydrogel (E, gray).

Non-aggregating Scr Aβ was used as a control of monomer diffusivity. The diffusivity of these Scr Aβ monomers in solution was determined to be 175 $\mu m^2/s$, whereas the diffusivity in the hydrogels were 129 $\mu m^2/s$ (collagen), 145 $\mu m^2/s$ (agarose), 65 $\mu m^2/s$ (HA), and 59.5 $\mu m^2/s$ (PEG) (Figure 4.3). As points for comparison, the diffusivity of Aβ monomer is 180 $\mu m^2/s$ in solution and 62.3 $\mu m^2/s$ in brain tissue [153]. In solution, the diffusivity of the average Aβ aggregate population (determined using the 2-component model) is ~6x slower than the monomer with

little variation for up to 6 hrs (Figure 4.3A). In collagen, the diffusivity of the average Aβ aggregate population is ~850x slower than the monomer for up to 4 hrs (Figure 4.3B). In agarose, the diffusivity of the average Aβ aggregate population is ~3,600x slower than the monomer for up to 4 hrs (Figure 4.3C). In the small mesh size hydrogels, HA and PEG, the diffusivity of the average Aβ aggregate population is ~130x slower than the monomer with little variation (one order of magnitude or less) for up to 4 hrs (Figure 4.3D & E).

The correlation functions were also determined using the MEMFCS program. A distribution of multiple diffusivity populations of Aβ aggregates and their relative fractions were modeled. In solution, Aβ diffusivity values have a single broad distribution with a peak diffusivity of 85 $\mu m^2/s$ (Figure 4.4A). The peak diffusivity of Aβ in solution is ~2x slower than the Scr Aβ diffusivity, suggesting an Aβ population predominately composed of dimers. In all hydrogel types, Aβ has a peak diffusivity similar to the diffusivity of Scr monomer. However, in contrast to the solution samples that only have one diffusivity peak, the diffusivity values in all hydrogel types show a small secondary diffusivity peak as early as 25 mins after addition of Aβ to the hydrogel and persists throughout the measurement period (up to 5 hrs) with diffusivity values in the range of 0.1 $\mu m^2/s$ to 9 $\mu m^2/s$, or between 1000x to 15x slower than Scr Aβ (Figures 4.4B-E). The width of the diffusivity peaks appears to be most narrow for Aβ samples measured in the HA and PEG hydrogels.

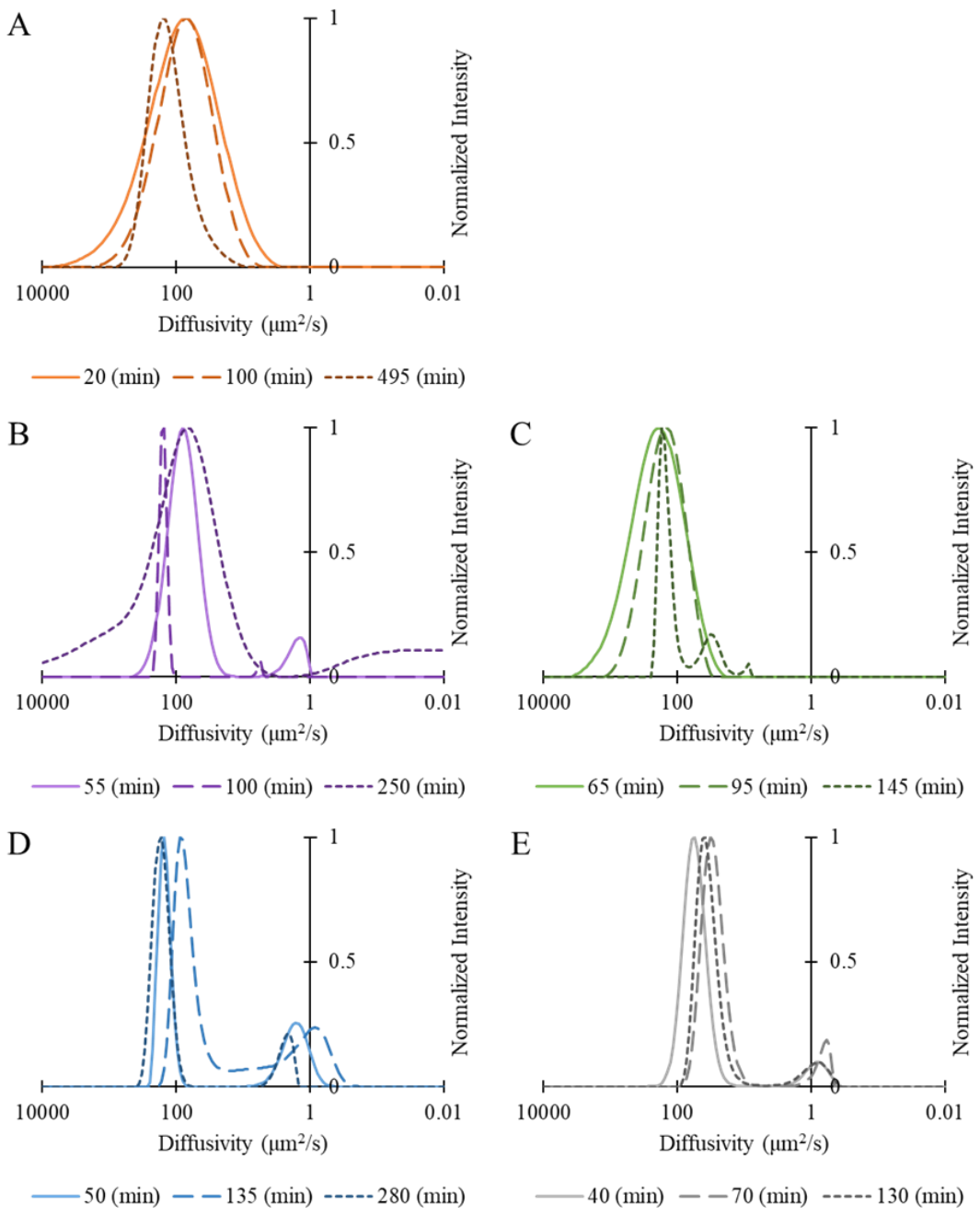

Figure 4.4 Aβ aggregate distribution using the MEMFCS program.

FCS G(τ) fit of 20 μM Aβ with 250 nM HiLyte Aβ using the MEMFCS program gifted by Dr. S. Maiti [228]. In A, solution timepoints were collected at 20 min (solid line, light orange), 100 min (long dash, medium orange) and 495 min (short dash, dark

orange). In B, collagen hydrogel timepoints were collected at 55 min (solid line, light purple), 100 min (long dash, medium purple), and 250 min (short dash, dark purple). In C, agarose hydrogel timepoints were collected at 65 min (solid line, light green), 95 min (long dash, medium green), and 145 min (short dash, dark green). In D, HA hydrogel timepoints were collected at 50 min (solid dash, light blue), 135 min (long dash, medium blue), and 280 min (short dash, dark blue). In E, PEG hydrogel timepoints were collected at 40 min (solid line, light gray), 70 min (long dash, medium gray), and 130 min (short dash, dark gray).

Both analysis methods of the FCS data indicate that Aβ aggregates differently in 3D gels compared to in solution. Based on these data, a rough estimate of aggregate species size in hydrogels is ~25x to 200x larger than the Aβ species detected in solution.

Toxicity of Aβ in 2D and 3D cultures

Biophysical analysis using ThT and FCS depict matching trends for Aβ aggregation in the hydrogels as compared to in solution. However, the variations in aggregation between hydrogel types may favor different size ranges of aggregate species that have varying degrees of toxicity. Therefore, I examined the viability of PC12 cells when treated with Aβ in 2D and 3D collagen, agarose, HA and PEG hydrogels over a 72 hr period (Figure 4.5).

We acknowledge that the percent viability decreases for all samples over time, but it is important to note that the medium was not exchanged in order to better retain the evolving populations of Aβ species that were measured in the ThT and FCS experiments. Over 72 hrs, it is likely that cell waste accumulates, and nutrients are depleted, thus explaining the decrease in cell viability in all conditions.

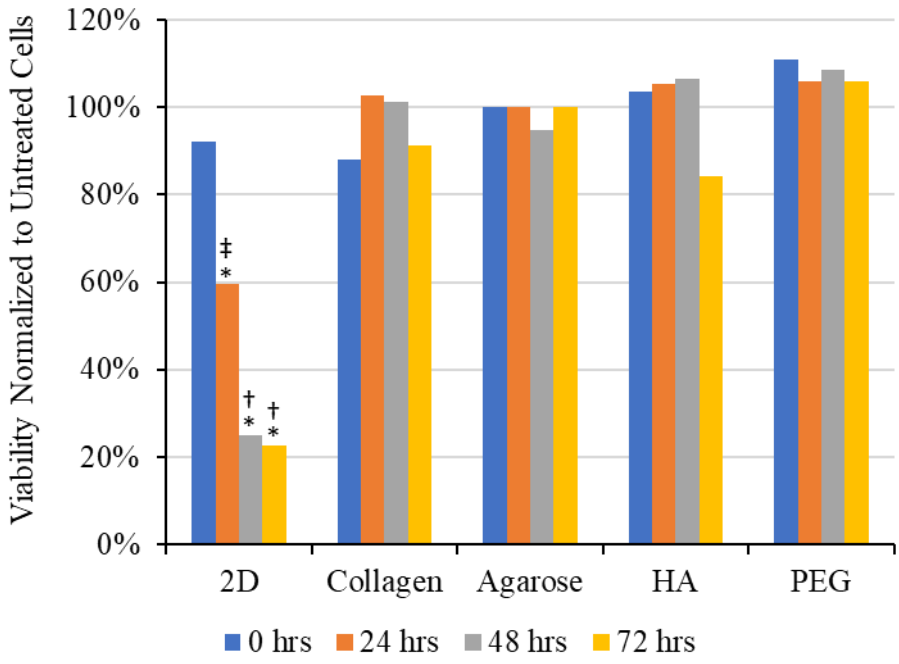

Figure 4.5 Viability of Aβ treated cells normalized by the untreated condition. Viability of PC12 cells treated with 20 μM pretreated Aβ, normalized by respective untreated conditions. Cells were cultured on 2D collagen or encapsulated within 3D collagen hydrogel, 3D agarose hydrogel, 3D HA hydrogel, or 3D PEG hydrogel. Viability was tested using a Live/Dead assay over the 72 hr period. Significant differences were seen in 2D culture in the presence of Aβ compared to no Aβ at 24, 48, and 72 hrs signified by (*). Significant differences were seen between all hydrogels treated with Aβ compared to the respective time points in 2D (48 and 72

hrs) signified by (†). A significant difference was also seen between 3D HA and 2D culture at 24 hrs signified by (‡). Statistics used n = 4. P values at significantly different times in 2D culture: 24 hrs (0.004), 48 hrs (<0.001), and 72 hrs (<0.001); 3D cultures: 48 hrs (<0.001) and 72 hrs (<0.001); and 3D HA: 24 hrs (0.045).

We report the viability data in two ways. In this section of the text, I report the cell viability percentages for each condition. Then to provide an alternative perspective for interpreting the results, in Figure 4.5, I show the same data with Aβ treatment condition normalized by the respective untreated condition (Figure 4.5). The percent of viable cells cultured in 2D with Aβ decreased greatly by 24 hrs (49% viability; p-value 0.004), and then at 48 hrs and 72 hrs, the cell viability was further reduced to 16% (p-value <0.001) and 12% (p-value <0.001), respectively [253]. The type of 3D hydrogel did not affect cell viability, yet differences between the viability of Aβ-treated cells in 3D hydrogels vs. 2D culture at 48 hrs and 72 hrs are significant (p-value <0.001).

Considering the normalized cell viability data, at 24 hrs, cells cultured in 3D HA hydrogels treated with Aβ had higher normalized viability (105%) than in 2D (60%), and this difference is significant (p-value 0.045, Figure 4.5). Representative fluorescence microscopy images of LIVE/DEAD-stained cells at 0 hrs, 24 hrs, 48 hrs, and 72 hrs in 2D and 3D cultures are shown in Figure 4.6. In the presence of Aβ, the extent of cell death (red staining) at 48 hrs and 72 hrs in 2D culture is striking, while no notable increase in cell death is observed in the Aβ-treated 3D cultures (Figure 4.6B - E).

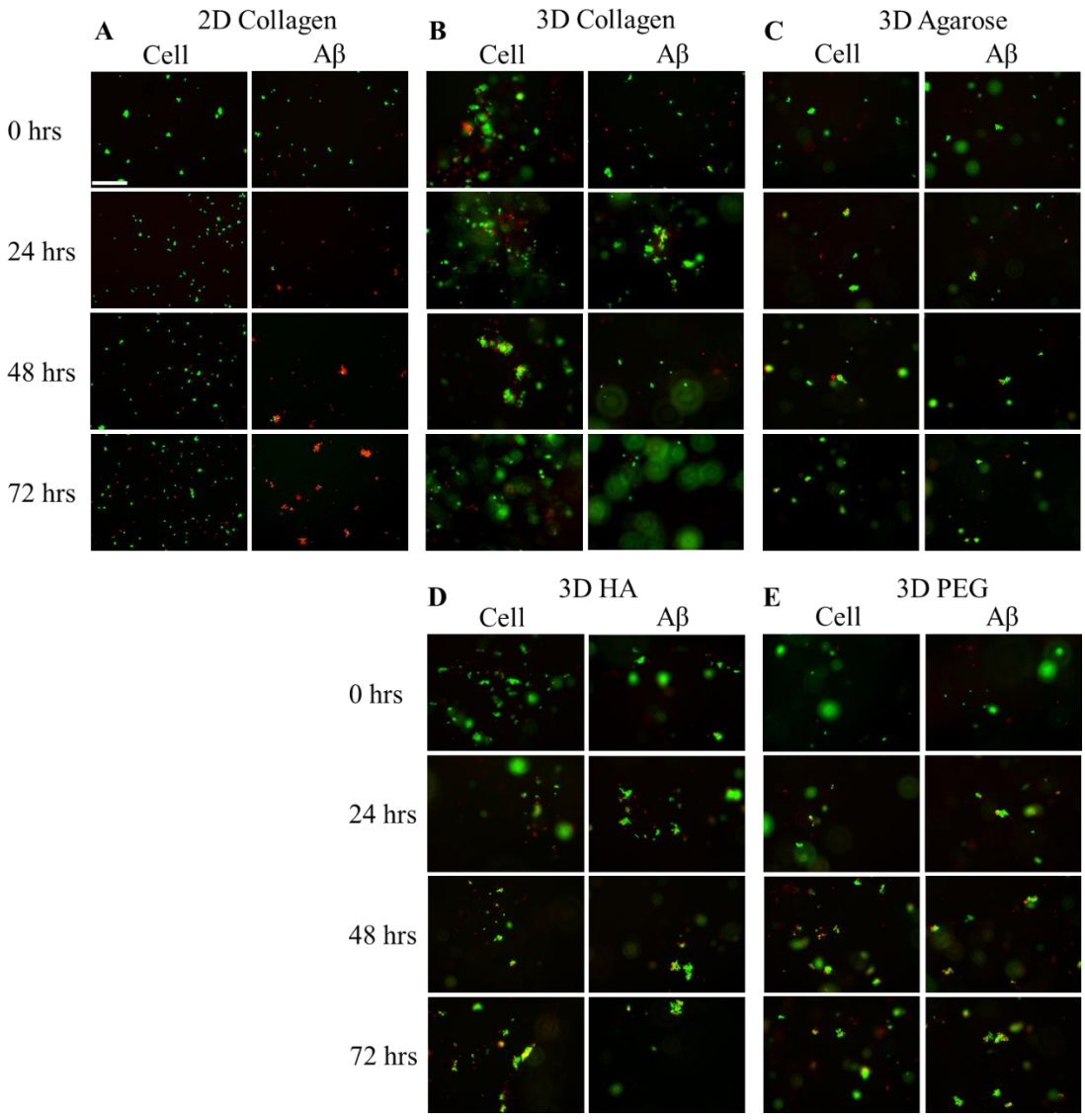

Figure 4.6 Micrographs of PC12 cell viability in 2D and 3D culture.

Cells were cultured on 2D collagen (A), in 3D collagen (B), 3D agarose (C), 3D HA (D) and 3D PEG (E). Control conditions were cells cultured without Aβ (column labeled "Cells"). Experimental conditions were cells cultured with 20 μM Aβ (column labeled "Aβ"). Live cells fluoresced green from Calcein-AM, and dead cells fluoresced red from EthD. Scale bar is 200 μm; all micrographs are the same magnification.

Discussion

In a broad range of contexts, the epigenetics and morphology of cells *in vivo* can be well-approximated in 3D hydrogel cultures. Though simple hydrogels cannot recapitulate the entire complexity of *in vivo* tissues, they do provide strikingly similar results compared to 2D cell culture [24-26]. Depending on the application, the optimal physiochemical properties of the hydrogel model will vary. Type I collagen hydrogels have been applied to recapitulate *in vivo*-like cancer cell behaviors including migration and invasion [27-28, 279]. Agarose hydrogels are capable of allowing hepatocytes, fibroblasts, and other cell types to elaborate the distinct cellular zones that exist within respective tissues [29, 280-281]. The bioactivity of HA hydrogels has been utilized in stem cell differentiation and patient cancer cell expansion for personalized medicine [282-283]. In addition, drug delivery applications have utilized PEG hydrogels due to their biocompatibility and tunable degradation properties [284]. Features of hydrogels that may be important in applications include mesh size, chemical composition, stiffness, and the presence of ligands or functional groups that interact with the cell surfaces.

Hydrogels impart confinement by encapsulating proteins in a macromolecular network. The network serves to exclude solvent from proteins, which minimizes the ability of proteins to undergo changes in conformation and increases the local protein concentration; the net result is that confinement promotes proteins to undertake compact structures and favors protein-protein interactions. The degree to which a particular hydrogel exerts confinement on an encapsulated protein is inversely

proportional to the gel's mesh size. With this in mind, I predicted altered Aβ aggregation kinetics in gels with small mesh sizes (HA, PEG) vs. those with larger mesh sizes (collagen, agarose).

The attenuation of Aβ toxicity in hydrogels could potentially be influenced by cellular changes that occur due to cell-hydrogel interactions. Thus, I acknowledge that the biological activity of the hydrogel (e.g., integrin-binding motifs in collagen and CD44- and RHAMM-binding motifs in HA) may influence Aβ toxicity. Collagen is a commonly used hydrogel, but HA hydrogels could be more relevant to studies related to the brain wherein the main ECM molecules are HA, tenascins, and lecticans [266]. Basement membrane ECM molecules such as laminins and collagens are an important component of the blood-brain barrier and are found surrounding blood vessels in the brain [285]. Thus, I investigated Aβ aggregation and cytotoxicity in both biologically-active and inert hydrogels in order to uncover a possible role of bioactivity on cell susceptibility to Aβ toxicity.

The kinetics of Aβ aggregation was measured via ThT assay, wherein ThT fluorescence indicates the presence of β-sheet structures. The presence of β-sheet aggregates was negligible (no fluorescence) at the start of each experiment. This is consistent with the Aβ pretreatment process that was used to ensure a consistent population of Aβ monomers at the start of each experiment [253]. All conditions showed the presence of aggregated Aβ (ThT fluorescence) that increased over time according to one of four trends: 1) a pronounced lag phase then rapid aggregation, 2) a two-phase increase in fluorescence depicting an overall relatively slow rate of

aggregation, 3) a brief slow phase then rapid aggregation, and 4) a two-phase increase in fluorescence suggesting an overall relatively fast rate of aggregation.

For Aβ aggregation in solution, ThT fluorescence measurements consistently show a pronounced lag phase then rapid aggregation or a trend 1 curve (Figure 4.2). Both ThT and FCS measurements indicate that the only Aβ species present for up to 20 hrs were small, rapidly diffusing species that are devoid of β-sheet structures for at least 6 hrs (Figures 4.2, 4.3A & 4.4A). At these early times, the Aβ species present are likely monomers and dimers as well as a population of larger species (diffusivities of ~20 $\mu m^2/s$, Figure 4.3A, 4.4A) do not have extended β-sheet structure (do not bind ThT, Figure 4.2)

For Aβ aggregation in 3D hydrogels, all four types displayed the immediate presence of extended β-sheet structures and a population of large aggregate species (Figure 4.2, 4.3B-E & 4.4B-E). In other words, for all hydrogels, a type 1 curve was never observed, but instead displayed trend 2, 3, or 4 with some differences in magnitude depending on Aβ lot and random variation. Figure 4.2 depicts the most common curves observed for each hydrogel type: collagen shows trend 2, agarose shows trend 3, HA shows trend 3, and PEG shows trend 4. These trends are consistent with the idea that Aβ is confined in a hydrogel: PEG hydrogels have the smallest mesh size (~20 nm) and show the fastest Aβ aggregation, collagen hydrogels have the largest mesh size (~10 μm) and show Aβ aggregation occurring at a slower rate than in PEG gels, yet faster than in solution.

The variation or spread in aggregate size is also consistent with the idea that Aβ confinement and aggregation are influenced by hydrogel mesh size. The collagen and agarose hydrogels were measured by FCS to have a large range in aggregate size (Figure 4.3B & C), in comparison to the relatively small variation in aggregate sizes observed in HA and PEG hydrogels (Figure 4.3D & E). The size distribution of Aβ species was quite narrow in the PEG hydrogel (Figure 4.4E) as compared to the broader Aβ size distributions measured for the other hydrogel types that have larger mesh sizes. I suggest that the differences in Aβ species sizes may be due to Aβ having fewer possible configurations when the Aβ species size is of the same scale the hydrogel mesh size.

We expected that given the differences in the Aβ aggregation rate and size distribution observed in the four hydrogel types, coupled with differences in hydrogel bioactivity, that Aβ cytotoxicity would vary with the particular hydrogel type, but all hydrogels would be associated with lower cytotoxicity than that observed in solution. To my surprise, despite quantitative differences in Aβ aggregation kinetics and aggregate size distributions, all hydrogel materials completely attenuated Aβ toxicity for up to 72 hrs in culture (Figure 4.5 & 4.6). When Aβ aggregation was reexamined in hydrogels containing cells, there was no difference in respective aggregation kinetic curve types regardless of the presence of cells (data not shown). From the results presented herein, it appears the key feature relevant to Aβ toxicity that is consistent across all hydrogel types is the rapid stabilization of large β-sheet aggregates, suggesting that attenuated Aβ cytotoxicity in hydrogels may be due to a limited presence of Aβ oligomers that are available to interact with cells.

We acknowledge that Aβ aggregation also may be influenced by properties of the hydrogels (e.g., charge, hydrophilicity) that were not evaluated herein. Also, I cannot rule out that the attenuation of Aβ toxicity in hydrogels is influenced by confinement of the cells themselves or effects from the stiffness of the cellular microenvironment. However, I hold that these possibilities are unlikely given the evidence that 3D culture allows cells to more closely mimic *in vivo* phenotypes vs. 2D culture [24-26]. More importantly, Dr. Theresa Good reported in 2002 agarose itself does not confer a protective effect against the cytotoxicity of the Aβ 1-40 amino acid sequence [247]. Similar results were found with the 1-42 amino acid sequence of Aβ (unpublished data). Results presented herein may seem to contradict findings in her 2002 publication [247] that Aβ is toxic to cells in 3D agarose hydrogels. It is important to note that experiments herein utilized Aβ in the monomeric form, whereas the 2002 publication used pre-aggregated Aβ that contained a mixture of fibrils and smaller aggregated species, including the toxic 20 $\mu m^2/s$ diffusing species. In contrast, I report here that the intermediate 20 $\mu m^2/s$ diffusing species was not observed in any of the hydrogel types tested (Figures 4.3 and 4.4). Therefore, the current and 2002 reports are consistent in the idea that confinement in a hydrogel alters the kinetics of Aβ aggregation resulting in a) Aβ populations predominated by larger aggregate species (as opposed to Aβ in solution wherein oligomers are present for prolonged times), and b) attenuation of Aβ toxicity vs that observed 2D cultures.

Our findings have strong implications for *in vitro* models of disease. Aβ has been studied for decades in solution; wherein unstructured cytotoxic aggregates are clearly identifiable. Many drugs have been designed to target Aβ aggregation or

interactions with cells. Yet, astoundingly few AD drugs have been approved by the FDA. I demonstrate here that Aβ cytotoxicity is completely attenuated in 3D culture models composed of commonly-used hydrogels that have a broad range of physical, chemical and biological properties.

Stated more generally, I report that protein-protein interactions are altered in confined microenvironments. I suggest that this phenomenon may also relate to protein confinement as it occurs intracellularly and *in vivo.* Therefore, any field of research investigating protein structure and function in contexts relevant to those that exist *in vivo* should consider the potential impact of protein confinement by the local microenvironment.

Chapter 5 : Conclusions and Future Directions

AD is a devastating neurodegenerative disease that affects one in 10 people age 65 and older. Currently, there are no treatments to cure, prevent, or slow the progression of AD, but investigators are diligently searching for effective therapeutic treatments. Unfortunately, to date, drugs in development have not been able to achieve the efficacy shown in pre-clinical trials. AD is a slowly progressive disease that begins well before clinical symptoms emerge, making it near impossible to study the onset of the disease in humans. Investigators have depended on *in vitro* and animal models to understand the pathology, and design drugs to combat the disease.

Research that focuses on protein biophysics often requires high-resolution measurements to acquire protein structure details. The Aβ protein has a diameter of ~3 nm which is near the limit of electron microscopy. Other techniques that detect protein structure such as CD, NMR, and scattering techniques require specific conditions and data analysis to obtain structure information. To obtain unobscured data, proteins are typically studied in pure dilute solutions.

Three-dimensional *in vitro* cell models have been adopted across many fields because they provide an environment to allow cells to behave more similarly to cells *in vivo* as compared to 2D cultures. Although 3D *in vitro* AD models have recently been published, there has been no attempt to analyze the Aβ structure and aggregation in these 3D environments. The assumption that Aβ behaves the same in dilute solution as in a confined hydrogel is unlikely.

Crowding and confinement exclude soluble volume from the protein. This volume exclusion increases the local protein concentration, promotes protein-protein interactions, and encourages a compact protein conformation. Even though crowding and confinement influence protein structure and function, these potentially significant influences have often remained underappreciated or unacknowledged to occur in 3D culture models.

Herein, I suggest that the key to understanding the role of Aβ in AD is to study Aβ in *in vivo*-like confined environments. As reviewed in Chapter 2, biophysical techniques to study proteins in pure solutions may have limited adaptability for use in 3D hydrogels. Yet, analyzing Aβ within confined hydrogel scaffolds was expected to unveil an aggregation model that may more accurately depict *in vivo* aggregation in the brain vs. what has been described to occur in solution. This work sought to define Aβ aggregation in 3D cultures in order to provide an improved *in vitro* AD model to study disease pathology and develop more effective AD drugs.

Contributions of the current dissertation

In this work, I demonstrated that 3D confinement has a strong influence over Aβ structure and function. This project was inspired by an early observation that is described in Chapter 3: when Aβ monomers are encapsulated with PC12 cells in 3D collagen hydrogels, to my surprise, the cytotoxicity was attenuated compared to 2D culture. Subsequent biophysical analysis of Aβ in 3D hydrogels identified a different

aggregation pathway than the pathway that is widely acknowledged to occur in solution. From an initial state of Aβ monomers, I discovered that large aggregate species with β-sheet structures form rapidly (within minutes). In comparison, similar large aggregate species may require several hours to form in 2D solutions. My results suggest the 3D confinement shifts the aggregate equilibrium species from small unstructured, presumably toxic oligomers to β-sheet structured fibrils. However, based on these findings alone, I could not rule out potential cellular changes due to the collagen hydrogel itself that could alter cellular susceptibility to Aβ toxicity.

Chapter 4 reports my further investigation into the attenuation of Aβ toxicity that occurs in hydrogels. To complement the findings from the collagen hydrogel experiments, I added agarose, HA, and PEG hydrogels to my studies. I selected these particular hydrogels in order to determine the impact of mesh size (~ μm in collagen and agarose, ~nm in HA and PEG) and bioactivity (collagen and HA are bioactive, agarose and PEG are inert) on Aβ aggregation and cytotoxicity. Quantitative differences were observed between all four hydrogels from ThT assays of Aβ aggregation kinetics as well as FCS measurements of aggregate size distributions. However, despite these differences, all 3D hydrogel cultures strongly attenuated Aβ cytotoxicity compared to near complete cell death in 2D culture. Compared to Aβ in solution, all the hydrogels were associated with faster formation of β-sheet structures and a species population predominated by large aggregate species. This effect was observed in all hydrogels, regardless of their mesh size or bioactivity; therefore, I conclude that this phenomenon is not due to cellular changes enacted by interaction with collagen or HA. That said, based on these data, I cannot rule out the possibility

that the vastly different mechanical properties of hydrogels vs. 2D culture plates could alter the cells epigenetically, making the cells less susceptible to toxic oligomers.

In conclusion, this work has significant impact to the way drugs for AD are discovered and tested: I suggest that efforts to develop AD drugs using 2D *in vitro* models may overestimate the potential toxicity of Aβ, and thus offers an explanation for the decades of failed AD drug clinical trials. These findings imply that drug discovery and development for AD, and potentially other diseases, will more rapidly identify therapeutics with greater efficacy if 3D cultures are included in early testing stages.

Future directions

For researchers interested in these findings, I suggest the following ideas for future experimental directions.

- Whereas the data herein suggests that large Aβ species predominate in 3D hydrogels, direct visualization of the Aβ aggregates are required to confirm whether toxic oligomers are yet present in the 3D hydrogel. Hydrogels would need to be cryo-preserved in a vitreous state and imaged using cryo-TEM. A method would need to be developed to differentiate between the hydrogel scaffold and the Aβ aggregates that do not require excessive washing or labels that hinder Aβ aggregation.

- Though I have reported the association of more rapid Aβ aggregation with attenuated cytotoxicity, I cannot claim causation. The first step in this direction would be to determine whether cells directly associate with Aβ when cultured in a 3D hydrogel. Investigation of the Aβ localization within the hydrogel would unveil whether the Aβ is associating with cells, hydrogel structure itself, or perhaps both. Cross-correlation FCS or FRET could be used to identify interactions between the cell membrane and Aβ, or the hydrogel structure and Aβ.
- Tools such as RNAseq and quantitative PCR could be applied to identify cellular expression signatures that are associated with the resilience to Aβ toxicity that occurs in a 3D hydrogel.
- To start to identify a molecular mechanism that explains attenuated Aβ cytotoxicity in 3D hydrogels, prevailing theories of cytotoxicity pathways identified in 2D *in vitro* models (e.g., disrupted calcium signaling) could be probed in 3D hydrogels.
- Attenuated toxicity in confined environments could occur for other aggregating amyloid proteins. One such protein that could readily be investigated in this context is α-synuclein, which is associated with Parkinson's disease.
- The impact of 3D confinement most likely extends to all proteins. Therefore, other biologically relevant proteins should be investigated in 3D biomaterial scaffolds to determine if protein stabilization impacts the protein function.

- It is possible that drugs that inhibit or block Aβ aggregation may shift aggregate equilibrium species in confined environments back to small unstable oligomers such as those that predominate in 2D culture. Treatment with these types of AD drugs would confirm a possible "rescue" of Aβ toxicity in 3D cultures.
- Matrigel® is commonly used to model the brain because basement membrane ECM is located in blood vessels of the blood brain barrier. Laminin is part of the blood brain barrier located at blood vessels and is a potent inhibitor of Aβ fibrillization. It is unknown if the laminin fibril inhibition will promote a non-toxic or toxic form of Aβ in hydrogels. To begin to probe for this, laminin inhibition of Aβ aggregation should be tested in 2D vs. 3D hydrogels to determine Aβ toxicity.
- Development of a physiologically-relevant 3D *in vitro* AD model is the ultimate goal. Using brain ECM-relevant biomaterials to encapsulate and differentiate iPSCs derived from an AD patient would be ideal. Including a dual layer of endothelial cells encapsulated in basement membrane ECM such as Matrigel® could simulate the blood brain barrier. Neuroimmune interactions and the role of glia in AD could be probed in co-cultures with microglia and astrocytes.
- An advanced 3D *in vitro* AD model could reveal new insights into the disease pathology and be used to discover and develop drugs more rapidly and with greater efficacy.

Chapter 6 : Appendix

Appendix A – Control Data

Viability of PC12 cells in 2D and four 3D hydrogels

Cell viability was tested using a Live/Dead assay. Graphs for 2D culture and 3D collagen (Figure A.1A and B) were shown in Chapter 3 (Figure 3.1A and B). The same assay was conducted in Chapter 4 in agarose hydrogel, HA hydrogel, and PEG hydrogels but the raw percent viability graphs were not shown. Here I present the raw percent viability of all conditions, 2D and all four 3D hydrogel cultures. Significant cell death was seen in 2D culture (Figure A.1.A) at 24, 48, and 72 hrs. In all hydrogel cultures, Aβ toxicity was attenuated (Figure A.1.B-E).

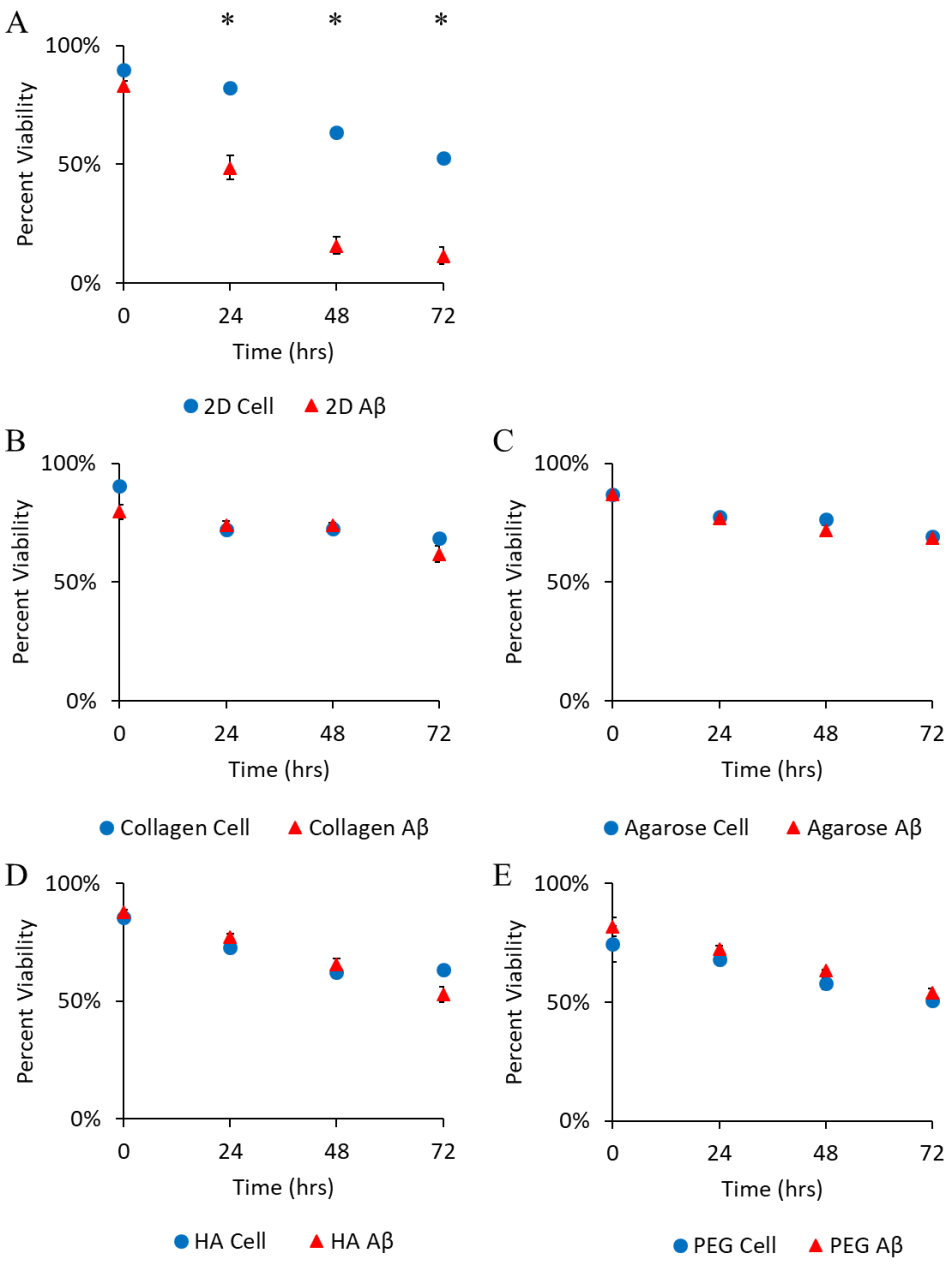

Figure A.1. *All 3D hydrogels attenuate Aβ cytotoxicity compared to 2D culture. Percent viability was tested with 20 μM Aβ (red triangle), and without Aβ (blue circle). These conditions were tested over 3 days in 2D culture (A), 3D collagen (B), 3D agarose (C), 3D HA (D), and 3D PEG (E).*

Serum attenuates Aβ aggregation in solution

Cells are typically maintained using medium supplemented with serum; however, serum can overshadow other experimental effects. Serum has also been shown to slow Aβ aggregation. Therefore, I ran a test to confirm [224]. Using the ThT assay, I tested Aβ aggregation in F12 medium without serum or supplemented with 1%, 5%, or 10% FBS (Figure A.2). The results showed a slowed aggregation rate and extended lag phase as serum was increased. Confirming serum slows Aβ aggregation; all experiments in this dissertation were conducted in serum-free conditions.

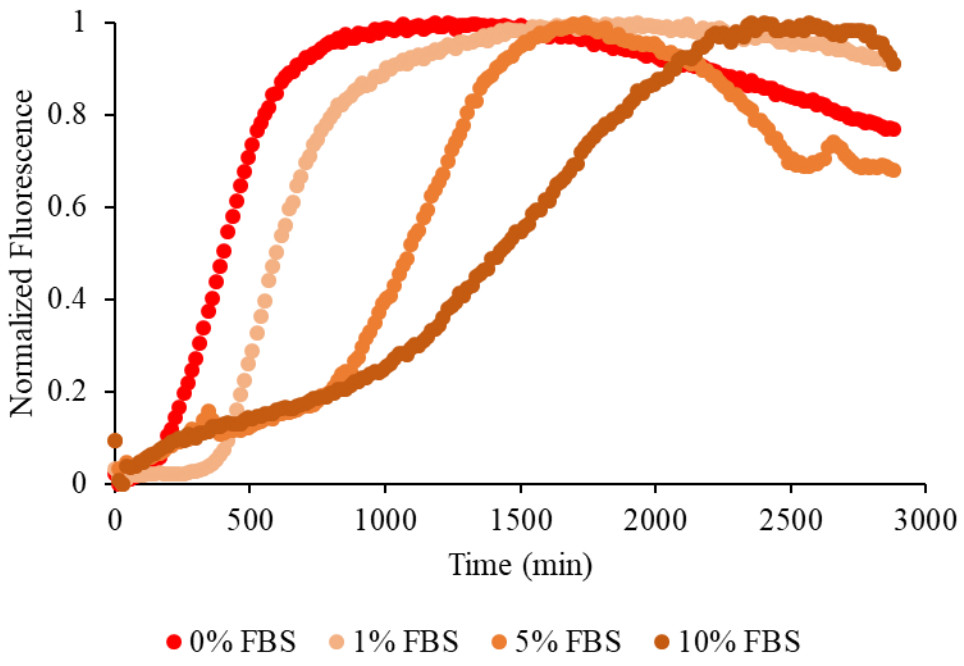

Figure A.2. *Serum slows Aβ aggregation rate and extends the lag phase. In F12 medium, 20 μM Aβ was aggregated with 20 μM ThT with 0% FBS (red), 1% FBS (light orange), 5% FBS (medium orange), or 10% FBS (dark orange).*

ThT kinetics of HiLyte 488-labeled Aβ incorporation

Fluorophore labeling of large non-aggregating proteins has little effect on protein function; however, Aβ is a small 42 amino acid protein that aggregates as stacked β-sheets. Fluorophore labeling of Aβ can affect the aggregation kinetics due to bulky fluorophores hindering β-sheet stacking [159]. For this reason, I used HiLyte Aβ in a 1:80 ratio with unlabeled Aβ in my FCS experiments. To confirm the 1:80 ratio did not affect the aggregation kinetics, I used a ThT assay to compare aggregation curves with and without HiLyte Aβ in a 1:40 ratio (Figure A.3.). In all cases, both solution and in hydrogels, the 1:40 ratio of HiLyte Aβ did not change the Aβ kinetics. This experiment was tested at a 1:40 ratio and showed no effect; therefore, the 1:80 ratio tested in my FCS experiments would not affect Aβ aggregation.

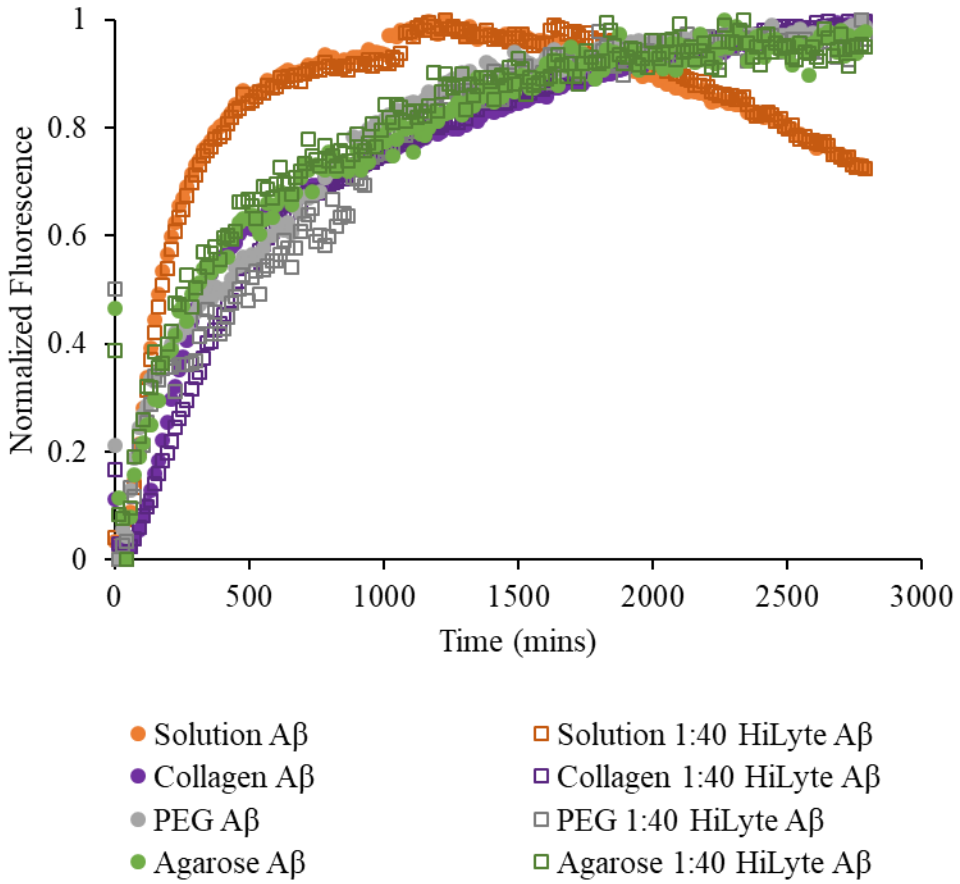

Figure A.3. *HiLyte 488 labeled Aβ did not inhibit aggregation. A ThT assay tested 10 μM Aβ alone (circle) or with 250 nM HiLyte Aβ – a 1:40 ratio (square). These conditions were tested in F12 solution (orange), collagen hydrogel (purple), PEG hydrogel (gray), and agarose hydrogel (green).*

No viability changes with Scr Aβ or HiLyte Aβ incorporation

Fluorophore labeling of Aβ can affect the aggregation kinetics due to bulky fluorophores hindering β-sheet stacking [159]. For this reason, I used HiLyte Aβ in a 1:80 ratio with unlabeled Aβ in my FCS experiments. I ran a live/dead assay to confirm the 1:80 ratio did not affect the Aβ cytotoxicity to 2D cultured cells or the toxicity attenuation of 3D cultured cells (Figure A.4. green diamond). Additionally, to confirm the specific Aβ42 amino acid sequence was responsible for the cytotoxicity in 2D culture, I tested a scrambled sequence of Aβ42 that is unable to fold or aggregate as native Aβ42 does (Figure A.4. yellow square). The Scr Aβ viability had no significant differences from the PC12 alone culture (Figure A.4. yellow square) – the decrease in viability is due to no medium changes over the 3 day culture. The incorporation of HiLyte Aβ in a 1:80 ratio decreased cell viability in 2D culture with no significant difference from unlabeled Aβ (Figure A.4.A green diamond). Additionally, there was no significant difference between HiLyte Aβ 1:80 and unlabeled Aβ in 3D culture where toxicity was attenuated (Figure A.4. B-E green diamond).

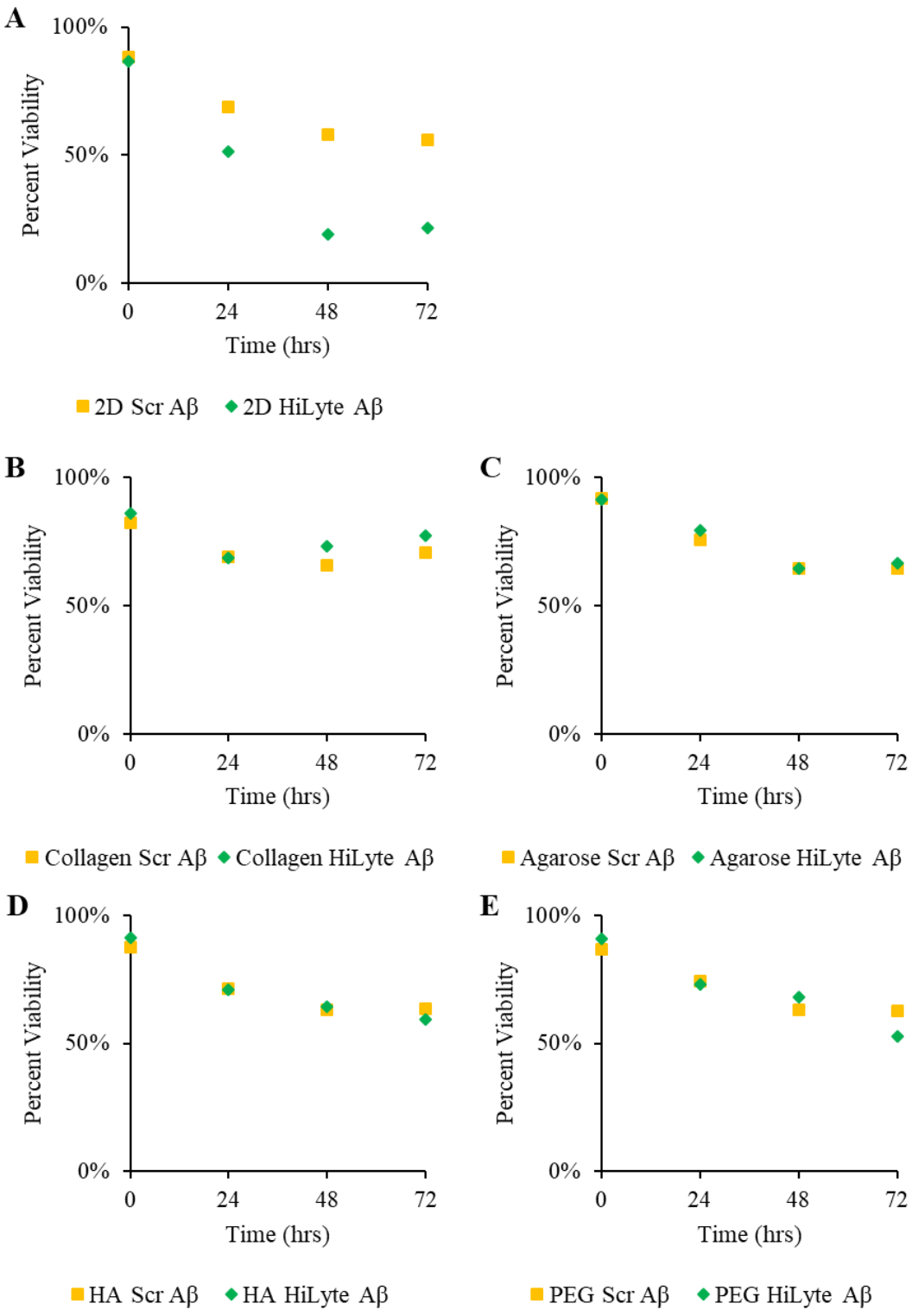
A
100%
50%
0%
Percent Viability
0
24
48
72
Time (hrs)
2D Scr Aβ
2D HiLyte Aβ
B
Collagen Scr Aβ
Collagen HiLyte Aβ
C
Agarose Scr Aβ
Agarose HiLyte Aβ
D
HA Scr Aβ
HA HiLyte Aβ
E
PEG Scr Aβ
PEG HiLyte Aβ

Figure A.4. *Scr Aβ is not cytotoxic, and HiLyte Aβ incorporation does not affect 2D cytotoxicity or 3D toxicity attenuation. Percent viability was tested with 20 μM Scr Aβ (yellow square), and with HiLyte Aβ in a 1:80 ratio with unlabeled Aβ (green diamond). These conditions were tested over 3 days in 2D culture (A), 3D collagen (B), 3D agarose (C), 3D HA (D), and 3D PEG (E).*

Variation in Aβ aggregation between companies

Aβ is an intrinsically disordered protein whose aggregation is highly stochastic by nature. I used a ThT assay to test Aβ aggregation from four companies: Bachem, Abcam, Tocris, and Alfa Aesar (Figure A.5. blue, orange, gray & yellow respectively). Aβ aggregation between companies varied in lag time, aggregation rate and total fluorescence. However, the trend between solution and 3D hydrogel remain consistent with each company, 3D had a shorter lag phase than solution. Due to the variation, in my dissertation, I show representative ThT data.

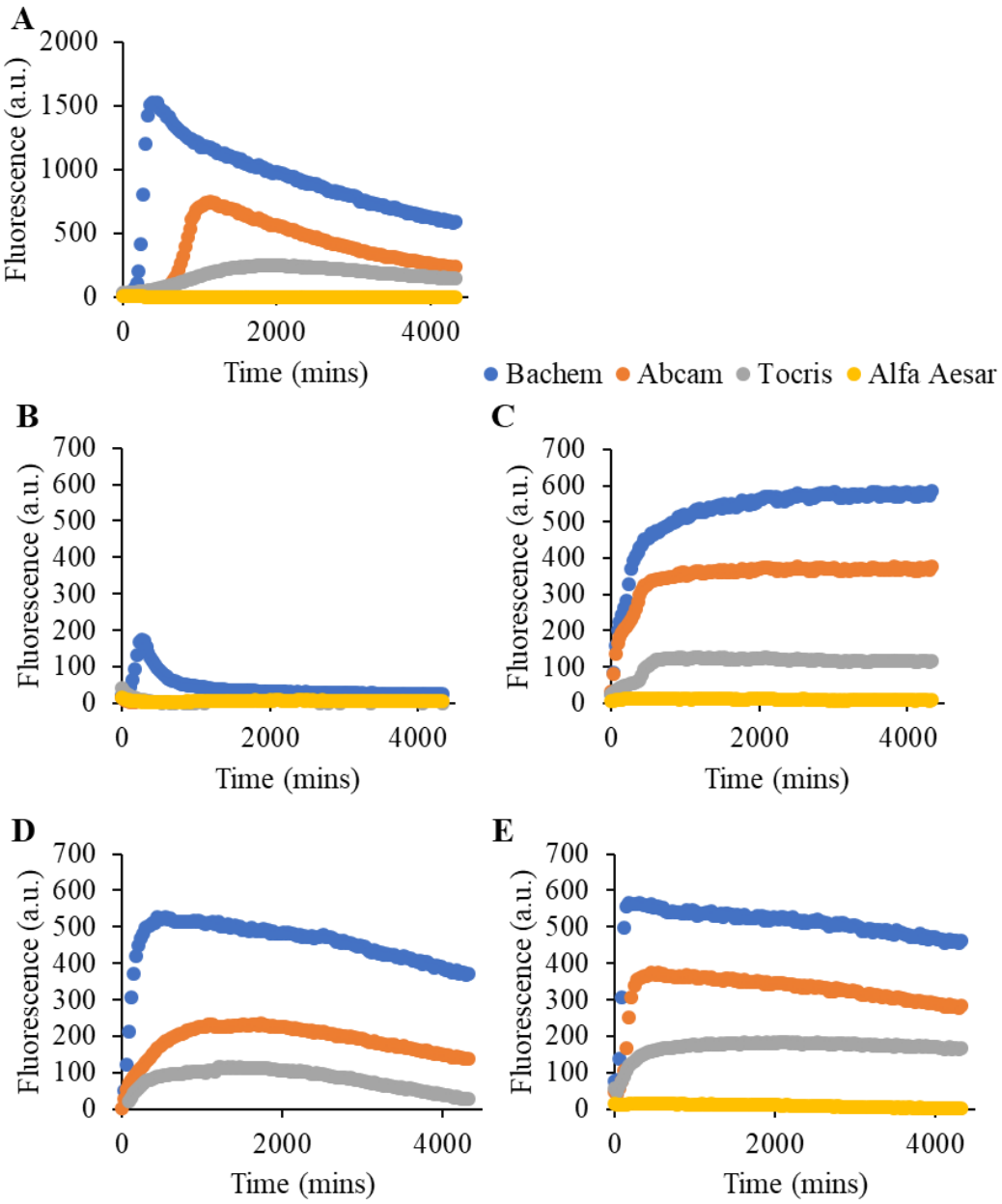

Figure A.5. *Stochastic nature of Aβ demonstrates variation between separate companies: Bachem (blue), Abcam (orange), Tocris (gray), and Alfa Aesar (yellow). Aβ from each company was tested in F12 solution (A), collagen hydrogel (B), agarose hydrogel (C), HA hydrogel (D), and PEG hydrogel (E).*

Variation in Aβ aggregation between lots

Aβ is an intrinsically disordered protein whose aggregation is highly stochastic by nature. GenScript supplied three lots of Aβ, each having variation in lag time, rate and total fluorescence (Figure A.6). Although there are lot to lot differences, the trends between solution and 3D aggregation remain consistent. In my dissertation, representative curves are shown in my ThT experiments.

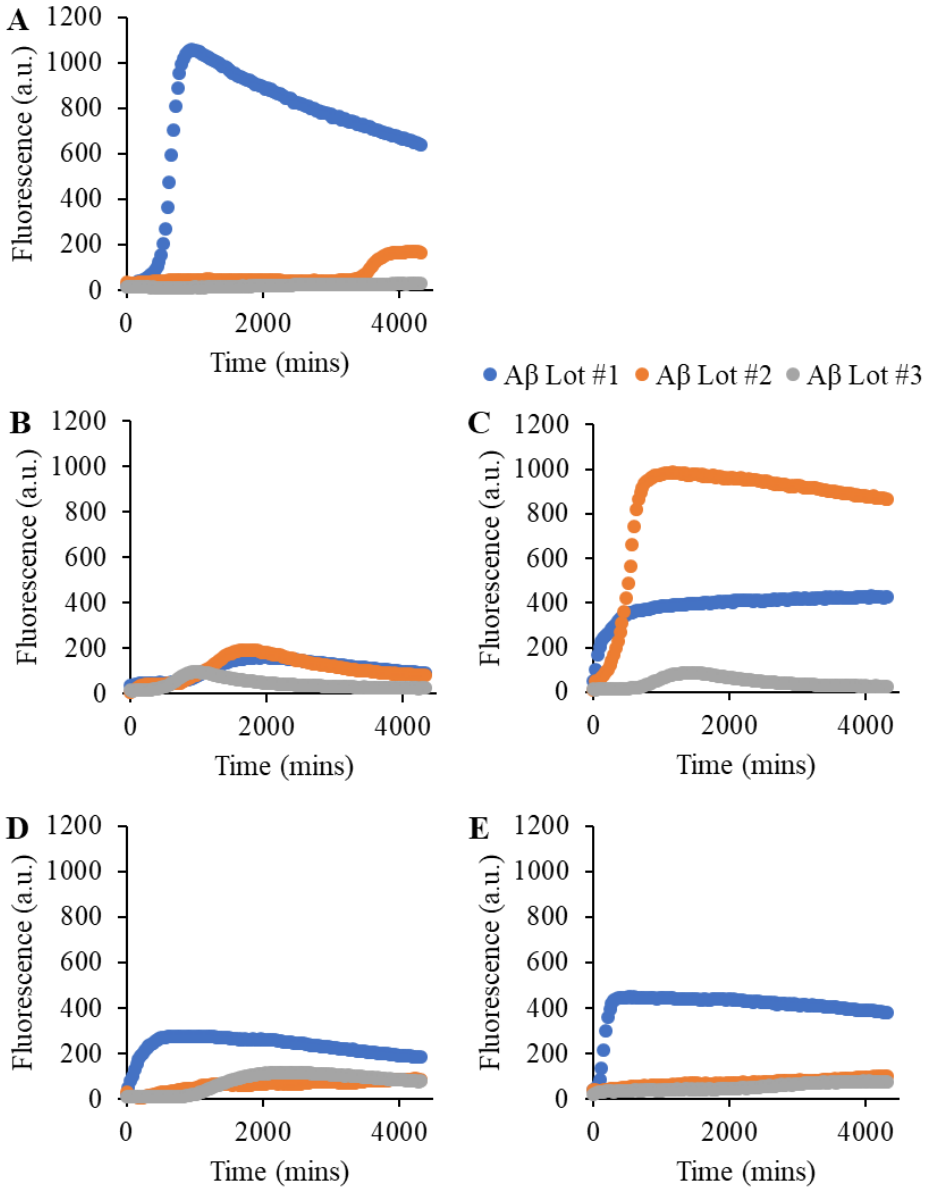

Figure A.6. *Stochastic nature of Aβ demonstrates variation between separate lots from GenScript. Three separate Aβ lots were tested with a ThT assay: lot #1 (blue), lot #2 (orange), and lot #3 (gray). The Aβ lots were tested in F12 solution (A), collagen hydrogel (B), agarose hydrogel (C), HA hydrogel (D), and PEG hydrogel (E).*

Aβ pretreatment: HFIP vs. NH_4OH

I pretreated Aβ to break existing β-sheets and start my experiments with a structure free state. Traditionally HFIP is an organic acid that is a known β-sheet breaker and has been used to treat Aβ. However, using diluted HFIP causes aggregation; therefore, 100% solution was used in this dissertation and was removed by vacuum desiccation overnight. Recent publications recommend using NH_4OH rather than HFIP [242]. I tested this method, and one disadvantage I found was that NH_4OH must be lyophilized, which caused the small aliquots of Aβ to cling to the walls of the tube. This made it challenging to dissolve to 222 μM because, in a 0.1 mg aliquot, 100 μl was used which could not pull Aβ off the walls. I analyzed this method with ThT kinetics and TEM analysis. After dissolving the pretreated Aβ back into solution to 222 μM, TEM saw minimal β-sheet structure in the HFIP pretreated samples, whereas small β-sheet fragments were identified in the NH_4OH pretreated samples (Figure A.7 A & B respectively). ThT analysis in solution and hydrogels found that Aβ in solution did not have a lag phase, but rapid aggregation in NH_4OH samples (Figure A.7 C). The β-sheet structure found in TEM seeded aggregation in solution where I would typically see an extended lag phase lacking structure. My results found HFIP to remove β-sheet structure more effectively than NH_4OH; therefore HFIP pretreatment was used in this dissertation.

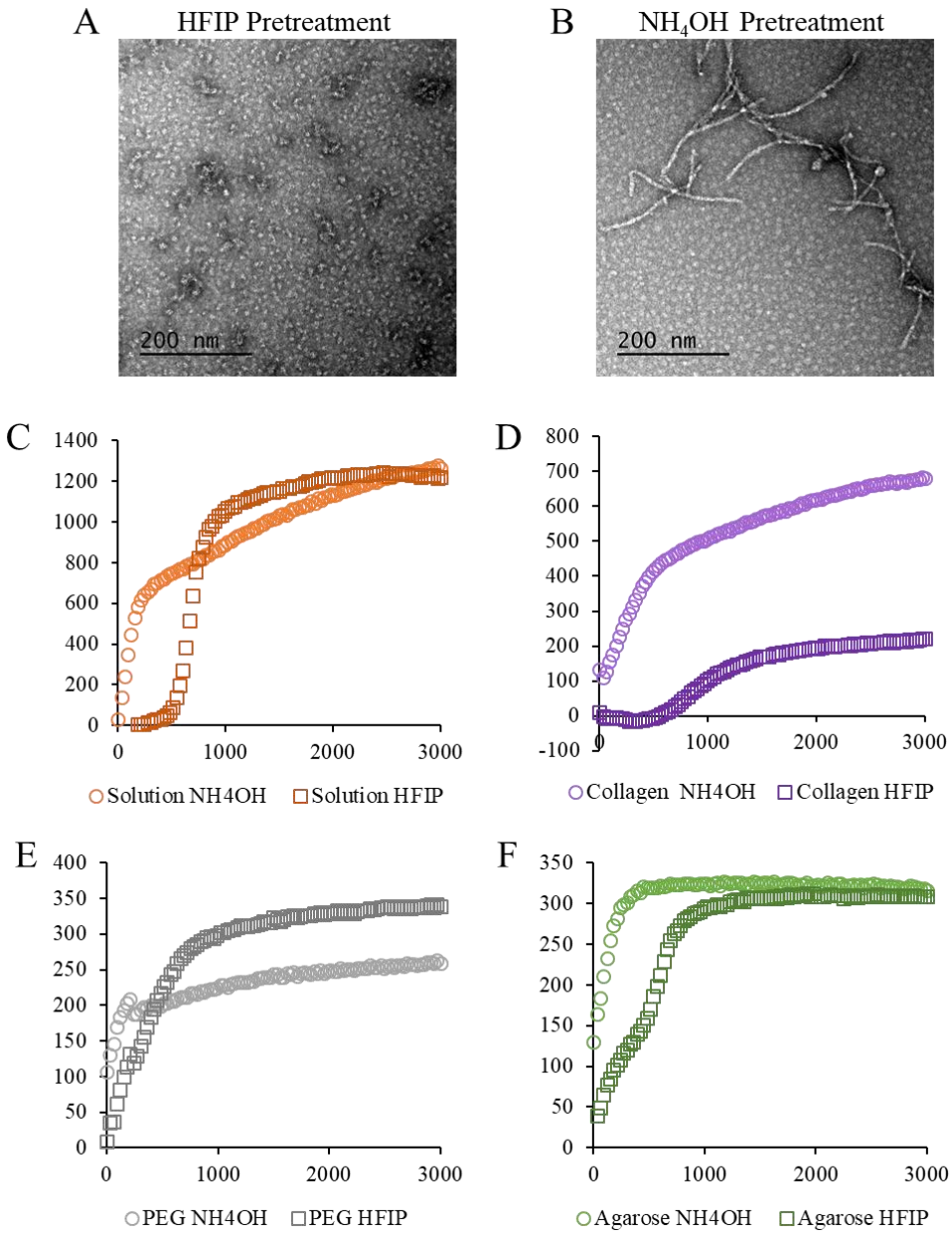

Figure A.7. HFIP pretreatment of Aβ removes existing β-sheet structure more effectively than NH_4OH. TEM images of HFIP pretreatment (A) and NH_4OH pretreatment (B). Aβ aggregation kinetics comparing HFIP (circle) and NH_4OH (square) in solution (C orange), collagen hydrogel (D purple), PEG hydrogel (E gray), and agarose hydrogel (F green).

Matrigel® inhibits Aβ aggregation

Current 3D *in vitro* AD models use Matrigel as their hydrogel; however, laminin (60% of Matrigel®) is a potent inhibitor of Aβ aggregation. I tested Aβ aggregation kinetics using a ThT assay and found Matrigel® to have minimal fluorescence compared to other hydrogels and solution over the 2 days (Figure A.8). With my results, I proceeded with experiments without Matrigel®.

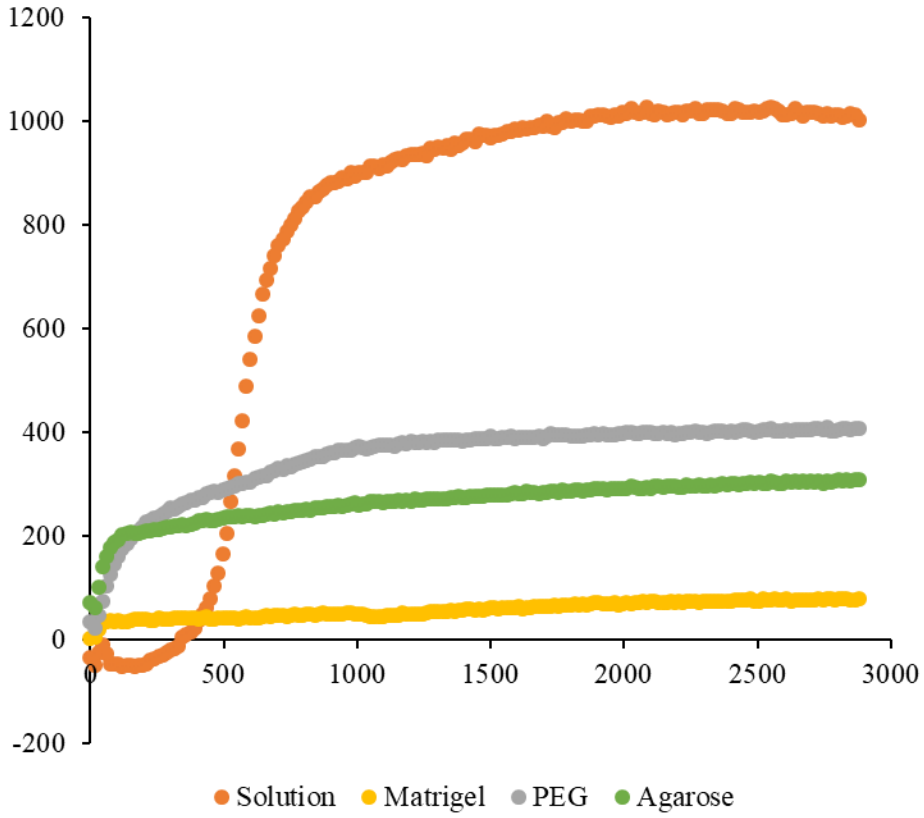

Figure A.8. *Matrigel inhibits Aβ aggregation. 10 μM Aβ was tested in solution (orange), Matrigel® (yellow), PEG (gray), and agarose (green). Rapid aggregation in agarose and PEG while solution has a lag phase. Matrigel has a minimal increase in fluorescence.*

ThT Aβ kinetics with cells and controls

I initially hypothesized that Aβ aggregation kinetics would be slowed when cells were incorporated due to Aβ – cell membrane interactions. Live cells have the potential to have active interactions with Aβ; therefore I ran additional controls to account for other explanations. Dead cells were tested to account for basic lipid membrane association with Aβ and microparticles (μparticle) were tested as a control to account for mesh size disturbance from 10 μm spheres being incorporated. To my surprise, the lag time in all hydrogels and solution did not differ from basic Aβ aggregation in each respective environment (Table A.1). While growth rate and total fluorescence had more variation, I found in Chapter 4 that despite variations in ThT kinetics, the determining factor in cytotoxicity was the extended lag phase.

	Lag Time			Growth Rate			Fluorescence Total		
	←	−	→	↓	−	↑	↓	−	↑
	F12								
Live Cells	11%	67%	22%	22%	78%	0%	78%	22%	0%
µparticle	20%	80%	0%	20%	80%	0%	40%	20%	40%
Dead Cells	0%	100%	0%	0%	100%	0%	67%	33%	0%
	Collagen								
Live Cells	25%	63%	13%	13%	38%	50%	50%	13%	38%
µparticle	33%	50%	17%	17%	50%	33%	50%	17%	33%
Dead Cells	33%	67%	0%	0%	33%	67%	33%	0%	67%
	PEG								
Live Cells	11%	67%	22%	22%	56%	22%	67%	11%	22%
µparticle	17%	83%	0%	17%	67%	17%	33%	33%	33%
Dead Cells	0%	100%	0%	0%	75%	25%	25%	50%	25%
	Agarose								
Live Cells	13%	63%	25%	50%	38%	13%	63%	0%	38%
µparticle	0%	100%	0%	0%	50%	50%	0%	100%	0%
Dead Cells	0%	100%	0%	0%	100%	0%	0%	100%	0%
	Hyaluronic Acid								
Live Cells	17%	67%	17%	67%	33%	0%	50%	33%	17%
µparticle	0%	100%	0%	20%	40%	40%	60%	20%	20%
Dead Cells	0%	100%	0%	25%	50%	25%	50%	25%	25%

Table A.1. *Cell incorporation did not affect Aβ lag phase. ThT curves studying Aβ with live cells/dead cells/µparticles were compared to ThT curves of Aβ alone and grouped into less than (←↓), equal to (−), or greater than (→↑) categories. Each grouping was divided by the number of experiments tested to give the percent of the population in each category.*

Appendix B – Lab Protocols

Aβ Preparation

Supplies

- HFIP
- NaOH
- Water
- PBS
- 1 ml sterile plastic syringe
- 1 ml glass syringe
- Beveled needle
- Blunt tip 2” needle
- Ultra-small syringe filter
- Glass scintillation vial
- Glass small volume inserts
- Vacuum desiccator

Methods

Monomerize and aliquot stock protein

Aβ is delivered as a lyophilized powder. To ensure the protein I work with is starting at the same point I pre-treat the delivered lyophilized powder and aliquot out samples.

1. Hexafluoroisopropanol (HFIP) should be added 1 ml per 1 mg of Aβ.

Note HFIP is a strong organic solvent, work in a fume hood with proper gloves, eye protection and lab coat. Plastic pipette tips will start to dissolve when in contact with HFIP, use a glass syringe if possible.

2. Puncture the rubber stopper with a free needle to allow air to leave as you inject the HFIP with a needle attached to the glass syringe. Remove both needles and

swirl vial gently. Allow to dissolve for 30 – 60 mins, until the solution is clear with no particulates.

3. Hold the glass vial to the light and gently swirl to look for floating particulates. Try to take a picture.
4. Aliquot solution into glass scintillation vials. Use glass small volume inserts if using < 150 µl for aliquot.

Note Silicone will start to dissolve in HFIP, only use silicone tubes during your experiment set up when HFIP has been evaporated off. Calculate out what size aliquots you will need for the experiments you will run.

5. Using a micropipettor, accurately pipette the proper amount in to each labeled microcentrifuge tube.
6. Keeping the lids open, place into vacuum desiccator, and turn on the compressor. Make sure thick reinforced tubing is used to connect compressor. Allow to run under vacuum for an hour or more depending on aliquot size. When done there will be no liquid left, only a clear peptide film.
7. If there are crystals or particulates in the dried peptide take a picture and make note in lab notebook.
8. Store at -20^{o}C or -80^{o}C.

Concerns HFIP treatment brings the peptide through its isoelectric point which is where it is most prone to aggregate. Extended time in HFIP has also shown to induce aggregation. Other papers show it is not as effective at breaking stable fibrils and leaves aggregate seeds behind. The strong solvent has the potential to extract plastic into the solution interacting with the peptide.

Preparing Aβ for Experiment

Aβ aliquots are specific amounts and will be reconstituted to a final concentration of 222 µM. For 1 mg Aβ, it will be dissolved in a final volume of 1ml. Diluted in a 2:7:1 ratio of 60 mM NaOH : water : PBS. Prepare Aβ once everything else is ready in your experiment. You don't want the concentrated solution sitting for long because aggregation with occur faster.

1. Make fresh 60 mM NaOH from stock bottle, diluted with DI water.
    a. 470 µl water + 30 µl 1 M NaOH = 500 µl 60 mM NaOH
    b. Filter the NaOH into a 2 ml eppendorf tube using a small diameter syringe filter.
2. Calculate 20% of the final Aβ aliquot volume. Add the calculated 20% volume of NaOH to the peptide film making sure not to touch tip to peptide film. Let sit at room temperature for 2 min.
    a. 1mg Aβ has a final volume of 1000 µl, 20% is 200 µl, therefore use 200 µl NaOH.
3. Add 70% final sample volume of deionized water to NaOH + Aβ. Close tube and put in floatation holder, place in water for the sonicator and sonicate for 5 min.
4. Take out of sonicator and floatation holder and wipe excess water off of the tube with a kim wipe.
5. Filter sterilize with a 1 ml syringe and ultra-small volume syringe tip filter. You will lose some solution to the filter so make sure you plan for about 50-100 µl

extra. Filtration will sterilize the solution for cell culture as well as remove undissolved protein aggregates.

a. Using purple blunt tip transfer needle, transfer Aβ solution from scintillation vial into the syringe. Once solution is completely out of tube, turn syringe with the needle facing up and slowly suck in air to get all the solution out of the needle.
b. Remove the needle from the syringe and set to the side to be put in a sharps container.
c. Place the ultra-small volume syringe tip filter on to the syringe and twist on lure lock.
d. Slowly press solution through filter into a sterile siliconized microcentrifuge tube in a TC room hood.

6. Add 10% final sample volume of sterile PBS. Pipette solution a few times avoiding bubbles. Salt stabilized the beta sheet structure allowing the protein to aggregate, therefore adding PBS after filtration prevents protein loss on the filter.
7. Aβ monomer solution is ready to be added to gels and solutions for an experiment.

Collagen coating flasks and well plates for PC12 culture

Supplies

- Rat Tail Collagen I (3.39 mg/ml may vary by batch)
- 0.02 N Acetic Acid
- 15 ml conical tube
- Flask or well plate

Methods

Dilute collagen to 50 µg/ml with 0.02 N acetic acid. Plate at 5 µg/cm^2 for PC12 cells.

T75 Flask

Surface area: 75 cm^2

5 µg/ cm^2 · 75 cm^2 = 375 µg

375 µg / 50 µg/ml = 7.5 ml

(50 µg/ml · 7.5 ml) / 3.39 mg/ml = 110.6 µl

110.6 µl collagen + 7.389 ml 0.02 N acetic acid

96 Well Plate

Surface area: 1.13 cm^2

5 µg/ cm^2 · 1.13 cm^2 = 5.65 µg (per coverslip)

5.65 µg / 50 µg/ml = 0.113 ml (per coverslip)

24 coverslips + 2 extra = 26 · 0.113 ml = 2.938 ml

(50 µg/ml · 2.938 ml) / 3.39 mg/ml = 43.3 µl

43.3 µl collagen + 2.938 ml 0.02 N acetic acid

- Let collagen solutions incubate at 37°C for 1 hour or 2 hours on the bench top.
- Rinse with PBS, then water, and finally cell culture media.
- Use immediately or may be stored at 4°C for 1-2 weeks.

Notes:

- Coating concentrations may differ for different cell lines, check what works best for yours.
- Too much or too little collagen can interfere with cell attachment, optimize concentrations for best results.
- Collagen begins to polymerize when the temperature rises, therefore work quickly with the concentrated stock solution.

PC12 cell culture

Supplies

- 15 ml conical tubes
- Trypsin
- PBS
- Growth medium (w/ serum)
- SF Neurobasal medium
- Gentamicin
- Sterile pipette tips
- Sterile pipettes
- Pipettors
- Hemocytometer

Methods

1. Remove old medium from PC12 culture T75 flask and rinse with 5 ml sterile PBS then remove PBS.
2. Add 6 ml trypsin to T75 flask and incubate for 5 min. Tapping the bottom of the flask or incubating in the incubator will speed cell detachment. Rock flask gently side to side to see if cells are lifted or check on the microscope.
3. Add 6 ml of growth medium w/ serum to deactivate the trypsin. Pipette the cell solution multiple times, spraying the liquid over the entire surface of the flask to lift any remaining cells.
4. Collect cell solution in a sterile 15 ml conical tube, cap, then centrifuge at 4,000 g for 4 min to pellet the cells.
5. Check for the pellet, then dump the supernatant. Resuspend cell pellet with 10 ml growth medium. Pipette up and down to break up cell clumps ~ 20 times. Avoid making bubbles because they damage the cells.
6. With a micropipetor collect 10 µl of cells and inject onto the hemocytometer.

7. Count the number of cells in each of the 4 quadrants. Count cells on the 2 outer sides, and skip cells on the 2 inner sides of each quadrant.
8. Average the 4 quadrants, this equals the average number of cells x 10^4 cell/ml. You have 10 ml total, therefore you can calculate the total number of cells in your solution.

Avg # = _____* 10^4 cell/ml = **_____k cell/ml** * _____ml

= _____cells total

9. To continue culturing cells, take a collagen coated T75 flask from the refrigerator and wash with 7 ml growth medium, then dump.
10. General recommended seeding density is 2.1 x 10^6 cells in a T75 flask. Add growth medium and cells from the 15 ml tube. Rock the plate gently to mix and spread cells across the plate.
11. Add gentamicin from the refrigerator at a concentration of 20 µg/ml. Stock is 20 mg/ml, therefore add 30 µl gentamicin to the 15 ml culture solution.

Cell Methods for Experiments

1. After the hemocytometer, determine how many cells you need for your experiment, and at what concentration you need to add the cells. Hydrogel culture needs highly concentrated cells (~7000 kcell/ml) where 30 µl cells goes into a 400 µl pre-gel solution.
2. Into a sterile tube, pipette the volume containing the desired number of cells for your experiment and centrifuge at 4,000 g for 4 minutes to pellet.

3. Check for a pellet and dump the supernatant. Resuspend pellet with Neurobasal medium to the cell concentration needed for the experiment.

Avg # = _____* 10^4 cell/ml = _____**k cell/ml** * _____ml

= _____cells total

$$\frac{\text{need 3,000 k cells}}{\text{\_\_\_\_\_ k cell/ml}} = \text{\_\_\_\_\_ ml from stock cell tube.}$$

resuspend in _____ml to reach 7,000k cell/ml

Maleimide modification of HA

Supplies

- HA
- MES buffer
- EDC
- NHS
- AEM
- NaCl
- Water
- 15 ml conical tubes
- Rubber bands
- Bottle filter
- Plastic wrap
- Dialysis tubing 45mm, 12 - 14 kD

Calculations

$$\text{HA} \quad \frac{0.1\text{ g}}{242{,}000\text{ g/mol}} = 4.133\times10^{-7} \times 623 = \frac{0.258\text{ mmol}}{50\text{ ml}} = 5.15\text{ mM}$$

$$\text{EDC} \quad \frac{0.1438\text{ g}}{191.7\text{ g/mol}} = \frac{0.75\text{ mmol}}{50\text{ ml}} = 15\text{ mM}$$

$$\text{NHS} \quad \frac{0.08632\text{ g}}{115.09\text{ g/mol}} = \frac{0.75\text{ mmol}}{50\text{ ml}} = 15\text{ mM}$$

$$\text{AEM} \quad \frac{0.127\text{ g}}{254.16\text{ g/mol}} = \frac{0.25\text{ mmol}}{50\text{ ml}} = 10\text{ mM}$$

0.1 M MES Buffer:

48.8 g in 400 ml deionized water, pH 5.5 w/ NaOH, bring to 500 ml

Methods

HA modification chemistry

1. Dissolve HA in 50 ml MES 0.1 M with a stir bar.
2. Add EDC and NHS at the same time to the stirring HA solution. React for 30 mins.
3. Dissolve AEM in a separate beaker in 50 ml MES 0.1 M with a stir bar.
4. After the 30 min incubation, add AEM solution to the HA/EDC/NHS solution. React for 4 hrs stirring. Cover beaker with plastic wrap to prevent evaporation.
5. Fill a large bucket with 12 L deionized water + 35 g NaCl. Stir solution with large stir bar to dissolve NaCl.
6. With dry gloves, cut a 18 cm long piece of dialysis tubing (45 mm, 12 – 14 kDa) for a 100 ml batch.
7. Set the stir bar for the dialysis bucket to low and let the dialysis tubing soak for 20 mins.
8. Once the solution has reacted for 4 hrs, retrieve the dialysis tubing from the water bucket. Fold one end over on itself, ~ 1 cm, and fold a second time. Use a dialysis clip (weighted one if possible) and clip across the double folded bit of tubing.
9. Use a 25 ml pipette to transfer the HA solution into the dialysis tubing at the open end. Rub the open end between your fingers, this will help separate the pieces.

Note Put the pipette at least half way into the tubing before you pipette out the solution. Initially the tubing is stuck together and pipetting at the opening may not open the tubing, causing your reaction solution to spill out.

10. Transfer all 100 ml of HA solution into the dialysis tubing. When filled, gently remove air from the tubing.
11. You can fold the open end over twice and clip it if you want to. Then use a binder clip to clip the top of the tubing to the edge of the bucket. Keep the stir bar on low and run the dialysis for 3 days.
12. Fill a large beaker with deionized water and move the dialysis tubing bag from the bucket to the beaker.
13. Dump out the salt water, rinse the bucket, and fill with deionized water.
14. Put the dialysis tubing bag back into the bucket of deionized water clipped to the side. Run the dialysis for 3 more days with the stir bar on low.
15. Take the dialysis tubing out of the bucket. Hold the tubing toward the top above the solution collected at the bottom. Above the hand holding the tubing, cut the dialysis tubing open.
16. In a new clean beaker, pour or transfer with a pipette, your HA solution.
17. Take the beaker with HA to a sterile hood and set up a sterile bottle filter. Filter your HA solution.
18. Aliquot your sterile HA into sterile 15 ml conical tubes, 7 ml each tube. Label your tubes.
19. Freeze the HA aliquots in a -80^{o}C freezer overnight.
20. In a sterile hood, set up kim wipes and rubber bands and bring the frozen HA aliquots into the hood, open the lids and cover each tube with a folded kim wipe and hold in place with a rubber band.

21. Gently cap the tubes over the kim wipes, don't tighten down all the way. Put the HA aliquots back into the -80°C freezer for an hour.
22. Quickly take the HA aliquots out of the freezer, and place ~ 6 tubes into a lyophilizer jar. Gently take off the cap and place it in the bottom of the jar before you put the tube in.
23. Put the lyophilizer lid on the jar and put it on the lyophilizer tree securely. Slowly turn the dial to engage the vacuum. Lyophilize samples for ~ 3 days. Samples will look like cotton balls.
24. When done, turn off the dial on the lyophilizer branch and take the jar off the lyophilizer. Collect HA aliquot tubes and caps.
25. In a sterile hood, remove the kim wipes from the tubes and cap them. Store them at -20°C.

<u>HA modification analysis</u>

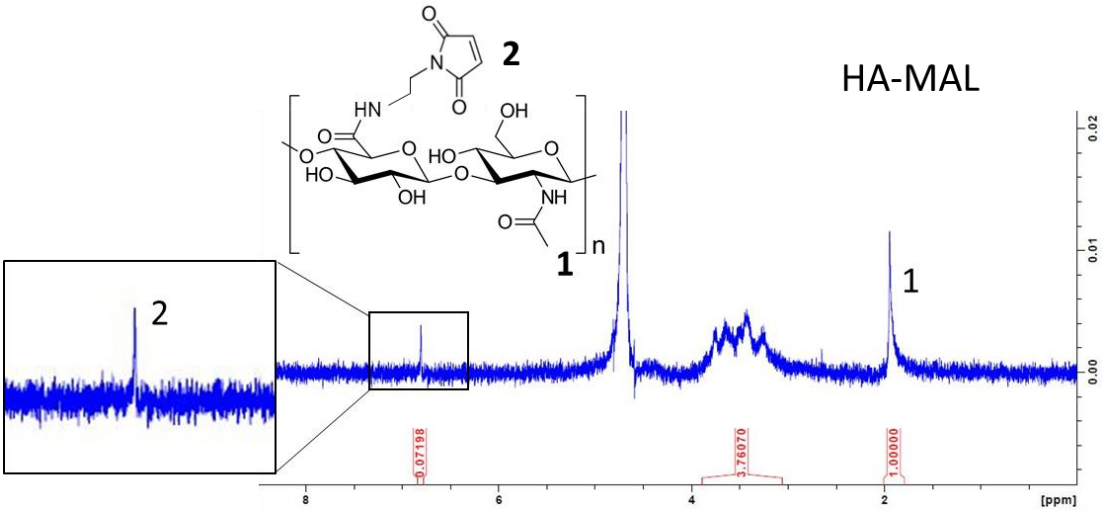

Figure B.1. NMR spectra of maleimide modified HA. Peak 1 is the COOH and peak 2 is the Maleimide. Dividing peak 2 by peak 1 x 100 gives the percent molar modification.

A 1 mg sample of HA-Mal is sent for NMR H+ analysis. The NMR spectra seen in Figure B.1. has a COOH peak (1), and a maleimide peak (2). Dividing peak 2 by peak 1 and multiplying by 100 gives the molar percent modification of maleimide. In Figure B.1. the HA repeating unit (without the HA modification) has a molecular weight of 388.327 g/mol. The HA I used in this dissertation has a molecular weight of 242,000 g/mol. Multiplying the number of COOH groups on a HA chain by the molar percent maleimide modification tells me the number of maleimides on a HA chain. This is important when calculating the molar concentration of maleimides for HA, and molar concentration of thiols on PEG in Michael type click reaction hydrogels.

Molar percent modification:

$$\frac{\text{Peak 2}}{\text{Peak 1}} = \frac{0.07198}{1.00} \times 100 = 7.2\% \text{ modified}$$

$$\frac{242{,}000 \text{ g/mol}}{388.327 \text{ g/mol}} = 623 \text{ COOH groups on one HA chain}$$

623 COOH sites x 7.2% = 44.856 maleimide per HA chain

Hydrogel preparation

Collagen Hydrogel

Supplies

- Collagen
- Water
- Sodium Bicarbonate
- 5x DMEM w/out phenol red
- 2 ml Microcentrifuge tubes
- Sterile pipette tips
- Pipettors

Example Calculations

Order			**Sample 1**	**Sample 2**
1	20%	5x DMEM	40 µl	40 µl
2	10%	Sodium Bicarbonate	20 µl	20 µl
6	1 mg/ml	Collagen I	59 µl	59 µl
3		Water	61 µl	41 µl
5	10%	Cells	20 µl	20 µl
4	10%	*Other*	0 µl	20 µl
		Total	200 µl	200 µl

Stock Collagen: 3.39 mg/ml

$$\frac{1 \text{ mg/ml} * 200 \text{ µl}}{3.39 \text{ mg/ml}} = 59 \text{ ul}$$

Methods

1. Determine the volume of your hydrogels and the concentration of cells in the hydrogel.
    a. If you want 10k cells in one 20 µl gel and you are making enough for 10 gels (aka 200 µl), then you need 10k cells * 10 (gels) = 100k cells in 20 µl.
2. You should make a solution of cells that contain more than enough such as 600k cells in 120 µl.

    600k cells = _____ml from stock cell tube. Resuspend in 120 µl.

    _____ **k cell/ml** (from cell collection tube)

3. Combine components in correct order adding the collagen last. The "other" may be Aβ, ThT, or other additives; adjust the water balance accordingly.
4. Carefully pipette a droplet of collagen/cell solution onto the center of the well to create a small droplet gel.
5. Incubate at 37°C for 15 mins and check for polymerization. When polymerized the gel will become cloudy or hazy, hold to the light and check.
6. For cell culture, once collagen has gelled, add Neurobasal medium + 20 µM gentamicin to each well. Collagen gels may lift from the well bottom.

Agarose Hydrogel

Supplies

- 1x SeaPlaque agarose
- 2x DMEM/F12 w/out phenol red
- 2 ml Microcentrifuge tubes
- Sterile pipette tips
- Pipettors

Methods

1. Heat 1x agarose in a water bath set to 68^{o}C to melt.
2. Determine the number of hydrogels and the volume of the hydrogels to calculate the total agarose hydrogel solution volume. Plan to make enough for 2 extra hydrogels per condition.
3. Determine the concentration of cells in the hydrogel and pick a volume of concentrated cells to add to your hydrogel solution. See collagen hydrogel 1.a.
4. Calculate the volume of potential additives (Aβ, ThT, HiLyte Aβ), based on stock concentrations described in Material and Methods of Chapter 4.
5. Subtract the total volume of additives from the total agarose hydrogel solution volume. Then divide by two, this is the volume of 1x agarose and 2x DMEM/F12.
    a. Say you have a total agarose volume of 500 µl. You would need 45 µl of stock Aβ (222 µM) to have a final concentration of 20 µM. Say you are adding 20 µl of cells too. Then 500 µl – 45 µl – 20 µl = 435 µl, 435 µl / 2 = 217.5 µl.
6. Mix together the 2x DMEM/F12 and the experimental additives in a sterile tube.

7. Take the melted 1x agarose and allow it to cool for 1 min in the hood before mixing into the DMEM/F12 solution. Vortex briefly to mix.
8. Pipette droplets of agarose solution into the center of the wells.
9. Allow the agarose hydrogels to cool and solidify for 10 mins at room temperature.
10. For cell culture, add warmed Neurobasal medium + 20 μM gentamicin to each well.

Comments HA is viscous at a 1% solution and cannot be filtered and UV causes crosslinking. Therefore, sterile filtering during this chemistry makes the HA acceptable for cell culture. Use aseptic technique when handling HA aliquots.

Hyaluronic Acid Hydrogel

Supplies

- HA sterile aliquot
- PEG dithiol
- Neurobasal medium
- 2ml Microcentrifuge tubes
- Sterile pipette tips
- Pipettors
- Tweezers
- 1ml sterile syringe
- Blunt tip needle
- Ultra-small syringe tip filter

Calculations

HA Mal is mixed 1:1 volume with PEG dithiol at a molar ratio of 1:1.2 Mal:SH. Both are dissolved in Neurobasal medium in a sterile hood. PEG dithiol concentration is adjusted to equal 1.2x the molar concentration of 1% HA after additive volumes have been added and have diluted the PEG solution. The green multiplying factor is the number of reactive groups per chain (32 calculated from NMR spectra).

Example: The total hydrogel volume of 550 µl, therefore 275 µl each component.

1% Maleimide solution	0.00275 g / 242000 g/mol	=	1.13636E-08 mol	x	32	=	3.636E-07 mol / 0.000275 L	=	1.3 mM
Dithiol solution	0.002182 g / 10000 g/mol	=	2.18182E-07 mol	x	2	=	4.364E-07 mol / 0.000275 L	=	1.6 mM

1. Determine the number of hydrogels and the volume of the hydrogels to calculate the total agarose hydrogel solution volume. Plan to make enough for 2 extra hydrogels per condition.
2. Determine the concentration of cells in the hydrogel and pick a volume of concentrated cells to add to your hydrogel solution. See collagen hydrogel 1.a.
3. Calculate the volume of potential additives (Aβ, ThT, HiLyte Aβ), based on stock concentrations described in Material and Methods of Chapter 4.
    a. For a 550 µl total hydrogel volume, you would need 50 µl of stock Aβ (222 µM) to have a final concentration of 20 µM.
4. Divide the total HA hydrogel solution volume in half (275 µl), then subtract the additive volumes (275 µl - 50 µl = 215 µl). This is the volume of concentrated PEG dithiol that additives are added to.
    a. Once additives are mixed in, the PEG dithiol molar concentration should be 1.2x HA Mal molar concentration.

Methods

1. Take PEG dithiol and HA Mal out of the freezer and let them reach room temperature to avoid condensation from entering the vials and degrading the material.

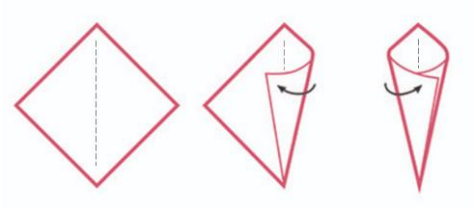

2. Weigh out PEG dithiol according to your calculations above. Collect in a 2ml microcentrifuge tube. Place on a centrifuge and "quick spin" to collect the powder to the bottom of the tube.

Figure B.2. Weigh paper cone folding for small measurements.

   a. I like to fold my weigh paper like Figure B.2., the cone shape is helpful for collecting very small amounts into a microcentrifuge tube.
   b. PEG dithiol should be stored under an inert gas such as argon.
3. Bring into sterile hood to add sterile Neurobasal medium. Vortex to dissolve.
4. PEG needs to be sterilized. Use a blunt tip needle and a 1 ml syringe to take up the PEG solution. Turn syringe so the needle is facing up and slowly pull air in until you have an air bubble enter the syringe.
5. Remove the blunt tip needle and put on an ultra-small syringe tip filter. Push the PEG solution through the filter into a new autoclaved 2 ml microcentrifuge tube.
6. To aseptically weigh HA Mal, take an autoclaved 2 ml microcentrifuge tube, close the cap and weigh the tube. Take a picture of the weight, then zero the scale.
7. In the sterile hood, take your ethanol sterilized tweezers (once dry) and gently pull off chunks of HA Mal from the sterile aliquot.
   a. Pinching the cotton-like HA Mal compacts the material and makes it more difficult to dissolve.

8. Close the cap and weigh the tube + HA Mal. Continue this process until you have more than the calculated value you need. Adjust volume calculations to keep HA Mal molar concentration at 1%.
9. Add sterile Neurobasal medium to the HA Mal. Tape the closed microcentrifuge tube to the vortexer and turn it ON to level 4 for 30 mins to 1 hr.
10. Mix together the PEG dithiol solution with the other additive solutions.
11. When ready to make the hydrogels, take the HA Mal off of the vortexer. You may need to put it on the centrifuge and "quick spin" to get rid of bubbles.
12. Pipette HA Mal with the half hydrogel volume as a droplet in each well. If the hydrogel volume is 50 μl, then pipette 25 μl HA Mal into each well.
13. Pipette PEG dithiol solution at the half hydrogel volume directly into the HA Mal droplet. GELS IN SECONDS!! You may be able to pipette up and down once or twice or you can pipette out the PEG solution and do a quick stir with the pipette tip to mix in the well.
14. For cell cultures add Neurobasal medium + 20 μM gentamicin to each well.

PEG Hydrogels

Supplies

- 4 arm PEG maleimide
- PEG dithiol
- Neurobasal medium
- 2ml Microcentrifuge tubes
- Sterile pipette tips
- Pipettors
- 1ml sterile syringe
- Blunt tip needle
- Ultra-small syringe tip filter

Calculations

4 arm PEG Mal is mixed 1:1 volume with PEG dithiol at a molar ratio of 1:1 Mal:SH. Both are dissolved in Neurobasal medium in a sterile hood. PEG dithiol concentration is adjusted to equal the molar concentration of 5% PEG Mal after additive volumes have been added and have diluted the PEG dithiol solution.

Example: The total hydrogel volume of 550 µl, therefore 275 µl each component.

5% Maleimide solution	0.01375 g / 20000 g/mol	=	6.875E-07 mol	x	4	=	2.75E-06 mol / 0.000275 L	=	10 mM
Dithiol solution	0.01375 g / 10000 g/mol	=	0.000001375 mol	x	2	=	2.75E-06 mol / 0.000275 L	=	10 mM

5. Determine the number of hydrogels and the volume of the hydrogels to calculate the total agarose hydrogel solution volume. Plan to make enough for 2 extra hydrogels per condition.

6. Determine the concentration of cells in the hydrogel and pick a volume of concentrated cells to add to your hydrogel solution. See collagen hydrogel 1.a.
7. Calculate the volume of potential additives (Aβ, ThT, HiLyte Aβ), based on stock concentrations described in Material and Methods of Chapter 4.
    a. For a 550 µl total hydrogel volume, you would need 50 µl of stock Aβ (222 µM) to have a final concentration of 20 µM.
8. Divide the total HA hydrogel solution volume in half (275 µl), then subtract the additive volumes (275 µl - 50 µl = 215 µl). This is the volume of concentrated PEG dithiol that additives are added to.
    a. Once additives are mixed in, the PEG dithiol molar concentration should be 1.2x HA Mal molar concentration.

Methods

1. Take PEG Mal and PEG dithiol out of the freezer and let them reach room temperature to avoid condensation from entering the vials and degrading the material.
2. Weigh out each PEG according to your calculations above. Collect each in a labeled 2ml microcentrifuge tube. Place on a centrifuge and "quick spin" to collect the powder to the bottom of the tube.
3. Bring into sterile hood to add sterile Neurobasal medium. Vortex to dissolve.
4. The PEG needs to be sterilized. Use a blunt tip needle and a 1 ml syringe to take up the PEG solution. Turn syringe so the needle is facing up and slowly pull air in until you have an air bubble enter the syringe.

5. Remove the blunt tip needle and put on an ultra-small syringe tip filter. Push the PEG solution through the filter into a new autoclaved 2 ml microcentrifuge tube.
6. Repeat filter sterilization for the other PEG solution.
7. Mix together the PEG dithiol solution with the other additive solutions.
8. Pipette PEG Mal with the half hydrogel volume as a droplet in each well. If the hydrogel volume is 50 µl, then pipette 25 µl PEG Mal into each well.
9. Pipette PEG dithiol solution at the half hydrogel volume directly into the PEG Mal droplet. GELS IN SECONDS!! You may be able to pipette up and down once or twice or you can pipette out the PEG dithiol solution and do a quick stir with the pipette tip to mix in the well.
10. For cell cultures add Neurobasal medium + 20 µM gentamicin to each well.

Cell viability assay

Supplies

- Calcein AM
- EthD-1
- PBS
- Pipette tips
- Pipettors
- Tinfoil

Calculations	MW	Stock (C_1)	Final (C_2)
Calcein AM	994.87 g/mol	1 mg/ml = 1.0 mM	8 μM
EthD	856.77 g/mol	1 mg/ml = 1.167 mM	18 μM

$$C_1V_1=C_2V_2$$

V_2 is the total volume needed to apply to all wells. Solve for V_1.

Methods

1. In a 96 well plate with 200 μl per well, remove 100 μl of media and apply 100 μl of live/dead assay. Calculate total volume of assay needed for your experiment.
2. Wrap plate in tinfoil to protect from the light and incubate for 30 mins.
3. Image 2D cultures first, 3D hydrogels take longer for dyes to diffuse. Image using FITC and Txs Red filters on the fluorescent microscope.
4. Using a 10x objective, take 2 images per well. There are 3 wells per condition.
5. I count cells using ImageJ cell counter and collect my data in an Excel sheet.

6. From one experiment, live & dead cells from the 3 replicate wells are added together. This total number is then used to calculate the percent viability (live /total). Percent viability from multiple experiments are used in ANOVA statistics.

TEM grid preparation

Supplies

- TEM grids
- Micropoint tweezers
- Paraffin wax paper
- TEM sticky dots
- Uranyl Acetate or Nanovan
- Water
- Pipette tips
- Filter paper

Methods

1. Cut a square of paraffin wax and stick a TEM staining dot in the center. Remove the plastic from the top of the dot to expose the adhesive.
2. With microtweezers, carefully grab a new TEM grid out of the grid box (Figure B.3. D), making sure to only grab at the thick metal edge.
3. Place the very edge of the grid to the edge of the sticky dot.
    a. The grids are made of 3 layers as shown in Figure B.3.A, a copper base with a formvar layer and a carbon layer.
    b. Sample should be put on the dark side of the grid (carbon formvar), therefore put the grid dark side up on the sticky dot.
    c. You can put the grid under UV for a few minutes to help make the grid hydrophilic and able to grab hold of particles.
4. Pipette 7 µl of sample onto the grid and incubate for 3 minutes.
5. Take a piece of cut filter paper and touch to the side of the grid. Do not touch the surface of the grid, you don't want to disturb the sample.

6. Pipette 30 µl droplets of water and uranyl acetate (or Nanovan) next to each other on the paraffin paper (Figure B.3.C). Have a piece of filter paper on the lab bench.
    a. Uranyl acetate is a typical heavy metal TEM stain, however, if you are using gold nanoparticles which are the same density as uranyl acetate, you need a lighter stain such as Nanovan (kept at 4°C).
7. With the microtweezers, grab the thicker outer rim next to the sticky dot and pull the grid off the dot.
8. Place the grid sample side down (dark side) onto the water droplet.
9. Immediately touch the side of the grid to filter paper to wick away the water.
10. Place the grid sample side down (dark side) on to the heavy metal stain. Incubate for 3 mins then wick away with filter paper.
11. Let the grids dry in an empty TEM grid box with the lid open. You can cover the box with a petri dish to prevent dust from contaminating the grid.

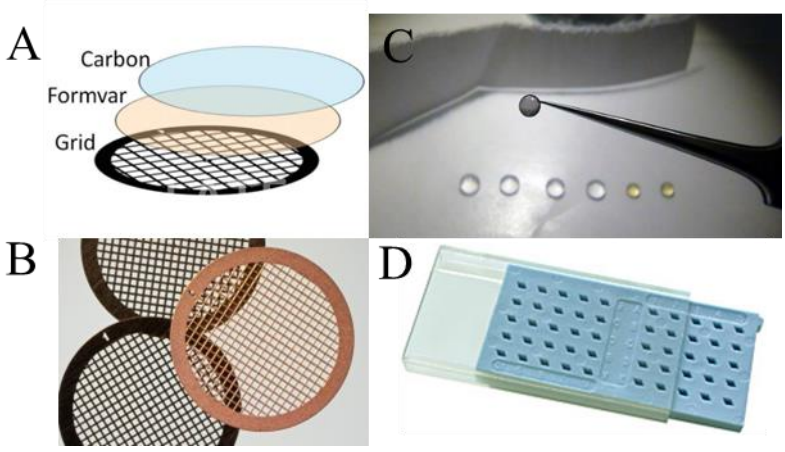

Figure B.3. TEM grid protocol materials. The layers of the grid are a copper base, with a formvar and carbon layer (A) where the light side is the copper grid and dark side is the formvar/carbon (B). Droplet method where you place the grid on droplets of solution (C). A TEM grid box holds grids on their side so you can grab them easily (D).

FCS set up

Supplies

- Secure-Seal Hybridization Chamber Gasket, 8 chambers, 0.8 mm depth (GraceBioLabs)

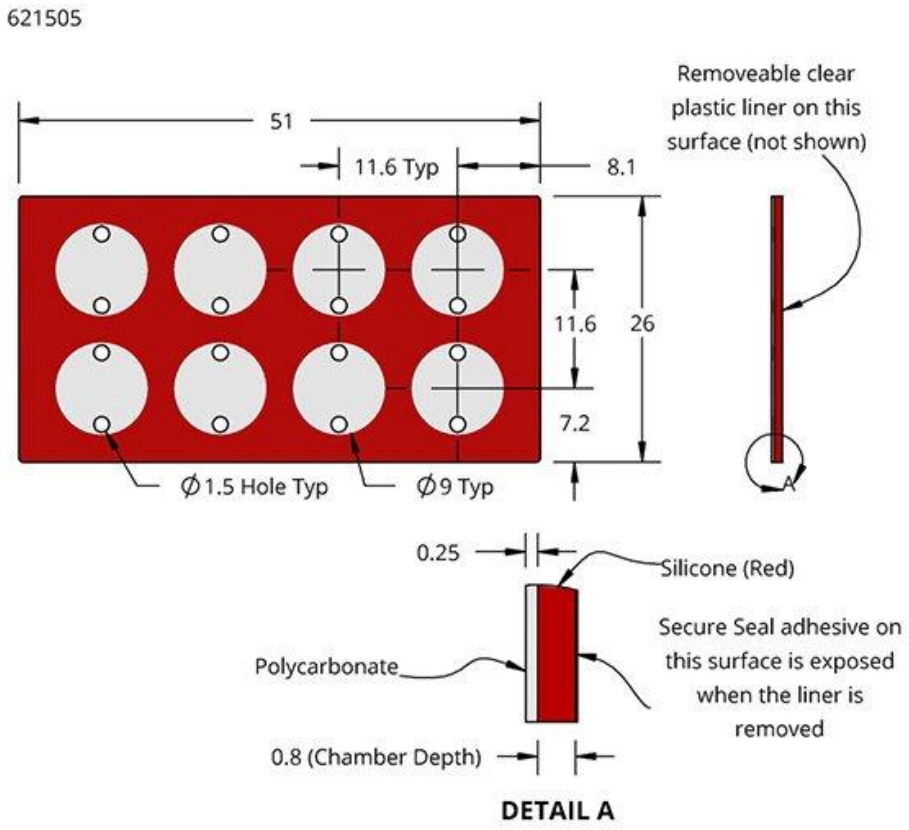

SecureSeal adhesive dots	2x HiLyte 488 Aβ
#2 borosilicate cover glass	FAM Scr Aβ
Knife	Neurobasal medium
2x Aβ aliquot	Microscope slide box
Scr Aβ	

*All hydrogel material – see hydrogel protocol for materials needed

Methods

1. Cut the hybridization chamber down the middle making 2 squares of 4 chambers. Be careful not to cut into a chamber. Use good scissors.
    a. The microscope stage slide holder blocks the corner wells if all 8 wells were on a single slide. The squares of 4 make all wells accessible.
2. Lay a cover glass on a kim wipe on the lab bench. Peel off the plastic liner to expose the adhesive on the hybridization chamber. Stick the hybridization chamber onto the cover glass carefully to be sure all the chamber wells are sealed.
    a. Make as many sample slides as needed. I typically make 4: hydrogel @ UMBC, hydrogel @ DSU, Solutions, and hydrogel Scr Aβ.

Note My drive to Dr. Boukari's lab at DSU is about 1hr 45min, therefore I make a set of samples at UMBC then a second set of samples at DSU to get immediate time points and late time points.

3. Reference hydrogel protocols and Aβ preparation protocol to prepare samples with 20 μM Aβ + 250 nM HiLyte Aβ.
4. Fill the chamber wells by holding the slide at a slight angle and pipette the solution into the bottom port. The 0.8 mm depth wells hold ~60 μl.
5. The HA and PEG hydrogels must be polymerized inside the chamber wells. Add the maleimide sample to the bottom port first.

6. Then with a new pipette tip, pipette the SH/Aβ solution into the bottom port. To mix, do not fully expel the SH/Aβ solution, but pipette back up to take in some maleimide solution before fully expelling the solution into the well.
    a. Do not overfill the chamber wells, the solution should not bulge out of the ports. You do not want your solution to touch the adhesive dots.
7. I use a pocket knife to cut the SecureSeal adhesive dots into fourths. Using pointed tweezers (or microtweezers), pick up a fourth and place it over the open ports. Try to place them in a way the entire well is not covered.
8. Write down the time the samples were made, this starts the aggregation clock.
9. Store sample slides in the slide box to protect from light.

DSU FCS Instrument

The FCS instrument setup is described in the Materials and Methods of Chapters 3 and 4.

1. Turn on boxes in order starting at 1.
2. In the VistaVision software select FFS acquisition.
3. Set acquisition time to 300s.
4. Place a drop of oil on the oil objective then place the sample slide on the stage.
5. I like to open the shutter so I can see the laser position on my sample. Position the stage so that the laser is in the bulk of the sample chamber well.
6. Begin raising the objective to make contact with the oil. I look at the sample and look for the contact. You can see a circle of liquid and the laser looks brighter.

7. Now cover the sample with a blackout sheet to block out light.
8. Watch the CPS monitor for Ch1 and Ch2 (this tells you the photon counts being detected) as you raise the objective slowly toward your sample. Out of your sample the photon count should be in the hundreds.
9. The first spike in photon counts is the outside layer of the cover glass.
10. Continue raising the objective until the second spike in photon counts, this is the laser leaving the cover glass into the sample.
11. At the cover glass surface molecules have settled, so although the photon counts are the highest, the molecules are not moving and therefore will not have a correlation function.
12. Move the objective a little deeper into the sample, photon counts ~20,000 is good.
    a. Watch the CPS monitor for 30s to see if the photon counts are dropping. If they are then the laser power should be turned down a little to minimize photo bleaching.
13. Close the shutter and click Start to begin acquiring data. Watch the photon counts graph, the line should be consistent with occasional spikes where large species are detected.
    a. There should not be a steady drop, a steady fluctuation, or massive increase as these will distort the correlation function curve.
    b. When finished, look at the cross-correlation function curve. The left side corresponds to fast species and the right side to slow species. The left side will have more spread in the data, but look for a smooth curve tapering to the right.
14. Save the data and write down the time since the sample was made.

15. Start the acquisition a second time to get a replicate data set and save.
16. To move to the next sample, lower the objective until the oil has detached, then move the stage to the next sample. Repeat steps 5 – 14 with this sample and the remaining samples.
17. The oil should be replaced ever 2 samples. When changing sample slides, clean the oil off of the objective with objective paper and cleaner. Then oil the objective and continue.
18. Once all samples have been tested once, I run through the samples in the same order a second time making note of the time point for every sample run.
19. When finished, save the files to a flash drive.
20. Clean the objective and turn off the instrument boxes in reverse order.
21. VistaVision 3D Triplet Gaussian 2 Species model data analysis explained in Materials and Methods of Chapters 3 and 4. Analysis is of the cross correlation, not the single channels.

References

1. Fleming, T. C.; Shin, J. Y.; Lee, S. H.; Becker, E.; Huang, K. C.; Bustamante, C.; Pogliano, K., Dynamic SpoIIIE assembly mediates septal membrane fission during Bacillus subtilis sporulation. *Genes Dev* **2010,** *24* (11), 1160-72.
2. Beyreuther, K.; Masters, C. L., Amyloid precursor protein (APP) and beta A4 amyloid in the etiology of Alzheimer's disease: precursor-product relationships in the derangement of neuronal function. *Brain Pathol.* **1991,** *1* (4), 241-51.
3. Selkoe, D. J., The molecular pathology of Alzheimer's disease. *Neuron* **1991,** *6* (4), 487-98.
4. Hardy, J.; Allsop, D., Amyloid deposition as the central event in the aetiology of Alzheimer's disease. *Trends Pharmacol Sci.* **1991,** *12* (10), 383-8.
5. Giuffrida, M. L.; Caraci, F.; Pignataro, B.; Cataldo, S.; De Bona, P.; Bruno, V.; Molinaro, G.; Pappalardo, G.; Messina, A.; Palmigiano, A.; Garozzo, D.; Nicoletti, F.; Rizzarelli, E.; Copani, A., Beta-amyloid monomers are neuroprotective. *J Neurosci* **2009,** *29* (34), 10582-7.
6. Selkoe, D. J.; Hardy, J., The amyloid hypothesis of Alzheimer's disease at 25 years. *EMBO Mol Med* **2016,** *8* (6), 595-608.
7. Hortschansky, P.; Schroeckh, V.; Christopeit, T.; Zandomeneghi, G.; Fandrich, M., The aggregation kinetics of Alzheimer's beta-amyloid peptide is controlled by stochastic nucleation. *Protein Sci* **2005,** *14* (7), 1753-9.

8. Cruz, L.; Urbanc, B.; Borreguero, J. M.; Lazo, N. D.; Teplow, D. B.; Stanley, H. E., Solvent and mutation effects on the nucleation of amyloid beta-protein folding. *Proc Natl Acad Sci U S A* **2005,** *102* (51), 18258-63.

9. Luhrs, T.; Ritter, C.; Adrian, M.; Riek-Loher, D.; Bohrmann, B.; Dobeli, H.; Schubert, D.; Riek, R., 3D structure of Alzheimer's amyloid-beta(1-42) fibrils. *Proc Natl Acad Sci U S A* **2005,** *102* (48), 17342-7.

10. Lee, S.; Fernandez, E. J.; Good, T. A., Role of aggregation conditions in structure, stability, and toxicity of intermediates in the Abeta fibril formation pathway. *Protein Sci* **2007,** *16* (4), 723-32.

11. Ahmed, M.; Davis, J.; Aucoin, D.; Sato, T.; Ahuja, S.; Aimoto, S.; Elliott, J. I.; Van Nostrand, W. E.; Smith, S. O., Structural conversion of neurotoxic amyloid-beta(1-42) oligomers to fibrils. *Nat Struct Mol Biol* **2010,** *17* (5), 561-7.

12. Keshet, B.; Gray, J. J.; Good, T. A., Structurally distinct toxicity inhibitors bind at common loci on beta-amyloid fibril. *Protein Sci* **2010,** *19* (12), 2291-304.

13. Drummond, E.; Wisniewski, T., Alzheimer's disease: experimental models and reality. *Acta Neuropathol* **2017,** *133* (2), 155-175.

14. Srivastava, A.; Balaji, P. V., Size, orientation and organization of oligomers that nucleate amyloid fibrils: clues from MD simulations of pre-formed aggregates. *Biochim Biophys Acta* **2012,** *1824* (8), 963-73.

15. Luhrs, T.; Ritter, C.; Adrian, M.; Riek-Loher, D.; Bohrmann, B.; Dobeli, H.; Schubert, D.; Riek, R., 3D structure of Alzheimer's amyloid-beta(1-42) fibrils. *Proc Natl Acad Sci U.S.A.* **2005,** *102* (48), 17342-7.

16. Khan, F.; Tanaka, M., Designing Smart Biomaterials for Tissue Engineering. *Int J Mol Sci* **2017,** *19* (1).

17. Long, G., The Biopharmaceutical Pipeline: Innovative Therapies in Clinical Development. Analysis Group, I., Ed. PhRMA: 2017.

18. Doody, R. S.; Raman, R.; Farlow, M.; Iwatsubo, T.; Vellas, B.; Joffe, S.; Kieburtz, K.; He, F.; Sun, X.; Thomas, R. G.; Aisen, P. S.; Alzheimer's Disease Cooperative Study Steering, C.; Siemers, E.; Sethuraman, G.; Mohs, R.; Semagacestat Study, G., A phase 3 trial of semagacestat for treatment of Alzheimer's disease. *N Engl J Med* **2013,** *369* (4), 341-50.

19. King, A., The search for better animal models of Alzheimer's disease. *Nature* **2018,** *559* (7715), S13-S15.

20. Cummings, J. L.; Morstorf, T.; Zhong, K., Alzheimer's disease drug-development pipeline: few candidates, frequent failures. *Alzheimers Res Ther* **2014,** *6* (4), 37.

21. Marieb, E. N.; Hoehn, K., *Human Anatomy & Physiology (11th Edition)*. Pearson: 2018.

22. Place, E. S.; Evans, N. D.; Stevens, M. M., Complexity in biomaterials for tissue engineering. *Nat Mater* **2009,** *8* (6), 457-70.

23. Edgar, L.; McNamara, K.; Wong, T.; Tamburrini, R.; Katari, R.; Orlando, G., Heterogeneity of Scaffold Biomaterials in Tissue Engineering. *Materials (Basel)* **2016,** *9* (5).

24. Balasubramanian, S.; Packard, J. A.; Leach, J. B.; Powell, E. M., Three-Dimensional Environment Sustains Morphological Heterogeneity and Promotes

Phenotypic Progression During Astrocyte Development. *Tissue Eng Part A* **2016,** *22* (11-12), 885-98.

25. Ribeiro, A.; Vargo, S.; Powell, E. M.; Leach, J. B., Substrate three-dimensionality induces elemental morphological transformation of sensory neurons on a physiologic timescale. *Tissue Eng Part A* **2012,** *18* (1-2), 93-102.
26. Mirbagheri, M.; Adibnia, V.; Hughes, B. R.; Waldman, S. D.; Banquy, X.; Hwang, D. K., Advanced cell culture platforms: a growing quest for emulating natural tissues. *Mater Horiz* **2019,** *6* (1), 45-71.
27. Rianna, C.; Kumar, P.; Radmacher, M., The role of the microenvironment in the biophysics of cancer. *Semin Cell Dev Biol* **2017**.
28. Duarte Campos, D. F.; Bonnin Marquez, A.; O'Seanain, C.; Fischer, H.; Blaeser, A.; Vogt, M.; Corallo, D.; Aveic, S., Exploring Cancer Cell Behavior In Vitro in Three-Dimensional Multicellular Bioprintable Collagen-Based Hydrogels. *Cancers (Basel)* **2019,** *11* (2).
29. Ahn, J.; Ahn, J. H.; Yoon, S.; Nam, Y. S.; Son, M. Y.; Oh, J. H., Human three-dimensional in vitro model of hepatic zonation to predict zonal hepatotoxicity. *J Biol Eng* **2019,** *13*, 22.
30. Ellis, R. J., Macromolecular crowding: an important but neglected aspect of the intracellular environment. *Curr. Opin. Struct. Biol.* **2001,** *11* (1), 114-119.
31. Ellis, R. J., Macromolecular crowding: obvious but underappreciated. *Trends Biochem. Sci.* **2001,** *26* (10), 597-604.
32. Kuznetsova, I. M.; Turoverov, K. K.; Uversky, V. N., What macromolecular crowding can do to a protein. *Int J Mol Sci* **2014,** *15* (12), 23090-140.

33. Zhou, Z.; Fan, J. B.; Zhu, H. L.; Shewmaker, F.; Yan, X.; Chen, X.; Chen, J.; Xiao, G. F.; Guo, L.; Liang, Y., Crowded cell-like environment accelerates the nucleation step of amyloidogenic protein misfolding. *J Biol Chem* **2009,** *284* (44), 30148-58.

34. Luo, X. D.; Kong, F. L.; Dang, H. B.; Chen, J.; Liang, Y., Macromolecular crowding favors the fibrillization of beta2-microglobulin by accelerating the nucleation step and inhibiting fibril disassembly. *Biochim Biophys Acta* **2016,** *1864* (11), 1609-19.

35. Kendrew, J. C., Structure and function in myoglobin and other proteins. *Fed Proc* **1959,** *18* (2, Part 1), 740-51.

36. Burr, M.; Koshland, D. E., Use of "Reporter Groups" in Structure-Function Studies of Proteins. *Proc Natl Acad Sci U.S.A.* **1964,** *52* (4), 1017-1024.

37. McLachlan, A. D., Protein Structure and Function. *Annu. Rev. Phys. Chem.* **1972,** *23* (1), 165-192.

38. Olesen, H. A., Protein structure and function. *Nord Med* **1970,** *84* (47), 1481-7.

39. Orengo, C. A.; Pearl, F. M.; Bray, J. E.; Todd, A. E.; Martin, A. C.; Lo Conte, L.; Thornton, J. M., The CATH Database provides insights into protein structure/function relationships. *Nucleic Acids Res.* **1999,** *27* (1), 275-9.

40. Guerrucci, M. A.; Belle, R., Characterisation of protein structure/function relationship by sequence analysis without previous alignment: distinction between sub-groups of protein kinases. *Biosci Rep* **1995,** *15* (3), 161-71.

41. Sandberg, W. S.; Schlunk, P. M.; Zabin, H. B.; Terwilliger, T. C., Relationship between in Vivo Activity and in Vitro Measures of Function and Stability of a Protein. *Biochemistry* **2002,** *34* (37), 11970-11978.

42. Jez, J. M., Revisiting protein structure, function, and evolution in the genomic era. *J Invertebr Pathol* **2017,** *142*, 11-15.

43. Zheng, M.; Zhao, J.; Cui, C.; Fu, Z.; Li, X.; Liu, X.; Ding, X.; Tan, X.; Li, F.; Luo, X.; Chen, K.; Jiang, H., Computational chemical biology and drug design: Facilitating protein structure, function, and modulation studies. *Med Res Rev* **2018,** *38* (3), 914-950.

44. Dunker, A. K.; Lawson, J. D.; Brown, C. J.; Williams, R. M.; Romero, P.; Oh, J. S.; Oldfield, C. J.; Campen, A. M.; Ratliff, C. M.; Hipps, K. W.; Ausio, J.; Nissen, M. S.; Reeves, R.; Kang, C.; Kissinger, C. R.; Bailey, R. W.; Griswold, M. D.; Chiu, W.; Garner, E. C.; Obradovic, Z., Intrinsically disordered protein. *J Mol Graph Model* **2001,** *19* (1), 26-59.

45. Bragg, W. H., X-Rays and Crystalline Structure. *Science* **1914,** *40* (1040), 795-802.

46. Marton, L., Electron Microscopy of Biological Objects. *Nature* **1934,** *133* (3372), 911-911.

47. Darrow, K. K., Magnetic Resonance. *Bell Syst. Tech. J* **1953,** *32* (1), 74-99.

48. Ovenall, D. W.; Peaker, F. W., A light scattering instrument for molecular weight measurments. *Makromolekulare Chemie* **1959,** *33* (1), 222-236.

49. Dobson, C. M., The structural basis of protein folding and its links with human disease. *Philos Trans R Soc Lond B Biol Sci* **2001,** *356* (1406), 133-45.

50. Ami, D.; Natalello, A.; Lotti, M.; Doglia, S. M., Why and how protein aggregation has to be studied in vivo. *Microb Cell Fact* **2013,** *12*, 17.

51. Wolynes, P.; Onuchic, J.; Thirumalai, D., Navigating the folding routes. *Science* **1995,** *267* (5204), 1619-1620.

52. Bernal, J. D.; Finney, J. L., Geometry of Random Packing of Hard Spheres. *Discuss Faraday Soc* **1967,** *43*, 62-69.

53. Dill, K. A., Theory for the folding and stability of globular proteins. *Biochemistry* **1985,** *24* (6), 1501-9.

54. Dill, K. A.; Alonso, D. O.; Hutchinson, K., Thermal stabilities of globular proteins. *Biochemistry* **1989,** *28* (13), 5439-49.

55. Stigter, D.; Dill, K. A., Free Energy of Electrical Double Layers: Entropy of Adsorbed Ions and the Binding Polynomial. *J. Phys. Chem.* **1989,** *93* (18), 6737-6743.

56. Chan, H. S.; Dill, K. A., Origins of structure in globular proteins. *Proc. Natl. Acad. Sci. U.S.A.* **1990,** *87* (16), 6388-92.

57. Wolynes, P. G.; Onuchic, J. N.; Thirumalai, D., Navigating the folding routes. *Science* **1995,** *267* (5204), 1619-20.

58. Fields, G. B.; Alonso, D. O. V.; Stigter, D.; Dill, K. A., Theory for the Aggregation of Proteins and Copolymers. *J. Phys. Chem.* **1992,** *96* (10), 3974-3981.

59. Hansen, S.; Müller, J. J., The Maximum-Entropy Method in Small-Angle Scattering. **1996**, 69-78.

60. Fink, A. L., Protein aggregation: folding aggregates, inclusion bodies and amyloid. *Folding and Design* **1998,** *3* (1), R9-R23.

61. Nyeo, S. L.; Chu, B., Maximum-entropy analysis of photon correlation spectroscopy data. *Macromolecules* **1989,** *22* (10), 3998-4009.

62. Zimmerman, S. B.; Minton, A. P., Macromolecular crowding: biochemical, biophysical, and physiological consequences. *Annu Rev Biophys Biomol Struct* **1993,** *22*, 27-65.

63. Cebecauer, M.; Spitaler, M.; Serge, A.; Magee, A. I., Signalling complexes and clusters: functional advantages and methodological hurdles. *J Cell Sci* **2010,** *123* (Pt 3), 309-20.

64. Smith, F. D.; Scott, J. D., Signaling Complexes: Junctions on the Intracellular Information Super Highway. *Curr. Biol.* **2002,** *12* (1), R32-R40.

65. Pliss, A.; Levchenko, S. M.; Liu, L.; Peng, X.; Ohulchanskyy, T. Y.; Roy, I.; Kuzmin, A. N.; Qu, J.; Prasad, P. N., Cycles of protein condensation and discharge in nuclear organelles studied by fluorescence lifetime imaging. *Nat Commun* **2019,** *10* (1), 455.

66. Frantz, C.; Stewart, K. M.; Weaver, V. M., The extracellular matrix at a glance. *J Cell Sci* **2010,** *123* (Pt 24), 4195-200.

67. Cohen, S. S., The isolation and crystallization of plant viruses and other protein macro molecules by means of hydrophilic colloids. *J. Biol. Chem.* **1942,** *144*, 353-362.

68. Juckles, I. R. M., Fractionation of proteins and viruses with polyethylene glycol. *Biochim Biophys Acta Protein Structure* **1971,** *229* (3), 535-546.

69. Laurent, T. C., The Interaction between Polysaccharides and Other Macromolecules. 5. The Solubility of Proteins in the Presence of Dextran. *Biochem J* **1963,** *89* (2), 253-257.

70. Cheung, M. S.; Klimov, D.; Thirumalai, D., Molecular crowding enhances native state stability and refolding rates of globular proteins. *Proc. Natl. Acad. Sci. U.S.A.* **2005,** *102* (13), 4753-8.

71. Hall, D.; Minton, A. P., Macromolecular crowding: qualitative and semiquantitative successes, quantitative challenges. *Biochim Biophys Acta Proteins Proteom* **2003,** *1649* (2), 127-139.

72. Comper, W. D.; Laurent, T. C., An estimate of the enthalpic contribution to the interaction between dextran and albumin. *Biochemistry* **1978,** *175* (2), 703-708.

73. Edmond, E.; Ogston, A. G., An approach to the study of phase separation in ternary aqueous systems. *Biochem J* **1968,** *109* (4), 569-76.

74. Laurent, T. C.; Ogston, A. G., The interaction between polysaccharides and other macromolecules. 4. The osmotic pressure of mixtures of serum albumin and hyaluronic acid. *Biochem J* **1963,** *89*, 249-53.

75. Minton, A. P., Thermodynamic nonideality and the dependence of partition coefficient upon solute concentration in exclusion chromatography. Application to self-associating and non-self-associating solutes. Application to hemoglobin. *Biophys Chem* **1980,** *12* (3-4), 271-7.

76. Minton, A. P., Excluded volume as a determinant of macromolecular structure and reactivity. *Biopolymers* **1981,** *20* (10), 2093-2120.

77. Minton, A. P., The effect of volume occupancy upon the thermodynamic activity of proteins: some biochemical consequences. *Mol Cell Biochem* **1983,** *55* (2), 119-40.

78. Rivas, G.; Fernandez, J. A.; Minton, A. P., Direct observation of the self-association of dilute proteins in the presence of inert macromolecules at high concentration via tracer sedimentation equilibrium: theory, experiment, and biological significance. *Biochemistry* **1999,** *38* (29), 9379-88.

79. Batra, J.; Xu, K.; Qin, S.; Zhou, H. X., Effect of macromolecular crowding on protein binding stability: modest stabilization and significant biological consequences. *Biophys J* **2009,** *97* (3), 906-11.

80. Minton, A. P., Implications of macromolecular crowding for protein assembly. *Curr Opin Struct Biol* **2000,** *10* (1), 34-9.

81. Sipe, J. D.; Benson, M. D.; Buxbaum, J. N.; Ikeda, S. I.; Merlini, G.; Saraiva, M. J.; Westermark, P., Amyloid fibril proteins and amyloidosis: chemical identification and clinical classification International Society of Amyloidosis 2016 Nomenclature Guidelines. *Amyloid* **2016,** *23* (4), 209-213.

82. Chiti, F.; Dobson, C. M., Protein Misfolding, Amyloid Formation, and Human Disease: A Summary of Progress Over the Last Decade. *Annu Rev Biochem* **2017,** *86*, 27-68.

83. Van den Berg, B.; Ellis, R. J.; Dobson, C. M., Effects of macromolecular crowding on protein folding and aggregation. *EMBO J* **1999,** *18* (24), 6927-33.

84. Hatters, D. M.; Minton, A. P.; Howlett, G. J., Macromolecular crowding accelerates amyloid formation by human apolipoprotein C-II. *J Biol Chem* **2002,** *277* (10), 7824-30.

85. Munishkina, L. A.; Cooper, E. M.; Uversky, V. N.; Fink, A. L., The effect of macromolecular crowding on protein aggregation and amyloid fibril formation. *J Mol Recognit* **2004,** *17* (5), 456-64.

86. Bokvist, M.; Grobner, G., Misfolding of amyloidogenic proteins at membrane surfaces: the impact of macromolecular crowding. *J Am Chem Soc* **2007,** *129* (48), 14848-9.

87. Borrero, E. E.; Escobedo, F. A., Folding kinetics of a lattice protein via a forward flux sampling approach. *J Chem Phys* **2006,** *125* (16), 164904.

88. Banks, A.; Qin, S.; Weiss, K. L.; Stanley, C. B.; Zhou, H. X., Intrinsically Disordered Protein Exhibits Both Compaction and Expansion under Macromolecular Crowding. *Biophys J* **2018,** *114* (5), 1067-1079.

89. Shin, Y.; Brangwynne, C. P., Liquid phase condensation in cell physiology and disease. *Science* **2017,** *357* (6357).

90. Uversky, V. N., The multifaceted roles of intrinsic disorder in protein complexes. *FEBS Lett* **2015,** *589* (19 Pt A), 2498-506.

91. Qin, S.; Zhou, H. X., Effects of Macromolecular Crowding on the Conformational Ensembles of Disordered Proteins. *J Phys Chem Lett* **2013,** *4* (20).

92. Goldenberg, D. P.; Argyle, B., Minimal effects of macromolecular crowding on an intrinsically disordered protein: a small-angle neutron scattering study. *Biophys J* **2014,** *106* (4), 905-14.

93. Miller, C. M.; Kim, Y. C.; Mittal, J., Protein Composition Determines the Effect of Crowding on the Properties of Disordered Proteins. *Biophys J* **2016,** *111* (1), 28-37.

94. Nguemaha, V.; Qin, S.; Zhou, H. X., Atomistic Modeling of Intrinsically Disordered Proteins Under Polyethylene Glycol Crowding: Quantitative Comparison with Experimental Data and Implication of Protein-Crowder Attraction. *J Phys Chem B* **2018**.

95. Minton, A. P., Confinement as a determinant of macromolecular structure and reactivity. *Biophys J* **1992,** *63* (4), 1090-100.

96. Minton, A. P., Models for excluded volume interaction between an unfolded protein and rigid macromolecular cosolutes: macromolecular crowding and protein stability revisited. *Biophys J* **2005,** *88* (2), 971-85.

97. Eggers, D. K.; Valentine, J. S., Molecular confinement influences protein structure and enhances thermal protein stability. *Protein Sci* **2001,** *10* (2), 250-61.

98. Wang, W.; Xu, W. X.; Levy, Y.; Trizac, E.; Wolynes, P. G., Confinement effects on the kinetics and thermodynamics of protein dimerization. *Proc. Natl. Acad. Sci. U.S.A.* **2009,** *106* (14), 5517-22.

99. Mittal, J.; Best, R. B., Thermodynamics and kinetics of protein folding under confinement. *Proc. Natl. Acad. Sci. U.S.A.* **2008,** *105* (51), 20233-8.

100. Rathore, N.; Knotts, T. A. t.; de Pablo, J. J., Confinement effects on the thermodynamics of protein folding: Monte Carlo simulations. *Biophys J* **2006,** *90* (5), 1767-73.

101. Bolis, D.; Politou, A. S.; Kelly, G.; Pastore, A.; Andrea Temussi, P., Protein Stability in Nanocages: A Novel Approach for Influencing Protein Stability by Molecular Confinement. *J Mol Biol* **2004,** *336* (1), 203-212.

102. Mastro, A. M.; Babich, M. A.; Taylor, W. D.; Keith, A. D., Diffusion of a small molecule in the cytoplasm of mammalian cells. *Proc. Natl. Acad. Sci. U.S.A.* **1984,** *81* (11), 3414-8.

103. Zhou, H. X., Protein folding and binding in confined spaces and in crowded solutions. *J Mol Recognit* **2004,** *17* (5), 368-75.

104. Ping, G.; Yuan, J. M.; Sun, Z.; Wei, Y., Studies of effects of macromolecular crowding and confinement on protein folding and protein stability. *J Mol Recognit* **2004,** *17* (5), 433-40.

105. Zhou, H. X., Protein folding in confined and crowded environments. *Arch Biochem Biophys* **2008,** *469* (1), 76-82.

106. Cheng, K.; Wu, Q.; Zhang, Z.; Pielak, G. J.; Liu, M.; Li, C., Crowding and Confinement Can Oppositely Affect Protein Stability. *ChemPhysChem* **2018,** *19* (24), 3350-3355.

107. Long, S.; Kunkel, J.; Asuri, P., Influence of Macromolecular Crowding and Confinement on Enzyme Activity and Structure under Native and Denaturing Conditions. *Biochem. Anal. Biochem.* **2017,** *07* (02).

108. Wei, M. T.; Elbaum-Garfinkle, S.; Holehouse, A. S.; Chen, C. C.; Feric, M.; Arnold, C. B.; Priestley, R. D.; Pappu, R. V.; Brangwynne, C. P., Phase behaviour of disordered proteins underlying low density and high permeability of liquid organelles. *Nat Chem* **2017,** *9* (11), 1118-1125.

109. Fisher, S. A.; Anandakumaran, P. N.; Owen, S. C.; Shoichet, M. S., Tuning the Microenvironment: Click-Crosslinked Hyaluronic Acid-Based Hydrogels Provide a Platform for Studying Breast Cancer Cell Invasion. *Advanced Functional Materials* **2015,** *25* (46), 7163-7172.

110. Choi, S. H.; Kim, Y. H.; Hebisch, M.; Sliwinski, C.; Lee, S.; D'Avanzo, C.; Chen, H.; Hooli, B.; Asselin, C.; Muffat, J.; Klee, J. B.; Zhang, C.; Wainger, B. J.; Peitz, M.; Kovacs, D. M.; Woolf, C. J.; Wagner, S. L.; Tanzi, R. E.; Kim, D. Y., A three-dimensional human neural cell culture model of Alzheimer's disease. *Nature* **2014,** *515* (7526), 274-8.

111. Aljohani, W.; Ullah, M. W.; Zhang, X.; Yang, G., Bioprinting and its applications in tissue engineering and regenerative medicine. *Int J Biol Macromol* **2018,** *107* (Pt A), 261-275.

112. Wieland, J. A.; Houchin-Ray, T. L.; Shea, L. D., Non-viral vector delivery from PEG-hyaluronic acid hydrogels. *J Control Release* **2007,** *120* (3), 233-41.

113. Xu, X.; Jha, A. K.; Harrington, D. A.; Farach-Carson, M. C.; Jia, X., Hyaluronic Acid-Based Hydrogels: from a Natural Polysaccharide to Complex Networks. *Soft Matter* **2012,** *8* (12), 3280-3294.

114. Stratakis, E., Novel Biomaterials for Tissue Engineering 2018. *Int J Mol Sci* **2018,** *19* (12).

115. Ruedinger, F.; Lavrentieva, A.; Blume, C.; Pepelanova, I.; Scheper, T., Hydrogels for 3D mammalian cell culture: a starting guide for laboratory practice. *Appl Microbiol Biotechnol* **2015,** *99* (2), 623-36.

116. Khan, R.; Mahendhiran, B.; Aroulmoji, V., Chemistry of hyaluronic acid and its significance in drug delivery strategies: A review. *Int J Pharm Sci Res* **2013,** *4* (9), 3699-3710.

117. Wu, J.; Wang, Z.; Lin, W.; Chen, S., Investigation of the interaction between poly(ethylene glycol) and protein molecules using low field nuclear magnetic resonance. *Acta Biomater.* **2013,** *9* (5), 6414-20.

118. Gregoritza, M.; Brandl, F. P., The Diels-Alder reaction: A powerful tool for the design of drug delivery systems and biomaterials. *Eur J Pharm Biopharm* **2015,** *97* (Pt B), 438-53.

119. Leach, J. B.; Bivens, K. A.; Patrick, C. W., Jr.; Schmidt, C. E., Photocrosslinked hyaluronic acid hydrogels: natural, biodegradable tissue engineering scaffolds. *Biotechnol Bioeng* **2003,** *82* (5), 578-89.

120. Lutolf, M. P.; Tirelli, N.; Cerritelli, S.; Cavalli, L.; Hubbell, J. A., Systematic Modulation of Michael-Type Reactivity of Thiols through the Use of Charged Amino Acids. *Bioconjug. Chem.* **2001,** *12* (6), 1051-1056.

121. Jin, R.; Dijkstra, P. J.; Feijen, J., Rapid gelation of injectable hydrogels based on hyaluronic acid and poly(ethylene glycol) via Michael-type addition. *J Control Release* **2010,** *148* (1), e41-3.

122. Place, E. S.; George, J. H.; Williams, C. K.; Stevens, M. M., Synthetic polymer scaffolds for tissue engineering. *Chem Soc Rev* **2009,** *38* (4), 1139-51.

123. Tong, Z.; Solanki, A.; Hamilos, A.; Levy, O.; Wen, K.; Yin, X.; Karp, J. M., Application of biomaterials to advance induced pluripotent stem cell research and therapy. *EMBO J* **2015,** *34* (8), 987-1008.

124. Abuelfilat, A. Y.; Kim, Y.; Miller, P.; Hoo, S. P.; Li, J.; Chan, P.; Fu, J., Bridging structure and mechanics of three-dimensional porous hydrogel with X-ray ultramicroscopy and atomic force microscopy. *RSC Advances* **2015,** *5* (78), 63909-63916.

125. Creasey, R.; Sharma, S.; Craig, J. E.; Gibson, C. T.; Ebner, A.; Hinterdorfer, P.; Voelcker, N. H., Detecting protein aggregates on untreated human tissue samples by atomic force microscopy recognition imaging. *Biophys J* **2010,** *99* (5), 1660-7.

126. Narayanan, J.; Xiong, J.-Y.; Liu, X.-Y., Determination of agarose gel pore size: Absorbance measurements vis a vis other techniques. *J Phys Conf Ser* **2006,** *28*, 83-86.

127. Bohidar, H. B., Dynamics in thermoreversible polymer gels. *Curr. Sci.* **2001,** *80* (8), 1008-17.

128. Pusey, P. N.; Van Megen, W., Dynamic light scattering by non-ergodic media. *PHYSICA A.* **1989,** *157* (2), 705-741.

129. Burne, P. M.; Sellen, D. B., A laser light scattering study of gellan gels. *Biopolymers* **1994,** *34* (3), 371-382.

130. Johnson, E. M.; Berk, D. A.; Jain, R. K.; Deen, W. M., Diffusion and partitioning of proteins in charged agarose gels. *Biophys J* **1995,** *68* (4), 1561-1568.

131. Pluen, A.; Netti, P. A.; Jain, R. K.; Berk, D. A., Diffusion of Macromolecules in Agarose Gels: Comparison of Linear and Globular Configurations. *Biophys J* **1999,** *77* (1), 542-552.

132. Canal, T.; Peppas, N. A., Correlation between mesh size and equilibrium degree of swelling of polymeric networks. *J. Biomed. Mater. Res.* **1989,** *23* (10), 1183-93.

133. Barretta, P.; Bordi, F.; Rinaldi, C.; Paradossi, G., A Dynamic Light Scattering Study of Hydrogels Based on Telechelic Poly(vinyl alcohol). *The Journal of Physical Chemistry B* **2000,** *104* (47), 11019-11026.

134. Amin, S.; Barnett, G. V.; Pathak, J. A.; Roberts, C. J.; Sarangapani, P. S., Protein aggregation, particle formation, characterization & rheology. *Curr. Opin. Colloid Interface Sci.* **2014,** *19* (5), 438-449.

135. Wozniak, M. A.; Keely, P. J., Use of three-dimensional collagen gels to study mechanotransduction in T47D breast epithelial cells. *Biol Proced Online* **2005,** *7*, 144-61.

136. Demeule, B.; Messick, S.; Shire, S. J.; Liu, J., Characterization of particles in protein solutions: reaching the limits of current technologies. *AAPS J* **2010,** *12* (4), 708-15.

137. V., C.-R. R., Aggregates in MAbs and Recombinant Therapeutic Proteins: A Regulatory Perspective. *BioPharm Int.* **2008,** *21* (11).

138. Siew, A., Analyzing Protein Aggregation in Biopharmaceuticals. *BioPharm Int.* **2015,** *28* (1), 40-43.

139. Manning, M. C.; Manning, R. R.; Holcomb, R. E.; Henry, C. S.; Wilson, G. A., Review of Orthogonal Methods to SEC for Quantitation and Characterization of Protein Aggregates. *BioPharm Int.* **2014,** *27* (12), 32-39.

140. Staskus, P. W.; Johnson, W. C., Jr., Conformational transition of hyaluronic acid in aqueous-organic solvent monitored by vacuum ultraviolet circular dichroism. *Biochemistry* **1988,** *27* (5), 1522-7.

141. Cheng, R.; Liu, J.; Xie, P.; Wu, Y.; Deng, J., Chiral, pH-sensitive polyacrylamide hydrogels: Preparation and enantio-differentiating release ability. *Polymer* **2015,** *68*, 246-252.

142. Li, S.; Peng, Z.; Leblanc, R. M., Method To Determine Protein Concentration in the Protein-Nanoparticle Conjugates Aqueous Solution Using Circular Dichroism Spectroscopy. *Anal Chem* **2015,** *87* (13), 6455-9.

143. Ami, D.; Lavatelli, F.; Rognoni, P.; Palladini, G.; Raimondi, S.; Giorgetti, S.; Monti, L.; Doglia, S. M.; Natalello, A.; Merlini, G., In situ characterization of protein aggregates in human tissues affected by light chain amyloidosis: a FTIR microspectroscopy study. *Sci Rep* **2016,** *6*, 29096.

144. Derenne, A.; Goormaghtigh, E., FTIR Spectroscopy as a Multi-Parameter Analytical Tool. *BioPharm Int* **2017,** *30* (4), 35-40.

145. Zolls, S.; Tantipolphan, R.; Wiggenhorn, M.; Winter, G.; Jiskoot, W.; Friess, W.; Hawe, A., Particles in therapeutic protein formulations, Part 1: overview of analytical methods. *J Pharm Sci* **2012,** *101* (3), 914-35.

146. Ami, D.; Natalello, A.; Taylor, G.; Tonon, G.; Maria Doglia, S., Structural analysis of protein inclusion bodies by Fourier transform infrared microspectroscopy. *Biochim Biophys Acta* **2006,** *1764* (4), 793-9.

147. Mirabella, F. M. J., *Internal reflection spectroscopy: Theory and applications*. Marcel Dekker: New York, 1993; Vol. 15.

148. Foster, M. P.; McElroy, C. A.; Amero, C. D., Solution NMR of large molecules and assemblies. *Biochemistry* **2007,** *46* (2), 331-40.

149. Harke, B.; Chacko, J. V.; Haschke, H.; Canale, C.; Diaspro, A., A novel nanoscopic tool by combining AFM with STED microscopy. *Opt Nanoscopy* **2012,** *1* (1).

150. Graham, H. K.; Hodson, N. W.; Hoyland, J. A.; Millward-Sadler, S. J.; Garrod, D.; Scothern, A.; Griffiths, C. E.; Watson, R. E.; Cox, T. R.; Erler, J. T.; Trafford, A. W.; Sherratt, M. J., Tissue section AFM: In situ ultrastructural imaging of native biomolecules. *Matrix Biol* **2010,** *29* (4), 254-60.

151. Micheva, K. D.; O'Rourke, N.; Busse, B.; Smith, S. J., Array tomography: high-resolution three-dimensional immunofluorescence. *Cold Spring Harb Protoc* **2010,** *2010* (11), pdb top89.

152. Suri, S.; Schmidt, C. E., Cell-laden hydrogel constructs of hyaluronic acid, collagen, and laminin for neural tissue engineering. *Tissue Eng Part A* **2010,** *16* (5), 1703-16.

153. Waters, J., The concentration of soluble extracellular amyloid-beta protein in acute brain slices from CRND8 mice. *PLoS One* **2010,** *5* (12), e15709.

154. Talmon, Y.; Adrian, M.; Dubochet, J., Electron beam radiation damage to organic inclusions in vitreous cubic and hexagonal ice. *J. Microsc* **1986,** *141* (3), 375-384.

155. Glaeser, R., Radiation damage relative to transmission electron microscopy of biological specimens at low temperature. *J. Microsc* **1978,** *112* (1), 127-38.

156. Lucic, V.; Rigort, A.; Baumeister, W., Cryo-electron tomography: the challenge of doing structural biology in situ. *J Cell Biol* **2013,** *202* (3), 407-19.

157. Milligan, R. A.; Whittaker, M.; Safer, D., Molecular structure of F-actin and location of surface binding sites. *Nature* **1990,** *348* (6298), 217-21.

158. Jungbauer, L. M.; Yu, C.; Laxton, K. J.; LaDu, M. J., Preparation of fluorescently-labeled amyloid-beta peptide assemblies: the effect of fluorophore conjugation on structure and function. *J Mol Recognit* **2009,** *22* (5), 403-13.

159. Amaro, M.; Wellbrock, T.; Birch, D. J. S.; Rolinski, O. J., Inhibition of beta-amyloid aggregation by fluorescent dye labels. *Applied Physics Letters* **2014,** *104* (6), 063704.

160. Lilyestrom, W. G.; Shire, S. J.; Scherer, T. M., Influence of the cosolute environment on IgG solution structure analyzed by small-angle X-ray scattering. *J Phys Chem B* **2012,** *116* (32), 9611-8.

161. Loh, X. J.; Scherman, O. A.; Shibayama, M., *Polymeric and Self Assembled Hydrogels: From Fundamental Understanding to Applications*. Royal Society of Chemistry: 2012.

162. Stradner, A.; Cardinaux, F.; Schurtenberger, P., A small-angle scattering study on equilibrium clusters in lysozyme solutions. *J Phys Chem B* **2006,** *110* (42), 21222-31.

163. Rochas, C.; Geissler, E., Measurement of Dynamic Light Scattering Intensity in Gels. *Macromolecules* **2014,** *47* (22), 8012-8017.

164. Kloster, C.; Bica, C.; Lartigue, C.; Rochas, C.; Samios, D.; Geissler, E., Dynamics of a Polymer Solution in a Rigid Matrix. *Macromolecules* **1998,** *31* (22), 7712-7716.

165. Kloster, C.; Bica, C.; Rochas, C.; Samios, D.; Geissler, E., Dynamics of a Polymer Solution in a Rigid Matrix. 2. *Macromolecules* **2000,** *33* (17), 6372-6377.

166. Yagi, H.; Ban, T.; Morigaki, K.; Naiki, H.; Goto, Y., Visualization and classification of amyloid beta supramolecular assemblies. *Biochemistry* **2007,** *46* (51), 15009-17.

167. Ban, T.; Hoshino, M.; Takahashi, S.; Hamada, D.; Hasegawa, K.; Naiki, H.; Goto, Y., Direct observation of Abeta amyloid fibril growth and inhibition. *J Mol Biol* **2004,** *344* (3), 757-67.

168. Morell, M.; Bravo, R.; Espargaro, A.; Sisquella, X.; Aviles, F. X.; Fernandez-Busquets, X.; Ventura, S., Inclusion bodies: specificity in their aggregation process and amyloid-like structure. *Biochim Biophys Acta* **2008,** *1783* (10), 1815-25.

169. Roberti, M. J.; Jovin, T. M.; Jares-Erijman, E., Confocal fluorescence anisotropy and FRAP imaging of alpha-synuclein amyloid aggregates in living cells. *PLoS One* **2011,** *6* (8), e23338.

170. Amaro, M.; Kubiak-Ossowska, K.; Birch, D. J. S.; Rolinski, O. J., Initial stages of beta-amyloid Abeta1-40 and Abeta1-42 oligomerization observed using fluorescence decay and molecular dynamics analyses of tyrosine. *Methods Appl Fluoresc* **2013,** *1* (1), 015006.

171. Amaro, M.; Birch, D. J.; Rolinski, O. J., Beta-amyloid oligomerisation monitored by intrinsic tyrosine fluorescence. *Phys Chem Chem Phys* **2011,** *13* (14), 6434-41.

172. Rolinski, O. J.; Wellbrock, T.; Birch, D. J.; Vyshemirsky, V., Tyrosine Photophysics During the Early Stages of beta-Amyloid Aggregation Leading to Alzheimer's. *J Phys Chem Lett* **2015,** *6* (15), 3116-20.

173. Zustiak, S. P.; Boukari, H.; Leach, J. B., Solute diffusion and interactions in cross-linked poly(ethylene glycol) hydrogels studied by Fluorescence Correlation Spectroscopy. *Soft Matter* **2010,** *6* (15).

174. Vagias, A.; Sergelen, K.; Koynov, K.; Košovan, P.; Dostalek, J.; Jonas, U.; Knoll, W.; Fytas, G., Diffusion and Permeation of Labeled IgG in Grafted Hydrogels. *Macromolecules* **2017,** *50* (12), 4770-4779.

175. Michelman-Ribeiro, A.; Horkay, F.; Nossal, R.; Boukari, H., Probe diffusion in aqueous poly(vinyl alcohol) solutions studied by fluorescence correlation spectroscopy. *Biomacromolecules* **2007,** *8* (5), 1595-600.

176. Sengupta, P.; Garai, K.; Balaji, J.; Periasamy, N.; Maiti, S., Measuring Size Distribution in Highly Heterogeneous Systems with Fluorescence Correlation Spectroscopy. *Biophysical Journal* **2003,** *84* (3), 1977-1984.

177. Shah, M.; Rattray, Z.; Day, K.; Uddin, S.; Curtis, R.; van der Walle, C. F.; Pluen, A., Evaluation of aggregate and silicone-oil counts in pre-filled siliconized syringes: An orthogonal study characterising the entire subvisible size range. *Int J Pharm* **2017,** *519* (1-2), 58-66.

178. Dong, J.; Revilla-Sanchez, R.; Moss, S.; Haydon, P. G., Multiphoton in vivo imaging of amyloid in animal models of Alzheimer's disease. *Neuropharmacology* **2010,** *59* (4-5), 268-75.

179. Schultz, T.; Martinez, L.; de Marco, A., The evaluation of the factors that cause aggregation during recombinant expression in E. coli is simplified by the employment of an aggregation-sensitive reporter. *Microb Cell Fact* **2006,** *5*, 28.

180. Rodina, N. P.; Sulatsky, M. I.; Sulatskaya, A. I.; Kuznetsova, I. M.; Uversky, V. N.; Turoverov, K. K., Photophysical Properties of Fluorescent Probe Thioflavin T in Crowded Milieu. *J Spectrosc* **2017,** *2017*, 1-10.

181. Groenning, M., Binding mode of Thioflavin T and other molecular probes in the context of amyloid fibrils-current status. *J Chem Biol* **2010,** *3* (1), 1-18.

182. Li, D.; Shao, L.; Chen, B. C.; Zhang, X.; Zhang, M.; Moses, B.; Milkie, D. E.; Beach, J. R.; Hammer, J. A., 3rd; Pasham, M.; Kirchhausen, T.; Baird, M. A.; Davidson, M. W.; Xu, P.; Betzig, E., ADVANCED IMAGING. Extended-resolution structured illumination imaging of endocytic and cytoskeletal dynamics. *Science* **2015,** *349* (6251), aab3500.

183. Hauser, M.; Wojcik, M.; Kim, D.; Mahmoudi, M.; Li, W.; Xu, K., Correlative Super-Resolution Microscopy: New Dimensions and New Opportunities. *Chem Rev* **2017,** *117* (11), 7428-7456.

184. Leake, M. C., Transcription factors in eukaryotic cells can functionally regulate gene expression by acting in oligomeric assemblies formed from an intrinsically disordered protein phase transition enabled by molecular crowding. *Transcription* **2018,** *9* (5), 298-306.

185. Chong, S.; Dugast-Darzacq, C.; Liu, Z.; Dong, P.; Dailey, G. M.; Cattoglio, C.; Heckert, A.; Banala, S.; Lavis, L.; Darzacq, X.; Tjian, R., Imaging dynamic and selective low-complexity domain interactions that control gene transcription. *Science* **2018,** *361* (6400).

186. Dersch, S.; Graumann, P. L., The ultimate picture-the combination of live cell superresolution microscopy and single molecule tracking yields highest spatio-temporal resolution. *Curr Opin Microbiol* **2018,** *43*, 55-61.

187. Balzarotti, F.; Eilers, Y.; Gwosch, K. C.; Gynna, A. H.; Westphal, V.; Stefani, F. D.; Elf, J.; Hell, S. W., Nanometer resolution imaging and tracking of fluorescent molecules with minimal photon fluxes. *Science* **2017,** *355* (6325), 606-612.

188. Walsh, D. M.; Selkoe, D. J., A beta oligomers - a decade of discovery. *J Neurochem* **2007,** *101* (5), 1172-84.

189. Tanzi, R. E.; Bertram, L., Twenty years of the Alzheimer's disease amyloid hypothesis: a genetic perspective. *Cell* **2005,** *120* (4), 545-55.

190. Schneider, L. S.; Mangialasche, F.; Andreasen, N.; Feldman, H.; Giacobini, E.; Jones, R.; Mantua, V.; Mecocci, P.; Pani, L.; Winblad, B.; Kivipelto, M., Clinical trials and late-stage drug development for Alzheimer's disease: an appraisal from 1984 to 2014. *J Intern Med* **2014,** *275* (3), 251-83.

191. Banik, A.; Brown, R. E.; Bamburg, J.; Lahiri, D. K.; Khurana, D.; Friedland, R. P.; Chen, W.; Ding, Y.; Mudher, A.; Padjen, A. L.; Mukaetova-Ladinska, E.; Ihara, M.; Srivastava, S.; Padma Srivastava, M. V.; Masters, C. L.; Kalaria, R. N.; Anand, A., Translation of Pre-Clinical Studies into Successful Clinical Trials for Alzheimer's Disease: What are the Roadblocks and How Can They Be Overcome? *J Alzheimers Dis* **2015,** *47* (4), 815-43.

192. Sabo, S.; Lambert, M. P.; Kessey, K.; Wade, W.; Krafft, G.; Klein, W. L., Interaction of beta-amyloid peptides with integrins in a human nerve cell line. *Neurosci. Lett.* **1995,** *184* (1), 25-28.

193. Li, Y.-P.; Bushnell, A. F.; Lee, C.-M.; Perlmutter, L. S.; Wong, S. K. F., β-Amyloid induces apoptosis in human-derived neurotypic SH-SY5Y cells. *Brain Research* **1996,** *738* (2), 196-204.

194. Mattson, M. P.; Cheng, B.; Davis, D.; Bryant, K.; Lieberburg, I.; Rydel, R. E., beta-Amyloid peptides destabilize calcium homeostasis and render human cortical neurons vulnerable to excitotoxicity. *J Neurosci* **1992,** *12* (2), 376-389.

195. Kondo, T.; Imamura, K.; Funayama, M.; Tsukita, K.; Miyake, M.; Ohta, A.; Woltjen, K.; Nakagawa, M.; Asada, T.; Arai, T.; Kawakatsu, S.; Izumi, Y.; Kaji, R.; Iwata, N.; Inoue, H., iPSC-Based Compound Screening and In Vitro Trials

Identify a Synergistic Anti-amyloid beta Combination for Alzheimer's Disease. *Cell Rep* **2017,** *21* (8), 2304-2312.

196. Hilt, S.; Altman, R.; Kalai, T.; Maezawa, I.; Gong, Q.; Wachsmann-Hogiu, S.; Jin, L. W.; Voss, J. C., A Bifunctional Anti-Amyloid Blocks Oxidative Stress and the Accumulation of Intraneuronal Amyloid-Beta. *Molecules* **2018,** *23* (8).
197. Mahairaki, V.; Ryu, J.; Peters, A.; Chang, Q.; Li, T.; Park, T. S.; Burridge, P. W.; Talbot, C. C., Jr.; Asnaghi, L.; Martin, L. J.; Zambidis, E. T.; Koliatsos, V. E., Induced pluripotent stem cells from familial Alzheimer's disease patients differentiate into mature neurons with amyloidogenic properties. *Stem Cells Dev* **2014,** *23* (24), 2996-3010.
198. Hogrebe, N. J.; Gooch, K. J., Direct influence of culture dimensionality on human mesenchymal stem cell differentiation at various matrix stiffnesses using a fibrous self-assembling peptide hydrogel. *J Biomed Mater Res A* **2016,** *104* (9), 2356-68.
199. Hopkins, A. M.; DeSimone, E.; Chwalek, K.; Kaplan, D. L., 3D in vitro modeling of the central nervous system. *Prog Neurobiol* **2015,** *125*, 1-25.
200. Baker, B. M.; Chen, C. S., Deconstructing the third dimension: how 3D culture microenvironments alter cellular cues. *J Cell Sci* **2012,** *125* (Pt 13), 3015-24.
201. Ghourichaee, S. S.; Powell, E. M.; Leach, J. B., Enhancement of human neural stem cell self-renewal in 3D hypoxic culture. *Biotechnol Bioeng* **2017,** *114* (5), 1096-1106.

202. Ghourichaee, S. S.; Leach, J. B., The effect of hypoxia and laminin-rich substrates on the proliferative behavior of human neural stem cells. *J Mater Chem B* **2016,** *4* (20), 3509-3514.

203. Ribeiro, A.; Balasubramanian, S.; Hughes, D.; Vargo, S.; Powell, E. M.; Leach, J. B., beta1-Integrin cytoskeletal signaling regulates sensory neuron response to matrix dimensionality. *Neuroscience* **2013,** *248*, 67-78.

204. Ordikhani, F.; Sheth, S.; Zustiak, S. P., Polymeric particle-mediated molecular therapies to treat spinal cord injury. *Int J Pharm* **2017,** *516* (1-2), 71-81.

205. Ordikhani, F.; Zustiak, S. P.; Simchi, A., Surface Modifications of Titanium Implants by Multilayer Bioactive Coatings with Drug Delivery Potential: Antimicrobial, Biological, and Drug Release Studies. *Jom* **2016,** *68* (4), 1100-1108.

206. Fang, Y.; Eglen, R. M., Three-Dimensional Cell Cultures in Drug Discovery and Development. *SLAS Discov* **2017,** *22* (5), 456-472.

207. Osaki, T.; Shin, Y.; Sivathanu, V.; Campisi, M.; Kamm, R. D., In Vitro Microfluidic Models for Neurodegenerative Disorders. *Adv Healthc Mater* **2018,** *7* (2).

208. Siney, E. J.; Kurbatskaya, K.; Chatterjee, S.; Prasannan, P.; Mudher, A.; Willaime-Morawek, S., Modelling neurodegenerative diseases in vitro: Recent advances in 3D iPSC technologies. *AIMS Cell and Tissue Engineering* **2018,** *2* (1), 1-23.

209. Jorfi, M.; D'Avanzo, C.; Tanzi, R. E.; Kim, D. Y.; Irimia, D., Human Neurospheroid Arrays for In Vitro Studies of Alzheimer's Disease. *Sci Rep* **2018,** *8* (1), 2450.

210. Park, J.; Wetzel, I.; Marriott, I.; Dreau, D.; D'Avanzo, C.; Kim, D. Y.; Tanzi, R. E.; Cho, H., A 3D human triculture system modeling neurodegeneration and neuroinflammation in Alzheimer's disease. *Nat Neurosci* **2018,** *21* (7), 941-951.

211. Librizzi, F.; Fodera, V.; Vetri, V.; Lo Presti, C.; Leone, M., Effects of confinement on insulin amyloid fibrils formation. *Eur Biophys J* **2007,** *36* (7), 711-5.

212. Shirai, N. C.; Kikuchi, M., The interplay of intrinsic disorder and macromolecular crowding on alpha-synuclein fibril formation. *J Chem Phys* **2016,** *144* (5), 055101.

213. Musiani, F.; Giorgetti, A., Protein Aggregation and Molecular Crowding: Perspectives From Multiscale Simulations. *Int Rev Cell Mol Biol* **2017,** *329*, 49-77.

214. Gao, M.; Winter, R., The Effects of Lipid Membranes, Crowding and Osmolytes on the Aggregation, and Fibrillation Propensity of Human IAPP. *J Diabetes Res* **2015,** *2015*, 849017.

215. Crespo, R.; Villar-Alvarez, E.; Taboada, P.; Rocha, F. A.; Damas, A. M.; Martins, P. M., Insoluble Off-Pathway Aggregates as Crowding Agents during Amyloid Fibril Formation. *J Phys Chem B* **2017,** *121* (10), 2288-2298.

216. Liu, J.; Dehle, F. C.; Liu, Y.; Bahraminejad, E.; Ecroyd, H.; Thorn, D. C.; Carver, J. A., The Effect of Milk Constituents and Crowding Agents on

Amyloid Fibril Formation by kappa-Casein. *J Agric Food Chem* **2016,** *64* (6), 1335-43.

217. Berwick, R.; Vaux, D. J.; Jean, L., Multiphasic effect of vinyl pyrrolidone polymers on amyloidogenesis, from macromolecular crowding to inhibition. *Biochem J* **2018,** *475* (21), 3417-3436.
218. Glabe, C. G., Structural classification of toxic amyloid oligomers. *J Biol Chem* **2008,** *283* (44), 29639-43.
219. Dubnovitsky, A.; Sandberg, A.; Rahman, M. M.; Benilova, I.; Lendel, C.; Hard, T., Amyloid-beta protofibrils: size, morphology and synaptotoxicity of an engineered mimic. *PLoS One* **2013,** *8* (7), e66101.
220. Cizas, P.; Budvytyte, R.; Morkuniene, R.; Moldovan, R.; Broccio, M.; Losche, M.; Niaura, G.; Valincius, G.; Borutaite, V., Size-dependent neurotoxicity of beta-amyloid oligomers. *Arch Biochem Biophys* **2010,** *496* (2), 84-92.
221. Verma, M.; Vats, A.; Taneja, V., Toxic species in amyloid disorders: Oligomers or mature fibrils. *Ann Indian Acad Neurol* **2015,** *18* (2), 138-45.
222. Lorenzo, A.; Yankner, B. A., Amyloid Fibril Toxicity in Alzheimer's Disease and Diabetesa. *Ann. N. Y. Acad. Sci.* **1996,** *777* (1), 89-95.
223. Wu, C.; Lei, H.; Wang, Z.; Zhang, W.; Duan, Y., Phenol red interacts with the protofibril-like oligomers of an amyloidogenic hexapeptide NFGAIL through both hydrophobic and aromatic contacts. *Biophys J* **2006,** *91* (10), 3664-72.
224. Reyes Barcelo, A. A.; Gonzalez-Velasquez, F. J.; Moss, M. A., Soluble aggregates of the amyloid-beta peptide are trapped by serum albumin to enhance amyloid-beta activation of endothelial cells. *J Biol Eng* **2009,** *3*, 5.

225. Weber, P. A.; Chang, H. C.; Spaeth, K. E.; Nitsche, J. M.; Nicholson, B. J., The permeability of gap junction channels to probes of different size is dependent on connexin composition and permeant-pore affinities. *Biophys J* **2004,** *87* (2), 958-73.

226. Zustiak, S. P.; Pubill, S.; Ribeiro, A.; Leach, J. B., Hydrolytically degradable poly(ethylene glycol) hydrogel scaffolds as a cell delivery vehicle: characterization of PC12 cell response. *Biotechnol Prog* **2013,** *29* (5), 1255-64.

227. Novo, M.; Freire, S.; Al-Soufi, W., Critical aggregation concentration for the formation of early Amyloid-beta (1-42) oligomers. *Sci Rep* **2018,** *8* (1), 1783.

228. Sengupta, P.; Garai, K.; Balaji, J.; Periasamy, N.; Maiti, S., Measuring Size Distribution in Highly Heterogeneous Systems with Fluorescence Correlation Spectroscopy. *Biophys J* **2003,** *84* (3), 1977-1984.

229. Karran, E.; Mercken, M.; De Strooper, B., The amyloid cascade hypothesis for Alzheimer's disease: an appraisal for the development of therapeutics. *Nat Rev Drug Discov* **2011,** *10* (9), 698-712.

230. Cummings, J.; Lee, G.; Mortsdorf, T.; Ritter, A.; Zhong, K., Alzheimer's disease drug development pipeline: 2017. *Alzheimers Dement (N Y)* **2017,** *3* (3), 367-384.

231. Cummings, J.; Morstorf, T.; Lee, G., Alzheimer's drug-development pipeline: 2016. *Alzheimers Dement (N Y)* **2016,** *2* (4), 222-232.

232. Gilman, S.; Koller, M.; Black, R. S.; Jenkins, L.; Griffith, S. G.; Fox, N. C.; Eisner, L.; Kirby, L.; Rovira, M. B.; Forette, F.; Orgogozo, J. M.; Team, A. N.

S., Clinical effects of Abeta immunization (AN1792) in patients with AD in an interrupted trial. *Neurology* **2005,** *64* (9), 1553-62.

233. Holmes, C.; Boche, D.; Wilkinson, D.; Yadegarfar, G.; Hopkins, V.; Bayer, A.; Jones, R. W.; Bullock, R.; Love, S.; Neal, J. W.; Zotova, E.; Nicoll, J. A. R., Long-term effects of Aβ42 immunisation in Alzheimer's disease: follow-up of a randomised, placebo-controlled phase I trial. *The Lancet* **2008,** *372* (9634), 216-223.
234. Tabira, T., Immunization Therapy for Alzheimer Disease: A Comprehensive Review of Active Immunization Strategies. *Tohoku J Exp Med* **2010,** *220* (2), 95-106.
235. Drachman, D. A., The amyloid hypothesis, time to move on: Amyloid is the downstream result, not cause, of Alzheimer's disease. *Alzheimers Dement* **2014,** *10* (3), 372-80.
236. Engler, A. J.; Sen, S.; Sweeney, H. L.; Discher, D. E., Matrix elasticity directs stem cell lineage specification. *Cell* **2006,** *126* (4), 677-89.
237. Postovit, L. M.; Seftor, E. A.; Seftor, R. E.; Hendrix, M. J., A three-dimensional model to study the epigenetic effects induced by the microenvironment of human embryonic stem cells. *Stem Cells* **2006,** *24* (3), 501-5.
238. Cavo, M.; Caria, M.; Pulsoni, I.; Beltrame, F.; Fato, M.; Scaglione, S., A new cell-laden 3D Alginate-Matrigel hydrogel resembles human breast cancer cell malignant morphology, spread and invasion capability observed "in vivo". *Sci Rep* **2018,** *8* (1), 5333.

239. Sadri, S.; Khazaei, M.; Ghanbari, A.; Khazaei, M. R.; Shah, P., Neuronal differentiation of PC12 and embryonic stem cells in two- and three-dimensional in vitro culture. *Indian J Exp Biol* **2014,** *52* (4), 305-11.

240. Matsumura, S.; Shinoda, K.; Yamada, M.; Yokojima, S.; Inoue, M.; Ohnishi, T.; Shimada, T.; Kikuchi, K.; Masui, D.; Hashimoto, S.; Sato, M.; Ito, A.; Akioka, M.; Takagi, S.; Nakamura, Y.; Nemoto, K.; Hasegawa, Y.; Takamoto, H.; Inoue, H.; Nakamura, S.; Nabeshima, Y.; Teplow, D. B.; Kinjo, M.; Hoshi, M., Two distinct amyloid beta-protein (Abeta) assembly pathways leading to oligomers and fibrils identified by combined fluorescence correlation spectroscopy, morphology, and toxicity analyses. *J Biol Chem* **2011,** *286* (13), 11555-62.

241. Lu, J. X.; Qiang, W.; Yau, W. M.; Schwieters, C. D.; Meredith, S. C.; Tycko, R., Molecular structure of beta-amyloid fibrils in Alzheimer's disease brain tissue. *Cell* **2013,** *154* (6), 1257-68.

242. Ryan, T. M.; Caine, J.; Mertens, H. D.; Kirby, N.; Nigro, J.; Breheney, K.; Waddington, L. J.; Streltsov, V. A.; Curtain, C.; Masters, C. L.; Roberts, B. R., Ammonium hydroxide treatment of Abeta produces an aggregate free solution suitable for biophysical and cell culture characterization. *PeerJ* **2013,** *1*, e73.

243. Coalier, K. A.; Paranjape, G. S.; Karki, S.; Nichols, M. R., Stability of early-stage amyloid-beta(1-42) aggregation species. *Biochim Biophys Acta* **2013,** *1834* (1), 65-70.

244. Zhang, A.; Qi, W.; Good, T. A.; Fernandez, E. J., Structural differences between Abeta(1-40) intermediate oligomers and fibrils elucidated by proteolytic

fragmentation and hydrogen/deuterium exchange. *Biophys J* **2009,** *96* (3), 1091-104.

245. Zhang, Y.; Rempel, D. L.; Zhang, J.; Sharma, A. K.; Mirica, L. M.; Gross, M. L., Pulsed hydrogen-deuterium exchange mass spectrometry probes conformational changes in amyloid beta (Abeta) peptide aggregation. *Proc Natl Acad Sci U.S.A.* **2013,** *110* (36), 14604-9.
246. Broersen, K.; Rousseau, F.; Schymkowitz, J., The culprit behind amyloid beta peptide related neurotoxicity in Alzheimer's disease: oligomer size or conformation? *Alzheimers Res Ther* **2010,** *2* (4), 12.
247. Wang, S. S.; Becerra-Arteaga, A.; Good, T. A., Development of a novel diffusion-based method to estimate the size of the aggregated Abeta species responsible for neurotoxicity. *Biotechnol Bioeng* **2002,** *80* (1), 50-9.
248. Zhou, H. X.; Rivas, G.; Minton, A. P., Macromolecular crowding and confinement: biochemical, biophysical, and potential physiological consequences. *Annu Rev Biophys* **2008,** *37*, 375-97.
249. Yang, Y. L.; Leone, L. M.; Kaufman, L. J., Elastic moduli of collagen gels can be predicted from two-dimensional confocal microscopy. *Biophys J* **2009,** *97* (7), 2051-60.
250. Banerjee, P.; Lenz, D.; Robinson, J. P.; Rickus, J. L.; Bhunia, A. K., A novel and simple cell-based detection system with a collagen-encapsulated B-lymphocyte cell line as a biosensor for rapid detection of pathogens and toxins. *Lab Invest* **2008,** *88* (2), 196-206.

251. Alzheimer's Disease Education and Referral Center. https://www.nia.nih.gov/alzheimers (accessed January 2).

252. Servick, K., Another major drug candidate targeting the brain plaques of Alzheimer's disease has failed. What's left? *Science* **2019,** *363* (6433).

253. Simpson, L. W.; Hacene, B.; Good, T. A.; Leach, J. B., Collagen hydrogel confinement of Amyloid-β (Aβ) accelerates aggregation and reduces cytotoxic effects. *Submitted to Journal on Date* **2019**.

254. Yagi, T.; Ito, D.; Okada, Y.; Akamatsu, W.; Nihei, Y.; Yoshizaki, T.; Yamanaka, S.; Okano, H.; Suzuki, N., Modeling familial Alzheimer's disease with induced pluripotent stem cells. *Hum Mol Genet* **2011,** *20* (23), 4530-9.

255. Luo, Y.; Lou, C.; Zhang, S.; Zhu, Z.; Xing, Q.; Wang, P.; Liu, T.; Liu, H.; Li, C.; Shi, W.; Du, Z.; Gao, Y., Three-dimensional hydrogel culture conditions promote the differentiation of human induced pluripotent stem cells into hepatocytes. *Cytotherapy* **2018,** *20* (1), 95-107.

256. Wang, B.; Jakus, A. E.; Baptista, P. M.; Soker, S.; Soto-Gutierrez, A.; Abecassis, M. M.; Shah, R. N.; Wertheim, J. A., Functional Maturation of Induced Pluripotent Stem Cell Hepatocytes in Extracellular Matrix-A Comparative Analysis of Bioartificial Liver Microenvironments. *Stem Cells Transl Med* **2016,** *5* (9), 1257-67.

257. Jarosz-Griffiths, H. H.; Noble, E.; Rushworth, J. V.; Hooper, N. M., Amyloid-beta Receptors: The Good, the Bad, and the Prion Protein. *J Biol Chem* **2016,** *291* (7), 3174-83.

258. Castillo, G. M.; Lukito, W.; Peskind, E.; Raskind, M.; Kirschner, D. A.; Yee, A. G.; Snow, A. D., Laminin inhibition of β-amyloid protein (Aβ) fibrillogenesis and identification of an Aβ binding site localized to the globular domain repeats on the laminin a chain. *J. Neurosci. Res.* **2000,** *62* (3), 451-462.

259. Myllyharju, J.; Kivirikko, K. I., Collagens, modifying enzymes and their mutations in humans, flies and worms. *Trends Genet* **2004,** *20* (1), 33-43.

260. Shoulders, M. D.; Raines, R. T., Collagen structure and stability. *Annu Rev Biochem* **2009,** *78*, 929-58.

261. Boot-Handford, R. P.; Tuckwell, D. S., Fibrillar collagen: the key to vertebrate evolution? A tale of molecular incest. *Bioessays* **2003,** *25* (2), 142-51.

262. Parkhurst, M. R.; Saltzman, W. M., Quantification of human neutrophil motility in three-dimensional collagen gels. Effect of collagen concentration. *Biophys J* **1992,** *61* (2), 306-315.

263. Narayanan, J.; Xiong, J.-Y.; Liu, X.-Y., Determination of agarose gel pore size: Absorbance measurements vis a vis other techniques. *J Phys Conf Ser.* **2006,** *28*, 83-86.

264. Balgude, A. P.; Yu, X.; Szymanski, A.; Bellamkonda, R. V., Agarose gel stiffness determins rate of DRG neurite extension in 3D cultures. *Biomaterials* **2001,** *22* (10), 1077-84.

265. Laurent, T. C.; Fraser, J. R. E., Hyaluronan. *FASEB J* **1992,** *6*, 2397-2404.

266. Ruoslahti, E., Brain extracellular matrix. *Glycobiology* **1996,** *6* (5), 489-492.

267. Feng, Q.; Zhu, M.; Wei, K.; Bian, L., Cell-mediated degradation regulates human mesenchymal stem cell chondrogenesis and hypertrophy in MMP-sensitive hyaluronic acid hydrogels. *PLoS One* **2014,** *9* (6), e99587.

268. Khetan, S.; Guvendiren, M.; Legant, W. R.; Cohen, D. M.; Chen, C. S.; Burdick, J. A., Degradation-mediated cellular traction directs stem cell fate in covalently crosslinked three-dimensional hydrogels. *Nat Mater* **2013,** *12* (5), 458-65.

269. Fisher, S. A.; Anandakumaran, P. N.; Owen, S. C.; Shoichet, M. S., Tuning the Microenvironment: Click-Crosslinked Hyaluronic Acid-Based Hydrogels Provide a Platform for Studying Breast Cancer Cell Invasion. *Adv Funct Mater* **2015,** *25* (46), 7163-7172.

270. Cui, F. Z.; Tian, W. M.; Hou, S. P.; Xu, Q. Y.; Lee, I. S., Hyaluronic acid hydrogel immobilized with RGD peptides for brain tissue engineering. *J Mater Sci Mater Med* **2006,** *17* (12), 1393-401.

271. Marklein, R. A.; Burdick, J. A., Spatially controlled hydrogel mechanics to modulate stem cell interactions. *Soft Matter* **2010,** *6* (1), 136-143.

272. Khan, R.; Mahendhiran, B.; Aroulmoji, V., Chemistry of hyaluronic acid and its significance in drug delivery strategies: A review. *Int J Pharm Sci Res.* **2013,** *4* (9), 3699-3710.

273. Shu, X. Z.; Liu, Y.; Luo, Y.; Roberts, M. C.; Prestwich, G. D., Disulfide Cross-Linked Hyaluronan Hydrogels. *Biomacromolecules* **2002,** *3* (6), 1304-1311.

274. Nimmo, C. M.; Owen, S. C.; Shoichet, M. S., Diels-Alder Click cross-linked hyaluronic acid hydrogels for tissue engineering. *Biomacromolecules* **2011,** *12* (3), 824-30.

275. Cruise, G. M.; Scharp, D. S.; Hubbell, J. A., Characterization of permeability and network structure of interfacially photopolymerized poly(ethylene glycol) diacrylate hydrogels. *Biomaterials* **1998,** *19* (14), 1287-1294.

276. Zustiak, S. P.; Leach, J. B., Hydrolytically degradable poly(ethylene glycol) hydrogel scaffolds with tunable degradation and mechanical properties. *Biomacromolecules* **2010,** *11* (5), 1348-57.

277. Phelps, E. A.; Enemchukwu, N. O.; Fiore, V. F.; Sy, J. C.; Murthy, N.; Sulchek, T. A.; Barker, T. H.; Garcia, A. J., Maleimide cross-linked bioactive PEG hydrogel exhibits improved reaction kinetics and cross-linking for cell encapsulation and in situ delivery. *Adv Mater* **2012,** *24* (1), 64-70, 2.

278. Streets, A. M.; Sourigues, Y.; Kopito, R. R.; Melki, R.; Quake, S. R., Simultaneous measurement of amyloid fibril formation by dynamic light scattering and fluorescence reveals complex aggregation kinetics. *PLoS One* **2013,** *8* (1), e54541.

279. Velez, D. O.; Tsui, B.; Goshia, T.; Chute, C. L.; Han, A.; Carter, H.; Fraley, S. I., 3D collagen architecture induces a conserved migratory and transcriptional response linked to vasculogenic mimicry. *Nat Commun* **2017,** *8* (1), 1651.

280. Bahcecioglu, G.; Hasirci, N.; Bilgen, B.; Hasirci, V., A 3D printed PCL/hydrogel construct with zone-specific biochemical composition mimicking that of the meniscus. *Biofabrication* **2019,** *11* (2), 025002.

281. Manning, K. L.; Thomson, A. H.; Morgan, J. R., Funnel-Guided Positioning of Multicellular Microtissues to Build Macrotissues. *Tissue Eng Part C Methods* **2018,** *24* (10), 557-565.

282. Wu, S.; Xu, R.; Duan, B.; Jiang, P., Three-Dimensional Hyaluronic Acid Hydrogel-Based Models for In Vitro Human iPSC-Derived NPC Culture and Differentiation. *J Mater Chem B* **2017,** *5* (21), 3870-3878.

283. Xiao, W.; Ehsanipour, A.; Sohrabi, A.; Seidlits, S. K., Hyaluronic-Acid Based Hydrogels for 3-Dimensional Culture of Patient-Derived Glioblastoma Cells. *J Vis Exp* **2018,** (138).

284. Sharma, P. K.; Taneja, S.; Singh, Y., Hydrazone-Linkage-Based Self-Healing and Injectable Xanthan-Poly(ethylene glycol) Hydrogels for Controlled Drug Release and 3D Cell Culture. *ACS Appl Mater Interfaces* **2018,** *10* (37), 30936-30945.

285. Bicker, J.; Alves, G.; Fortuna, A.; Falcao, A., Blood-brain barrier models and their relevance for a successful development of CNS drug delivery systems: a review. *Eur J Pharm Biopharm* **2014,** *87* (3), 409-32.